

**USING DATA ANALYTICS AND LABORATORY EXPERIMENTS TO ADVANCE
THE UNDERSTANDING OF RESERVOIR ROCK PROPERTIES**

Zihao Li

Thesis submitted to the faculty of the Virginia Polytechnic Institute and State University in
partial fulfillment of the requirements for the degree of

Master of Science

In

Mining and Minerals Engineering

Cheng Chen, Chair

Nino Ripepi

Emily Sarver

December 5, 2018

Blacksburg, VA

Keywords: rock properties, in-lab experiment, Klinkenberg effect, multiple linear regression

Copyright 2018, Zihao Li

USING DATA ANALYTICS AND LABORATORY EXPERIMENTS TO ADVANCE THE UNDERSTANDING OF RESERVOIR ROCK PROPERTIES

Zihao Li

ACADEMIC ABSTRACT

Conventional and unconventional reservoirs are both critical in oilfield developments. After waterflooding treatments over decades, the petrophysical properties of a conventional reservoir may change in many aspects. It is crucial to identify the variations of these petrophysical properties after the long-term waterflooding treatments, both at the pore and core scales. For unconventional reservoirs, the productivity and performance of hydraulic fracturing in shales are challenging because of the complicated petrophysical properties. The confining pressure imposed on a shale formation has a tremendous impact on the permeability of the rock. The correlation between confining pressure and rock permeability is complicated and might be nonlinear. In this thesis, a series of laboratory tests was conducted on core samples extracted from four U.S. shale formations to measure their petrophysical properties. In addition, a special 2D microfluidic equipment that simulates the pore structure of a sandstone formation was developed to investigate the influence of injection flow rate on the development of high-permeability flow channels. Moreover, the multiple linear regression (MLR) model was applied with the predictors based on the development stages to quantify the variations of reservoir petrophysical properties. The MLR model outcome indicated that certain variables were effectively correlated to the permeability. The 2D microfluidic model demonstrated the development of viscous fingering when the injection water flow rate was higher than a certain level, which resulted in reduced overall sweep efficiency. These comprehensive laboratory experiments demonstrate the role of confining pressure, Klinkenberg effect, and bedding plane direction on the gas flow in the nanoscale pore space in shales.

USING DATA ANALYTICS AND LABORATORY EXPERIMENTS TO ADVANCE THE UNDERSTANDING OF RESERVOIR ROCK PROPERTIES

Zihao Li

PUBLIC ABSTRACT

Conventional and unconventional hydrocarbon reservoirs are both important in oil-gas development. The waterflooding treatment is the injection of water into a petroleum reservoir to increase reservoir pressure and to displace residual oil, which is a widely used enhanced oil recovery method. However, after waterflooding treatments for several decades, it may bring many changes in the properties of a conventional reservoir. To optimize subsequent oilfield development plans, it is our duty to identify the variations of these properties after the long-term waterflooding treatments, both at the pore and core scales. In unconventional reservoirs, hydraulic fracturing has been widely used to produce hydrocarbon resources from shale or other tight rocks at an economically viable production rate. The operation of hydraulic fracturing in shales is challenging because of the complicated reservoir pressure. The external pressure imposed on a shale formation has a tremendous impact on the permeability of the rock. The correlation between pressure and rock permeability is intricate. In this thesis, a series of laboratory tests was conducted on core samples to measure their properties and the pressure. Moreover, a statistical model was applied to quantify the variations of reservoir properties. The results indicated that certain reservoir properties were effectively correlated to the permeability. These comprehensive investigations demonstrate the role of pressure, special gas flow effect, and rock bedding direction on the gas flow in the extremely small pore in shales.

ACKNOWLEDGMENTS

I would first like to thank my advisor, Dr. Cheng Chen, for all the support and guidance that he gave me during the past one and half years. He steered me in the right research direction. I really appreciate his support and dedication in helping me during this study.

I would also like to thank my committee members, Dr. Ripepi and Dr. Sarver, for their helpful comments and suggestions.

I would like to acknowledge the help from Manuel Barros Daza, Kaiwu Huang, and Ming Fan for guiding me during the development of this thesis.

I am also thankful to the funding support of the Junior Faculty Award from Virginia Tech's Institute for Critical Technology and Applied Science, as well as the financial assistance provided by the U.S. Department of Energy through the National Energy Technology Laboratory's Program under Contract No. DE-FE0031576.

I would like to express my appreciation to my family and friends, including my wife, Ye Zang, my parents, and my friends Chenguang Du, Yuan Li, and Wenyu Gao, for their support during this study.

Table of Contents

Chapter 1. Introduction.....	1
1.1. Reservoir petrophysical properties and the MLR model	1
1.2. Pore-scale effects of long-term waterflooding	2
1.3. Role of effective stress, Klinkenberg effect, and bedding plane direction in unconventional reservoirs	5
Chapter 2. Using Data Mining to Quantify the Variations of Reservoir Petrophysical Properties Resulting from Long-term Waterflooding.....	9
2.1. Introduction	9
2.2. Overview of the Experimental and Data Mining Workflow	10
2.3. MLR Modeling.....	13
2.3.1. Assumption check before the analysis	13
2.3.2. Transformation of dependent variables	14
2.3.3. Processing of potential outliers.....	15
2.3.4. The Goodness-of-Fit for MLR model.....	15
2.3.5. Final mathematical expression of the MLR model.....	16
2.4. Results and Discussion.....	16
2.5. Conclusion.....	26
Chapter 3. Pore-scale Effects of Long-term Waterflooding Treatments on Reservoir Petrophysical Properties	27
3.1. Introduction	27
3.2. Methodology	27
3.2.1. Casting thin section imaging.....	27
3.2.2. Scanning electron microscopy	28

3.2.3.	Wettability and relative permeability curves	28
3.2.4.	2D microfluidic model	28
3.3.	Results and Discussion.....	30
3.4.	Conclusion.....	37
Chapter 4. Comprehensive laboratory investigation of Klinkenberg Effect and its role on apparent permeability in various U.S. shale formations.....		38
4.1.	Introduction	38
4.2.	Overview of the Experiment/Analysis Workflow.....	39
4.3.	Models and Experimental Equipment	40
4.3.1.	Simple effective stress law and Klinkenberg equation	40
4.3.2.	Effective stress coefficient law	41
4.3.3.	Pressure pulse decay experiment	43
4.4.	Results and Discussion.....	44
4.5.	Conclusions	63
Chapter 5. Conclusions and Recommendations.....		65
REFERENCE.....		68

List of Figures

Figure 2-1. An experiment/data-mining integrated workflow for the assessment of the variations of petrophysical properties of the core samples.	11
Figure 2-2. Porosity distribution in 1) Stage 1, 2) Stage 2, 3) Stage 3, and 4) Stage 4.	17
Figure 2-3. Permeability distribution in 1) Stage 1, 2) Stage 2, 3) Stage 3, and 4) Stage 4.	18
Figure 2-4. Porosity distribution in the four formations from Stage 1 through 4.	19
Figure 2-5. Permeability distribution in the four formations from Stage 1 through 4.	20
Figure 2-6. CT images of core-flooding experiments with different PVs. The top row of CT images demonstrates the displacement process for water injection, and the bottom row of CT images illustrates the displacement process for polymer injection. The purple color indicates high oil content whereas the red color indicates high injection fluid content. The other colors indicate mixtures of oil and the injection fluid.	21
Figure 2-7. Regression standardized predicted value versus regression standardized residual.	22
Figure 2-8. The frequency distributions of permeability a) before, and b) after the logarithmic transformation.	24
Figure 3-1. Two microfluidic flow models used in this study. Their pore geometries were both from the CTS images of the core samples extracted from Stage 4. The pixel dimensions of the images were 212×148 pixels in the x and y directions, respectively. The image resolution was 141 μm per pixel. The pore size in the models ranged from 200 μm to 400 μm. In the microfluidic models, the flow inlet was at the right side and the flow outlet was at the left side. The flow direction was thus horizontal and from the right to the left.	29
Figure 3-2. The thin section core samples selected from Stage 1 to Stage 4 in the waterflooding development history.	30

Figure 3-3. SEM images from Stage 1 through Stage 4. The four column (from left to right) account for various mineral components.	31
Figure 3-4. Relative permeability curves measured on core samples extracted from Stages 2, 3, and 4. Specifically, the red, yellow, and blue markers are for relative permeabilities of Stages 2, 3, and 4, respectively.....	32
Figure 3-5. Displacement process in Model A with a water injection flow rate of 5 ul/min. The pore geometry was from the CTS imaging results of Stage 4. Flow direction is from right to left. The blue fluid is water and the yellow fluid is oil, which initially occupies the pore space. The interval between snapshot pictures is 5 seconds.	33
Figure 3-6. Breakthrough moments in Model A with different injection flow rates	34
Figure 3-7. Breakthrough moments in Model B with different injection rates.....	34
Figure 3-8. Zone divisions in Model A and Model B. Zone 1 is at the center of the microfluidic model in the streamline direction and Zones 2, 3, 4, and 5 are sequentially located in the transverse direction.....	35
Figure 3-9. Weighted average of the sweep efficiency as a function of injection water flow rate.	35
Figure 3-10. Distribution of the sweep efficiency in each zone when the injected water reached breakthrough in Model A.	36
Figure 3-11. Distribution of the sweep efficiency in each zone when the injected water reached breakthrough in Model B.	36
Figure 4-1. An experiment/analysis workflow for the assessment of the correlation between apparent permeability, confining pressure, and effective stress.	40
Figure 4-2. Schematic PDP equipment setup, which consists of an upstream test gas reservoir having a volume of V_1 , a high-pressure core holder with the pore volume of V_p , a downstream gas reservoir having a volume of V_2 , a differential pressure transducer to continuously measure the pressure difference (ΔP) between the upstream and downstream reservoirs, and a second pressure transducer to measure the downstream reservoir pressure, P_2	43

Figure 4-3. Core samples used in the PDP tests. The core samples were extracted from four U.S. shale formations, including the Eagle Ford, Marcellus, Mancos, and Barnett formations. “PL” denotes that the core axis direction is parallel to the bedding plane direction, whereas “PD” indicates that the core axis direction is perpendicular to the bedding plane direction..... 44

Figure 4-4. Apparent permeability as a function of pore pressure under different effective stresses in the core of a) Mancos PL, b) Mancos PD, c) Barnett PL, d) Barnett PD, e) Eagle Ford PL, and f) Marcellus PL. 49

Figure 4-5. k_a/k as a function of $1/P_p$, as well as the linear equation fitting, in the core samples of a) Mancos PL, b) Mancos PD, c) Barnett PL, d) Barnett PD, e) Eagle Ford PL, and f) Marcellus PL. Based on Equation 4-1, the y-intercept of the linear equation is 1 and the slope is equal to the Klinkenberg coefficient, b..... 52

Figure 4-6. The value of $\log(k)$ as a function of the confining pressure, P_c , under varying pore pressures in the formations of a) Mancos PL, b) Mancos PD, c) Barnett PL, d) Barnett PD, e) Eagle Ford PL, and f) Marcellus PL. 53

Figure 4-7. The value of $\log(k)$ as a function of pore pressure in the formations of a) Mancos PL, b) Mancos PD, c) Barnett PL, d) Barnett PD, e) Eagle Ford PL, and f) Marcellus PL. 57

Figure 4-8. PDP-measured apparent permeability as a function of the effective stress calculated based on χ in a) Mancos PL, b) Mancos PD, c) Barnett PL, d) Barnett PD, e) Eagle Ford PL, and f) Marcellus PL. 63

List of Tables

Table 2-1. Correlation between predictors, which include porosity (Φ), sorting coefficient (S_p), mean radius (r), homogeneous coefficient (α), and displacement pressure (P_d)..	23
Table 2-2. Goodness-of-fit Information. Model 1 includes the predictor of porosity, Model 2 includes the predictors of porosity and mean radius, and Model 3 includes the predictors of porosity, mean radius, and sorting coefficient.....	24

Chapter 1. Introduction

1.1. Reservoir petrophysical properties and the MLR model

Consumption of hydrocarbon energy in the world has been steadily increasing during the past several decades. To meet the rising energy demand, some oilfields that have been developed for several decades will still play an important role because the remaining hydrocarbon resources in place are still promising. In order to adequately recover the hydrocarbon resources in these reservoirs, the reservoir petrophysical properties after several decades of development should be assessed and characterized accurately before tertiary recovery or another enhanced oil recovery (EOR) processes occur. In many conventional oilfields, waterflooding, which is considered as a secondary recovery process, is an important method to enhance oil recovery. After waterflooding treatments of several decades, the petrophysical properties of the reservoir can vary in many aspects. It is crucial to identify and evaluate the variations of the petrophysical properties in order to optimize follow-on production strategies.

Waterflooding is the use of water injection to increase the production from oil reservoirs. Water displaces oil from the pore space, and the efficacy of the displacement depends on many factors (Craig, 1971). This method is usually regarded as a secondary recovery approach. In many oilfields, waterflooding is the most commonly used secondary recovery method because water is affordable, readily available in large volumes, and effective in substantially increasing oil recovery (Willhite, 1986). Petrophysics is the study of the physical and chemical properties of a rock formation and their interactions with fluids (Tiab and Donaldson, 1999). The key petrophysical properties include porosity, permeability, water and oil saturations, and pore structure, etc. Decades of waterflooding treatments inevitably change the petrophysical properties of a reservoir. It is crucial to advance the understanding of the variations of the petrophysical properties resulting from the long-term waterflooding treatments in order to optimize subsequent production strategies and to maximize the hydrocarbon recovery factor.

As an important method of data mining and data analytics, linear regression is an approach to modeling the relationship between a dependent variable and one or more independent variables. The case of one independent variable is called simple linear regression. The process for more than

one independent variable is called multiple linear regression (MLR) (Seber and Lee, 2012). The assumptions for conducting the MLR modeling are as follows (Yamane, 1973): (1) the relationship between the dependent variable and independent variables (i.e., the predictors) is linear; (2) the error term is assumed to have a normal distribution with zero mean and constant variance; (3) homoscedasticity: the variance of the error term is constant regardless of the predictors; (4) non-multicollinearity: the regression model should not have two or more predictors moderately or highly correlated. Dahraj et al. (2014) developed the linear mathematical model using statistical methods to predict permeability from porosity. However, the single predictor has considerable limitations in terms of the prediction accuracy. The MLR model can avoid such limitations by using multiple predictors.

The studied reservoir in this thesis is located in Northeastern China. The reservoir depth was around 2200 m, the oil-bearing area was 0.89 km², and the oil reserves were estimated as 1.57×10⁷ barrels. The major reservoir lithology includes mudstone, silty mudstone, and siltstone. The average thicknesses of sandstone and oil layers were 57.1 m and 24.5 m, respectively. The reservoir can be divided into four mid-term sedimentary cycles. Based on the sedimentary cycles, the reservoirs can be categorized into four formation groups (Formations I, II, III, and IV). The flooding surface of Formation I constantly rose and formed the predominant development cycle of the top mudstone section.

Chapter 2 of this thesis presents a comprehensive study of the changes of petrophysical properties through four different development stages under long-term waterflooding treatments. The investigated petrophysical properties include porosity, permeability, velocity and salinity sensitivity, and water and oil saturation distributions. Moreover, this study quantified the variations of the petrophysical data by the combination of mercury intrusion data and the MLR model, which leads to a methodology of multi-measurement investigation for the petrophysical properties of conventional reservoir development. Reservoir simulations can also benefit from this study with greatly detailed and improved prediction of reservoir petrophysical properties.

1.2. Pore-scale effects of long-term waterflooding

Most oilfields located in Northeastern or Eastern China have experienced several decades of hydrocarbon production, and they are all facing the issues of high water cut in produced liquids

and low oil recovery factors. Nowadays, many conventional oilfields in China, such as Daqing Oilfield, Shengli Oilfield, and Jilin Oilfield, have a water cut level higher than 90%. The high water-cut issue is generally associated with the development of high-permeability flow channels in the reservoir rock, and high-permeability flow channels is one of the most common issues faced by the oilfields which are in the later development stage of waterflooding treatments (Zhou, 1998). In a reservoir rock, high-permeability flow channels cause preferential flow paths of the injected fluids (water or other displacing fluids), leading to a relatively low sweep efficiency. The facts described above demonstrate the challenges in the development of conventional oilfields. However, these conventional reservoirs still contribute roughly 70% of the total oil production in China each year and thus will continue to play a critical role in future energy production. Pore-level investigation of core samples before and after long-term waterflooding treatments is an effective approach to understand the role of long-term waterflooding on the changes of pore-scale petrophysical characteristics, which dictate larger-scale petrophysical properties of the reservoir rock. In this study, the target reservoir is located in an oilfield in Northeastern China. The oil-producing formation depth is around 2200 m. The oil-bearing formation area is 0.89 km². The average thickness of the sandstone is 57.1 m, and the oil-bearing layer thickness is about 24.5 m. According to the development time sequence, four development stages, from Stages 1 through 4, were categorized and core samples were extracted from each of them.

The variation of rock petrophysical properties during the process of reservoir development has been a problem of interest for many years. Lucia et al. (1983) built improved relationships between porosity, permeability, capillary properties, and m values in carbonate rocks. Chierici et al. (1967) investigated two hundred core samples to study the influence of the overburden pressure on porosity, horizontal and vertical permeability, the relative permeability of gas, formation resistivity factor, and the capillary pressure curve. Zhang, et al. (1997) used laboratory methods to study the difference in the petrophysical properties of two groups of sandstones extracted from the Daqing oilfield, with one group being subjected to waterflooding treatments and the other group without waterflooding treatments. They concluded that injecting a large amount of water for a long time was an effective approach to enhance oil recovery in the Daqing Sandstone. Dunn et al. (1999) suggested an approach to assess permeability based on porosity, electrical formation factor, and nuclear magnetic resonance relaxation time, by studying a man-made porous medium having a periodic structure of packed spheres. Pranter et al. (2006) developed a detailed, three-dimensional

(3D) petrophysical model for a dolomite rock and then used a two-dimensional (2D) multiphase waterflooding simulator to identify and understand the effect of formation heterogeneity on reservoir production performance. Gupta et al. (2011) demonstrated the potential of advanced ion management (AIM) to increase oil recovery compared to conventional waterflooding treatments. The AIM approach involves adding and/or removing ions from the injection water to improve waterflooding performance. Li et al. (2016) found that alkaline-surfactant-polymer flooding can greatly influence the petrophysical properties of a reservoir. Sometimes the drastic changes in the petrophysical properties can lead to formation damage.

The topic of high-permeability flow channels has attracted significant attention in the oil and gas industry. They high-permeability conduits can be generated by geological movements (Montgomery et al., 1997), conventional oilfield development processes (Jadhunandan et al., 1995), and hydraulic fracturing operations (Haimson, B. C, 1978). These high-permeability conduits can become the cause that leads to low sweep efficiency. Long-term waterflooding treatments in general can result in high-permeability flow channels (Denney, 2010). Howard et al. (1998) discussed laboratory experimental studies to identify and understand the nature of channel growth and stability in proppant packs with and without fibers. The high-permeability flow channel length increases in a stepwise manner with increasing flow rate. The channels are stable over time at a constant flow rate. Ameen et al. (2015) conducted laboratory experimental studies and the results confirmed the presence of a transition process from uniform Darcy flow to fingering-pattern flow. Gooma et al. (2017) described experimental results and numerical models in order to develop a new method to generate stable proppant pillars. The results showed that with the occurrence of viscous-fingering phenomena, a pillar-propped fracture having conductive and stable flow channels could be created. A lot of works have been done for high-permeability flow channels that cause negative effects on oil and gas production. For instance, Hess et al. (1971) summarized many chemical methods for formation plugging and then developed a new chemical method for permanent formation plugging. Mojarad et al. (2005) presented the formulation and numerical implementation of two coupled reservoir flow and damage models. They also presented and evaluated several methods of implementing the velocity-based model. Zhao et al. (2017) introduced a new type of plugging particles to tackle the high-permeability flow channels in a reservoir having high temperature and high salinity. The particles can plug the high-permeability

flow channels and consequently mitigate the preferential flow paths, which cause low sweep efficiency.

In Chapter 3 of this thesis, the methods of casting thin sections (CTS) imaging, scanning electron microscopy (SEM) imaging, wettability testing, and laboratory microfluidic experiments were used to investigate the petrophysical properties of the core samples at the pore scale. We then analyzed the images from CTS and SEM to identify and understand the petrophysical property variations before and after waterflooding treatments. Wettability testing using relative permeability curves was also conducted. In the end, microfluidic experiments were developed based on CTS imaging results in order to understand the relation between sweep efficiency and injection flow rate.

1.3. Role of effective stress, Klinkenberg effect, and bedding plane direction in unconventional reservoirs

The complicated petrophysical properties and extremely low permeability of shale formations lead to extraordinary challenges to the development of unconventional hydrocarbon resources from these formations, such as shale oil and gas formations. Horizontal drilling associated with multi-stage hydraulic fracturing has become an effective technique to produce hydrocarbon resources from shales at an economically viable rate (Economides and Nolte, 2000; Gu and Mohanty, 2014; Chen et al., 2015). Fracture creation and propagation is an essential step in the process of hydraulic fracturing. In order to achieve this goal, the injection pressure should be higher than the minimum horizontal principal stress in the formation (Ye and Ghassemi, 2016). During hydrocarbon recovery, the decreased pore pressure leads to increased effective stress and fracture closure (Fan et al., 2017b, 2018). The effective stress variation has a significant impact on the petrophysical properties in the shale formation, especially the formation permeability. It is thus crucial to investigate the relationship between formation permeability and effective stress variation.

The investigation of the correlation between effective stress and rock permeability began with tight sandstones in the laboratory. Warpinski and Teufel (1992) performed laboratory experiments to study the effective stress law in tight sandstone and chalk. They found that the effective stress coefficient (i.e., the Biot coefficient), α , in tight sandstone was close to unity for small stresses but

contained uncertainties for larger stresses. The value of α varied with both effective stress and pore pressure. Zhang et al. (2000) set up laboratory experiments to test the dependence of permeability on loading conditions. It was found that the trend and magnitudes of permeability variations were controlled by the initial size of the fracture aperture, external load configuration, and rock deformation. The permeability changes appeared to be unpredictable when the rock deformation was in the inelastic stage. Chenevert and Sharma (1993) used laboratory-measured permeability and pore pressure data to characterize swelling pressure and spalling types of wellbore instability. Worthington (2004) quantified the dependence of permeability on mechanical stress through third-order polynomial formulation. The research outcome emphasized the importance of detailed field studies. Ojala and Fjær (2007) tested Castlegate sandstone cores under cyclic pore and confining pressure variations. Their results demonstrated that the effective stress coefficient under acoustic and elastic testing in the sandstone can be considerably different from unity. They also illustrated the hysteresis in petrophysical properties due to microfracture or frictional effects.

The Klinkenberg effect was proposed by Klinkenberg (1941) to explain the abnormal phenomenon of apparent permeability enhancement for gas flow in porous media. It has a significant impact on gas flow, especially in low permeability porous media such as shale reservoirs and tight coalbeds (Wu et al., 1998). The Klinkenberg effect is related to the Knudsen (Kn) number, which is defined as $Kn = \lambda/d$, where λ is gas mean-free-path length (m) and d is pore diameter (m). When $Kn < 0.001$, gas flow is governed by the Navier-Stokes equation with a no-slip boundary condition on the pore walls. When $0.001 < Kn < 0.1$, gas flow is in the slip flow regime in which the non-continuum effect can be approximated by a velocity slip on the pore walls; the bulk gas flow can still be governed by the Navier-Stokes equation (Beskok and Karniadakis, 1999). The continuous increase in Kn leads to the transitional flow regime ($0.1 < Kn < 10$) and then the free molecular flow regime ($Kn > 10$), where the gas flow cannot be described by the Navier-Stokes equation any more (Dr. X. Yin, personal communication, 2018).

In a shale formation, when the nanopore diameter decreases or gas pressure decreases (lower gas pressure leads to a larger gas molecule mean-free-path length), the Kn number increases. In this scenario, the nanopore diameter can be comparable to or smaller than the mean-free-path length of gas molecules. As a consequence, gas molecules collide with the pore walls more frequently than with one another, leading to Knudsen diffusion that causes a slip-velocity boundary

condition in the macroscopic Navier-Stokes flow model (Javadpour, 2009). The existence of the slip velocity on flow boundaries enhances the overall mass flux through the nanotube, which results in increased apparent permeability of the shale (Chen, 2016).

A series of analytical solutions was developed to characterize gas flow in tight porous media subjected to the Klinkenberg effect (Wu et al., 1998; Innocentini and Pandolfelli., 2001; Zhu et al., 2007; Hu et al., 2009; Hayek, 2015). Based on previous works in the literature, Firouzi et al. (2013) developed a non-equilibrium molecular dynamics model and then conducted pressure pulse decay experiments to compare the model predictions with laboratory measurements. They found that the laboratory measurements were about two orders of magnitude larger than the model predictions. Li et al. (2016) derived an analytical formula for gas effective permeability subjected to the Klinkenberg effect based on the microscale flow model and fractal capillary model. Their results demonstrated the physical meaning of the model parameters. In a complicated environment, such as polymer-water-oil flow in porous media, the Klinkenberg effect was found to be mitigated with the presence of an adsorption polymer layer (Blanchard et al., 2007). Moreover, the Klinkenberg coefficient cannot be treated as a constant in coalbeds due to the high compressibility and matrix swelling of coal (Wang et al., 2014). All the studies reviewed above confirm that the Klinkenberg effect exists in a wide range of subsurface flow and transport processes associated with geoenery and geoenvironmental implications.

In Chapter 4 of this thesis, we collected core samples from four U.S. shale formations, including Mancos, Eagle Ford, Barnett, and Marcellus, to investigate the correlations between apparent permeability, k_a , confining pressure, P_c , and effective stresses, P_e . We also tested core samples extracted in various directions; specifically, the cores extracted along the bedding planes included “PL” in the sample names, which means “parallel”, whereas the cores extracted perpendicular to the bedding planes included “PD” in the sample names, which means “perpendicular”. By doing this, the role of bedding plane direction on core permeability was unraveled. In this study, a core sample was tested using a pressure pulse decay permeameter (PDP), subjected to comprehensive combinations of pore pressures, P_p , and confining pressures, P_c . The gas used in the PDP is pure nitrogen. Measured permeability and pressure data were fitted using the simple effective stress law and the effective stress coefficient law. We then obtained the Klinkenberg coefficient, b , and the effective mean pore radius, r , using the simple effective stress law. Using the effective stress coefficient law, we derived the effective stress coefficient, χ , and

then calculated P_e , which has a one-to-one correlation with measured permeability, k . The value of $\log(k)$ was plotted as a function of P_e to demonstrate the correlation between them. This comprehensive, laboratory experimental study advances the fundamental understanding of the role of confining pressure, pore pressure, Klinkenberg effect, and bedding plane direction on shale permeability. The research outcome has the potential to advance the scientific understanding of the relationship between geomechanical stress and flow and transport properties in a shale formation. Generated knowledge will be helpful in stress analysis and the optimization of hydraulic fracturing.

Chapter 2. Using Data Mining to Quantify the Variations of Reservoir Petrophysical Properties Resulting from Long-term Waterflooding

2.1. Introduction

After waterflooding treatments over several decades, the petrophysical properties of a hydrocarbon reservoir may change in many aspects. In order to continue producing economically, it is crucial to identify the variations of these petrophysical properties after the long-term waterflooding treatments. Therefore, several groups of core samples, which were extracted from an old oilfield in Northeastern China, were collected to investigate the variations in these petrophysical properties. These samples were extracted from four different inspection wells and thus can represent the four different stages of the reservoir during the development history. A series of laboratory tests, including mercury intrusion porosimetry, CT-flooding experiments, and sensitivity experiments, was conducted on the samples to measure the petrophysical properties such as porosity, permeability, pore structure, sensitivity, and water saturate variation. The experimental results demonstrated that both the mean values and standard deviations of the porosity and permeability increased after the long-term waterflooding treatment. The variations of sensitivity and pore structure presented significant directionality. Moreover, the CT-flooding experiments explicitly illustrated the development process of high-permeability channels. The mercury intrusion porosimetry results were then classified and analyzed using data mining methods. Specifically, the multiple linear regression (MLR) model was applied with the predictors based on the development stages to quantify the variations of reservoir petrophysical properties resulting from long-term waterflooding. The dependent variable was permeability and the predictors of the MLR model included porosity, sorting coefficient, and some other pore structure indexes. The model outcome indicated that certain variables were effectively correlated to the permeability. Based on the comparison between the four different development stages, it was noticed that some weight coefficients changed during the development process whereas the others stayed almost constant. The predictors having the highest weight coefficients were porosity, mean pore radius, and sorting coefficient. The improved understanding of the variations of reservoir petrophysical properties resulting from long-term waterflooding treatments will provide valuable insight and guidance for follow-on production designs.

Keywords: long-term waterflooding treatment, petrophysical properties, in-lab experiment, data mining, multiple linear regression model

2.2. *Overview of the Experimental and Data Mining Workflow*

This section aims to provide an overview of the experimental and data mining workflow. Details of the MLR model will be given in a later section. In this work, an experiment/data-mining integrated approach was developed to identify and quantify the variations of reservoir petrophysical properties of the core samples that were subjected to the long-term waterflooding treatment. First, a series of permeability and porosity measurements were conducted on the core samples extracted from four different development stages in the same oil reservoir. CT-flooding experiments with two injection fluids (formation water and polymer) were then carried out to illustrate water and oil saturation changes in the core sample. The comparison of these two injection fluids will contribute to the development strategies after long-term waterflooding. Second, the velocity and salinity sensitivity of core samples was tested to reveal the influence of waterflooding on the core samples. The details of pore structure will then be investigated by mercury intrusion porosimetry. Third, the MLR model was developed based the mercury intrusion data from the four development stages. The variations in the petrophysical properties can be quantified using the MLR model. **Figure 2-1** demonstrates a schematic workflow for the experimental and data mining workflow in this study

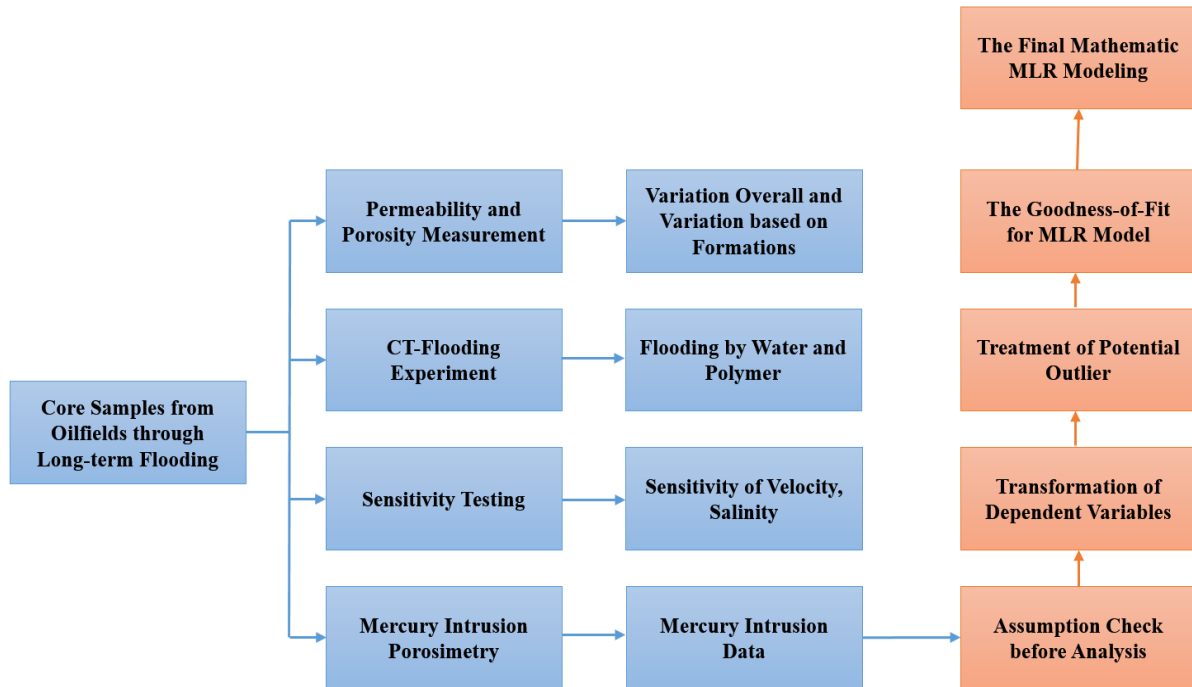


Figure 2-1. An experiment/data-mining integrated workflow for the assessment of the variations of petrophysical properties of the core samples.

More than three hundred core samples were collected from the oilfield and then classified by stages and formations. Specifically, the core samples were categorized into four stages, and Stages 1 through 4 followed the time sequence during the waterflooding development history. Therefore, Stage 1 samples experienced the shortest time of waterflooding treatment whereas Stage 4 samples experienced the longest time of waterflooding treatment. These core samples were collected from several inspection wells which were in close proximity, thus the extracted rock samples had similar initial petrophysical properties. Therefore, the changes in the petrophysical properties resulted primarily from the impact of waterflooding treatment. In addition, these inspection wells were located directly between the injection well and the production well, which suggests that the impact of the waterflooding treatment can be observed during the time scale of reservoir production. The injected water was surface water collected near the oilfield. In the laboratory, the porosity and permeability measurements were conducted by the helium porosity automatic analyzer and the core permeability analyzer. The testing temperatures were kept the same as the formation temperatures.

After the porosity and permeability measurements, core samples from Stage 4 were selected to carry out CT-flooding experiments, because Stage 4 is the last stage in the waterflooding development process, after which a new development strategy is needed. The traditional oil saturation measurement methods can only obtain the oil saturation of the entire core sample, and the distribution of oil saturation at the sub-core scale cannot be observed. X-ray computed tomography (CT) scanning is a non-invasive method that can observe oil saturation distribution at the sub-core scale. In the CT-flooding experiment, the scanning resolution was 2 mm/pixel in the longitudinal (z-) direction and 0.42 mm/pixel in the other two transverse (x- and y-) directions. and the fluid injection rate was 0.5 ml/min. The injection fluids used in this study were formation water and polymer. CT scanning was conducted during the process of water and polymer injections, leading to temporal snapshots of two-fluid distributions in the core sample.

Besides the CT-flooding experiments, we also conducted sensitivity experiments on the core samples. The sensitivity tests include the velocity sensitivity test and the salinity sensitivity test. The purpose of the sensitivity tests was to determine the triggering levels of flow velocity and salinity that cause abrupt changes in rock permeability. The velocity sensitivity is usually associated with grain migration, pore throat plugging, and permeability decrease. The salinity sensitivity refers to the permeability variation due to the change of water salinity. We conducted flooding experiment on samples extracted from the four different stages during the reservoir development history to measure the velocity and salinity sensitivity variations.

The result of mercury intrusion porosimetry experiments provides more details about the variation of the pore structure. Besides the porosity (ϕ) and permeability (k), the mercury intrusion data also include the sorting coefficient (S_p), relative sorting coefficient (D_r), mean radius (\bar{r}), structure coefficient (ϕ_p), feature structure index ($1/D_r\phi_p$), homogeneous coefficient (α), and displacement pressure (P_d), etc. The sorting coefficient (S_p) describes the distribution of grain size of sediments. The higher the sorting coefficient, the more uniform the grain size distribution is. The relative sorting coefficient (D_r) is the ratio of the sorting coefficient to the mean grain radius. The mean radius (\bar{r}) is the average of pore radius. The structure coefficient (ϕ_p) describes the curvature and connectivity of the pore channels. The feature structure index ($1/D_r\phi_p$) is the reciprocal of the product of the relative sorting coefficient and the structure coefficient. The homogeneous coefficient (α) accounts for the deviation between pore radius and the maximum

pore radius. A higher value of α implies a more uniform distribution of pore size. The displacement pressure (P_d) is the pressure at which the non-wettability fluid begins to enter into the maximum pore of the core sample. All the properties described above can describe the pore structure from different perspectives. However, some of them, such as feature structure index and relative coefficient, have functional relations with porosity and permeability. Therefore, we select five variables, which are independent on the permeability, as the predictors in the MLR model. The five predictors are porosity, sorting coefficient, mean pore radius, homogeneous coefficient, and displacement pressure. After the predictors were determined, the MLR model can be developed. In this study, the MLR model was built through the following procedures: first, the assumption check before the analyses; second, the transformation of dependent variables; third, processing of potential outliers; fourth, the goodness-of-fit test for the MLR model; and fifth, the final mathematical presentation of the MLR model. The details about the MLR modeling will be described in the following section.

2.3. MLR Modeling

The details of MLR model fitting of the mercury intrusion data are provided in this section.

2.3.1. Assumption check before the analysis

The hypothesized MLR model in this study can be written as:

$$Y = \beta_1 X_1 + \beta_2 X_2 + \beta_3 X_3 + \beta_4 X_4 + \beta_5 X_5 \quad (2-1)$$

where Y is permeability, X_1 is porosity, X_2 is sorting coefficient, X_3 is mean radius, X_4 is homogenous coefficient, X_5 is displacement pressure, and $\beta_{1\sim 5}$ are the standardized regression coefficients for the five predictors.

Three assumptions were made through the MLR modeling process, described as follows.

Step 1. The Gaussian distribution of the random error $\varepsilon \sim (0, \sigma^2)$

It is hypothesized that the error of the regression model is normally distributed. In order to check this assumption, the probability-probability (P-P) plot is produced, which compared the cumulative probability of the residual against the cumulative probability of the theoretical normal distribution

(Park, 2015). If the data of the residuals are normally distributed or approximated to a normal distribution, they should fall into the straight diagonal line (reference line). However, if most of the empirical data deviate from the reference line, it indicates that the assumption of normal distribution for the residual is not valid. In this case, the transformation of the dependent variable (i.e., Y, the permeability) is needed. Next, the Kolmogorov-Smirnov statistic test for normality will be conducted. If the test shows that the p-value is less than 0.05, it indicates that the null hypothesis of normal distribution should be rejected (Lopes, 2011).

Step 2. The homoscedasticity

The homoscedasticity assumption requires the equal variances of the dependent variable across a range of predictors. In order to check this assumption, a residual versus fitted value plot should be created. In this plot, the x-axis shows the fitted or predicted values and the y-axis is for the errors of prediction. Ideally, this assumption is valid when the scores are randomly scattered over a horizontal line across the zero (Garson, 2012).

Step 3. No perfect collinearity.

This assumption requires that all the predictors are not perfectly linearly related. In the exploration stage, the pairwise correlations between independent variables are calculated to avoid this issue (Bager, Ali, et al., 2017). The rule of thumb is that if the correlation coefficient is larger than 0.8, then severe multiple collinearities may be present. Another way to check this issue is to obtain the variance inflation factor (VIF). The VIF measures the extent to which multicollinearity has increased the variance of an estimated coefficient (Bager, Ali, et al, 2017). It looks at the extent to which an explanatory variable can be explained by all the other explanatory variables in the equation. The VIF is often calculated simultaneously with the estimation of the regression coefficient, and it will be checked when the final regression model is conducted. A VIF value less than 5 indicates no issue of collinearity. A VIF value above 5 and less than 10 indicates a moderate issue of collinearity. A VIF value larger than 10 implies a severe issue of collinearity.

2.3.2. Transformation of dependent variables

If the results imply that the distribution of the error score is not normally distributed, some techniques are needed to improve it. As suggested by Tabachnick and Fidell (2007), variable transformation

can be used for the dependent variable (Y). The logarithmic (Log 10) transformation is one of the most common transformations. Particularly, the logarithmic transformation is the most suitable transformation approach for this study, because the permeability of natural geological formations is usually assumed to be log-normally distributed (Chen and Zeng, 2015). The formula used in this study was “NEWX = LG10(X + C)”, where the constant C=17 was chosen because it creates the most ideal P-P plot. After the logarithmic transformation of the permeability, the regression model can be written as:

$$\text{Log}_{10}(Y+17) = \beta_1X_1 + \beta_2X_2 + \beta_3X_3 + \beta_4X_4 + \beta_5X_5 \quad (2-2)$$

After this transformation, the P-P plot usually shows that the empirical error scores heavily fall on the reference line. The Kolmogorov-Smirnov test also shows that the null hypothesis of normal distribution should not be rejected if the p-value is above 0.05.

2.3.3. Processing of potential outliers

An outlier in the MLR model is an observation that deviates noticeably from the major trend of the data. It can further influence the normality and linearity of the model. Therefore, it is necessary to remove the outlier data. There are several statistical methods which can be used for identifying outliers. The most frequently used one is the Cook’s distance (Stevens, 1984). If some points in the upper right, lower right and lower left of the graph imply that these points are outliers since they have the largest value on Cook’s distance or residual.

2.3.4. The Goodness-of-Fit for MLR model

In order to develop a meaningful model, we used the “forward selection” approach. This method adds one variable into the model at a time. In each step, each variable that is outside the model is tested for its relevance to the current model. The most significant of these variables is added to the model, so long as its P-value is below 0.5 significant level (Andersen and Rasmus, 2010). It is then necessary to measure how well the model fits the data. The statistical approach for measuring the goodness of fit is called the coefficient of determination (i.e., R^2 or R Square), which ranges from 0 to 1. More specifically, R^2 means the percentage variation in y that is explained by x-variables

or the entire regression model (Chatterjee, Samprit, and Ali S. Hadi., 2015). Therefore, the higher the R^2 , the better the hypothesized model fits the data.

2.3.5. Final mathematical expression of the MLR model

The final MLR model should include all the significant predictors for the permeability. Specifically, a positive coefficient for β_i represents a positive partial relationship between the predictor (independent variable) and permeability (dependent variable), whereas a negative coefficient indicates a negative partial relationship between them.

Because the logarithmic transformation was conducted only on the permeability, the interpretation of the partial effect resulting from the changes of the predictors was different from the scenario in which the logarithmic transformation is not performed. In addition, as mentioned before, the VIF value will be given associated with the estimation of the regression coefficient. If all of the VIF values are smaller than five, which are listed in the far right column of Table 2-2, then it suggests there is no perfect collinearity issue.

2.4. Results and Discussion

Figure 2-2 illustrates porosity distributions of the four different development stages. Specifically, the core sample porosity ranged primarily from 0.22 to 0.26. It is noticeable that the long-term waterflooding treatment raised the fraction of high porosity (e.g., comparing the fractions of 30% porosity between Stages 1 and 4), leading to increasing average porosity in the reservoir.

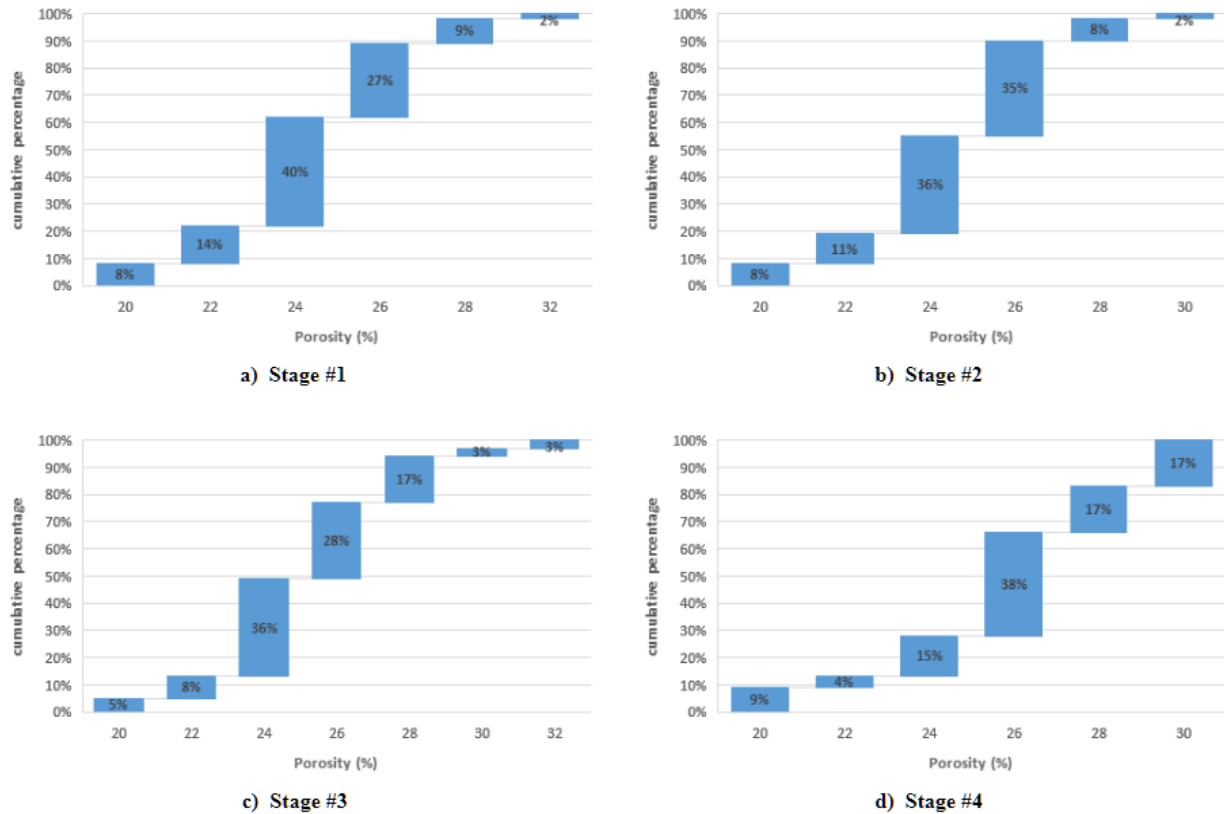


Figure 2-2. Porosity distribution in 1) Stage 1, 2) Stage 2, 3) Stage 3, and 4) Stage 4.

Figure 2-3 demonstrates the permeability distribution in the four development stages. The initial permeability of the reservoir (in Stage 1) was relatively low. The number fraction of cores that have permeability lower than 100 mD was about 66% and the highest permeability was lower than 500 mD. After a period of waterflooding treatment, the number fraction of cores that have permeability lower than 100 mD decreased to 27% and the average permeability of the entire reservoir increased noticeably (see Figure 2-3b). The peak permeability of Stage 2 reached 800 mD. With the waterflooding continued through Stage 3, the number fraction of permeability in the 200 mD-300 mD range increased. In Stage 4, the number fraction of low permeability decreased significantly and the peak permeability had reached 1000 mD. This suggests that the long-term waterflooding treatment had effectively increased the average porosity and permeability of the reservoir rock.

The overall variations of porosity and permeability reflect the overall effects resulting from the long-term waterflooding treatment. However, the effect of the waterflooding treatment is not the same for the four different formations even they are in the same reservoir.

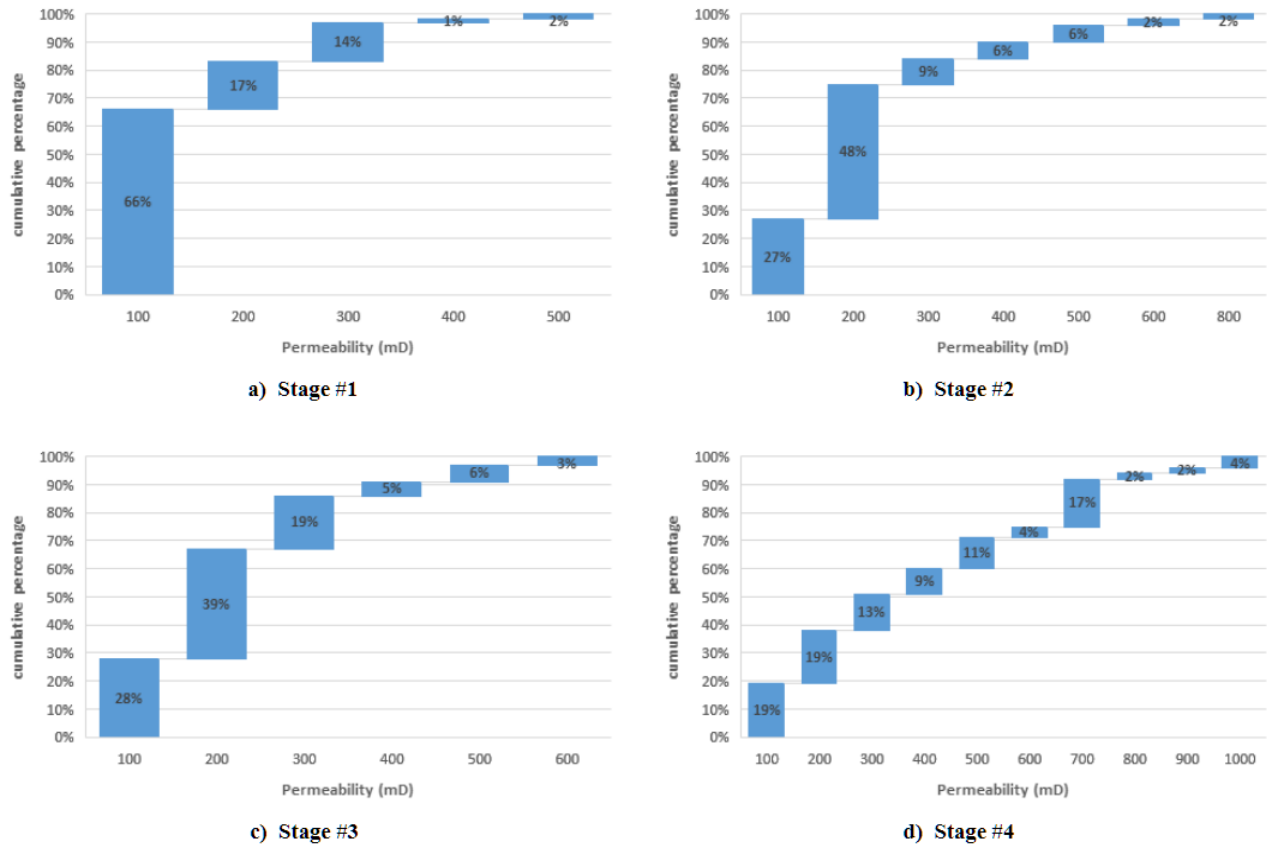


Figure 2-3. Permeability distribution in 1) Stage 1, 2) Stage 2, 3) Stage 3, and 4) Stage 4.

Figure 2-4 illustrates the distribution of porosity in the four formations in the reservoir. It is observed that the number fractions of high porosity (> 0.25) in Formations 1 through 3 increased with the development of long-term waterflooding treatments (from Stages 1 through 4). Conversely, the number fraction of high porosity (> 0.25) in Formation IV declined to a relatively low level when the waterflooding treatment developed into Stage 4. This confirms that the influence of long-term waterflooding on rock porosity was different on the four formations even they were in the same oilfield.

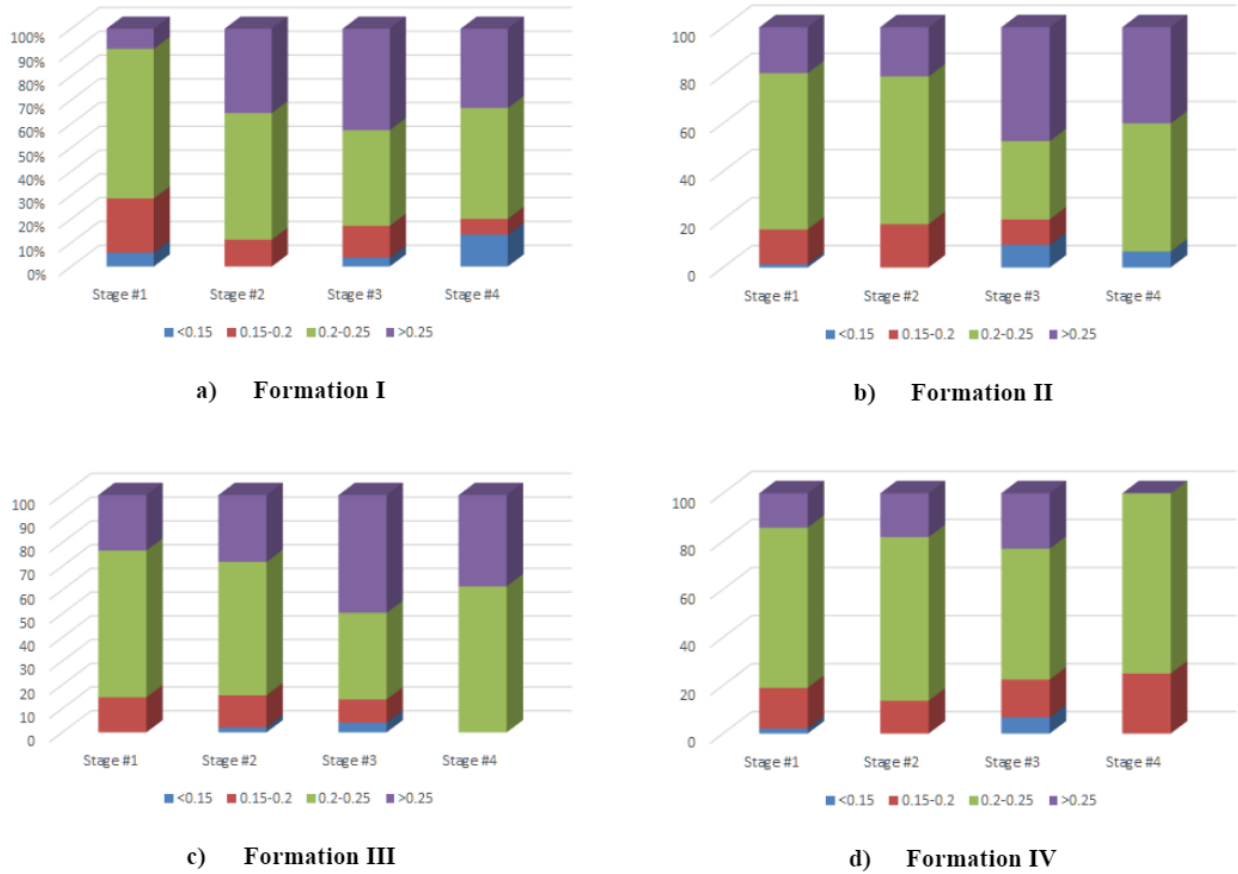


Figure 2-4. Porosity distribution in the four formations from Stage 1 through 4.

Figure 2-5 demonstrates the distribution of permeability in the four formations in the reservoir. It is found that the number fractions of relatively high permeability (500-1000 mD) in Formations 1 through 3 increased with the development of long-term waterflooding treatments (from Stages 1 through 4). Conversely, the number fraction of 500-1000 mD permeability in Formation IV continuously declined from Stage 1 through Stage 4. This suggests that the influence of long-term waterflooding on rock permeability was different on the four formations even they were in the same oilfield.

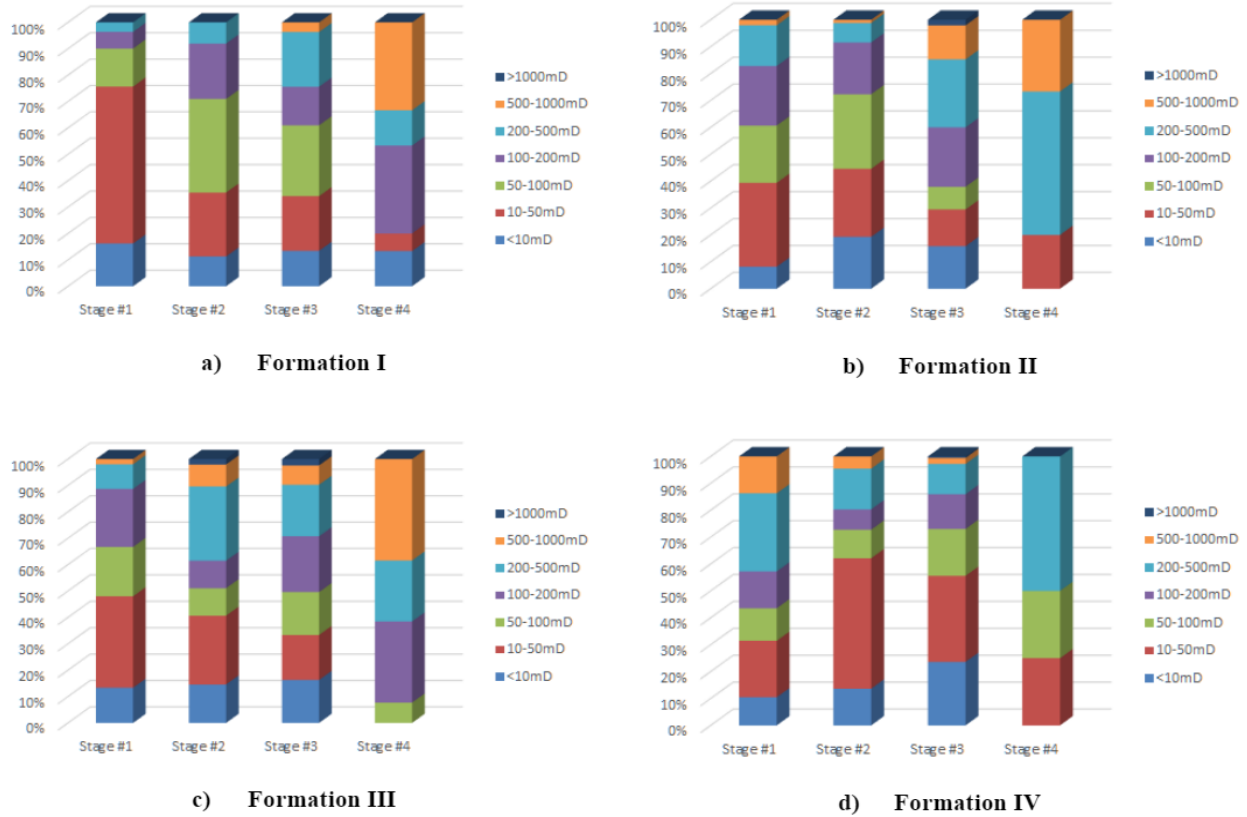


Figure 2-5. Permeability distribution in the four formations from Stage 1 through 4.

Figure 2-6 illustrates the X-ray CT images that show the variations of oil and water saturations during the core flooding experiments with increasing pore volumes (PV) of injection fluids. Specifically, the top row of CT images demonstrates the displacement process for water injection, whereas the bottom row of CT images illustrates the displacement process for polymer injection. The purple color indicates high oil content whereas the red color indicates high injection fluid content. The other colors indicate mixtures of oil and the injection fluid. The core sample was a high-permeability sandstone core sample extracted from an inspection well in Stage 4. The core sample porosity was 23.5%, and permeability was 643.8 mD. It is found that formation water injection led to significant development of preferential flow paths (i.e., fingering flow paths), which reduced the sweep efficiency of the displacement process. In contrast, the polymer fluid had raised viscosity and thus was able to form a piston-shaped displacement front, which was favorable for enhancing the sweep efficiency. The comparison between the top and bottom rows of CT images suggests that polymer flooding can be used as a promising EOR method after long-term waterflooding treatments.

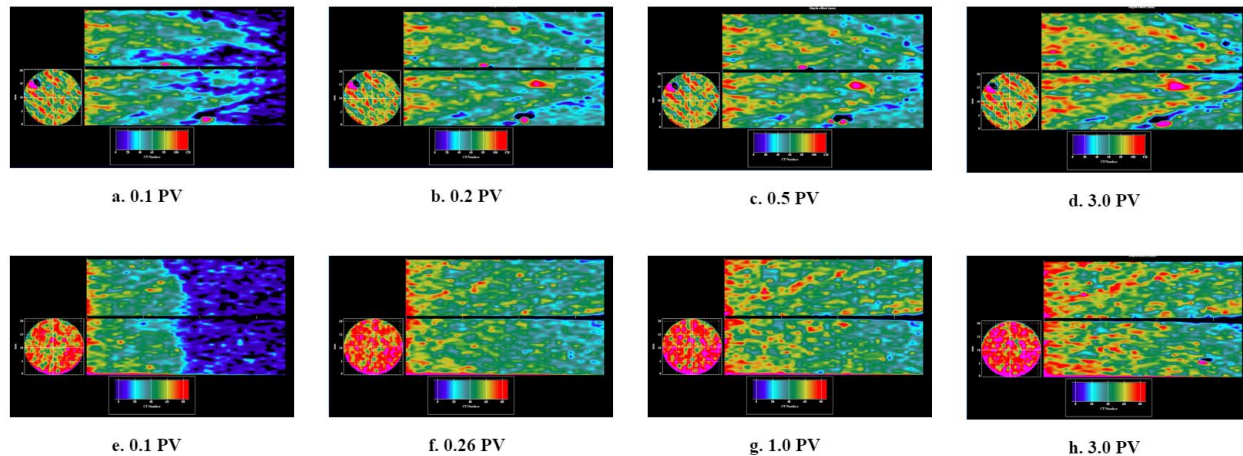


Figure 2-6. CT images of core-flooding experiments with different PVs. The top row of CT images demonstrates the displacement process for water injection, and the bottom row of CT images illustrates the displacement process for polymer injection. The purple color indicates high oil content whereas the red color indicates high injection fluid content. The other colors indicate mixtures of oil and the injection fluid.

The sensitivity testing results show that the long-term waterflooding treatment had an influence on velocity sensitivity and salinity sensitivity. The velocity sensitivity was mitigated gradually with the development of long-term waterflooding, i.e., and the reservoir rock became less and less sensitive to the water flooding velocity from Stages 1 through 4. This was because in the earlier stages of water flooding treatment, fine-sized clay grains in the reservoir rock were flushed and dislodged from the formation. Therefore, the average pore size, porosity, and permeability of the reservoir rock increased. When it came to Stage 4, the pore structure stabilized, and the remaining rock minerals cannot be dislodged easily, leading to decreased velocity sensitivity. For salinity sensitivity testing, the result shows that the salinity sensitivity increased with the development of long-term waterflooding treatment. This was because that the reservoir rock contains various clay minerals such as smectite, illite, kaolinite, and chlorite. These clay minerals have different expansion factors. Specifically, smectite has the maximum expansion factor, illite has the middle one, and kaolinite and chlorite have the minimum one. In a later stage of the waterflooding treatment, the low-expansion-factor minerals, such as kaolinite and chlorite, was dislodged by the waterflooding treatment. The remaining minerals were mainly illite and smectite. These high-expansion-factor clay minerals increased the salinity sensitivity of the reservoir rock in the later stages of the waterflooding treatment.

The mercury intrusion data provide details about the pore structure. The mercury intrusion data show that the trend of porosity and permeability variations are the same as those measured by laboratory porosimetry and permeameter. From Stages 1 through 4, the displacement pressure decreased continuously from -22.73% to -54.05% during the waterflooding process. This suggests that the waterflooding treatment increased the biggest pore throat radius and thus decreased the displacement pressure. Meanwhile, the structure coefficient was also reduced from -74.07% to -89.34%. Structure coefficient indicates the difference between the real pore structure and the pore structure of the parallel capillary bundles having the same pore size. The reduction of the structure coefficient showed that during the waterflooding process small-sized clay minerals were dislodged leading to improved pore connection. The sorting coefficient and relative sorting coefficient both decreased during the waterflooding process. A smaller sorting coefficient implies a more homogenous distribution of pore size. In addition, there was a large increase in the feature structure index. The larger feature structure index suggests a more uniform pore structure than before. Based on the above-mentioned results of mercury intrusion experiments, the mathematical relationships between these parameters will be investigated through the MLR modeling.

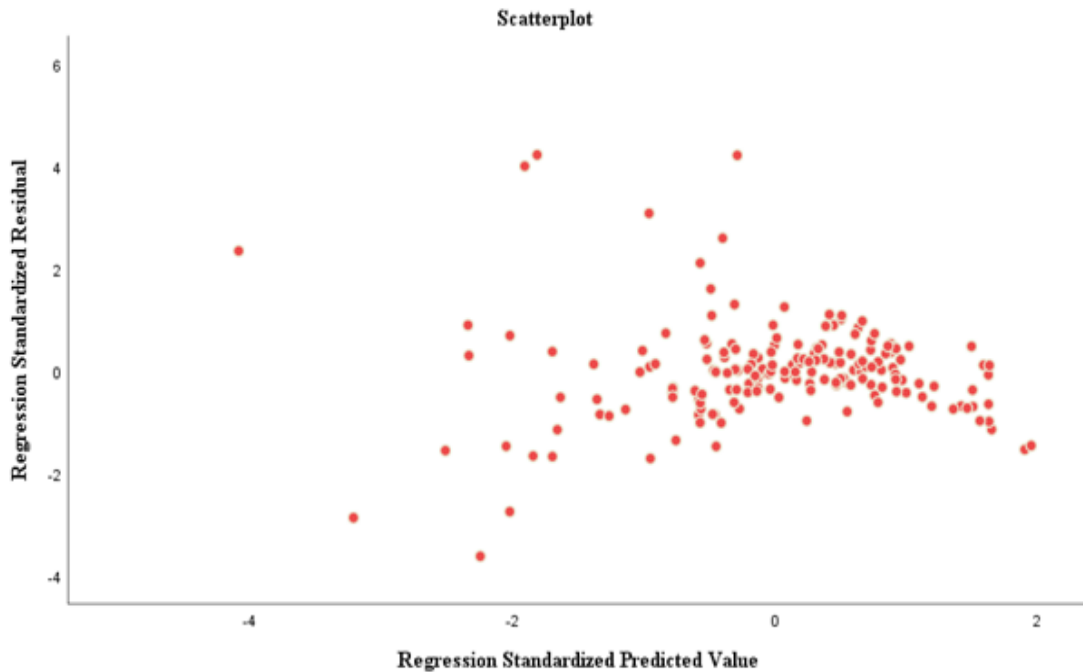


Figure 2-7. Regression standardized predicted value versus regression standardized residual.

The mercury intrusion data for the core samples extracted from Stage 2 were used to develop the MLR model. **Figure 2-7** illustrates that the regression standardized residual values from the MLR model were approximately uniformly distributed against the regression standardized predicted values. Therefore, it can be concluded that this assumption is satisfied and there are no potential outliers to be removed when it turns to the non-collinearity checking. **Table 2-1** illustrates the bivariate correlation matrix. The range of the correlation coefficient ranges from 0.299 to 0.742, which are all below 0.8. Therefore, there is no perfect collinearity issue in this model.

Table 2-1. Correlation between predictors, which include porosity (Φ), sorting coefficient (S_p), mean radius (\bar{r}), the omogeneous coefficient (α), and displacement pressure (P_d)

	φ	S_p	\bar{r}	α	P_d
φ	1	.625**	.742**	.661**	-.607**
S_p		1	.416**	.403**	-.665**
\bar{r}			1	.721**	-.369**
α				1	-.299**
P_d					1
** . Correlation is significant at the 0.01 level (2-tailed).					

The frequency distribution of permeability before the logarithmic transformation is a classic log-normal distribution. **Figure 2-8** shows the permeability distributions before and after the logarithmic transformation. Specifically, Figure 2-8a demonstrates that the permeability of the core samples approximately follows a log-normal distribution, which confirms that the permeability of natural geological formations can be modeled using a log-normal distribution (Chen and Zeng, 2015).

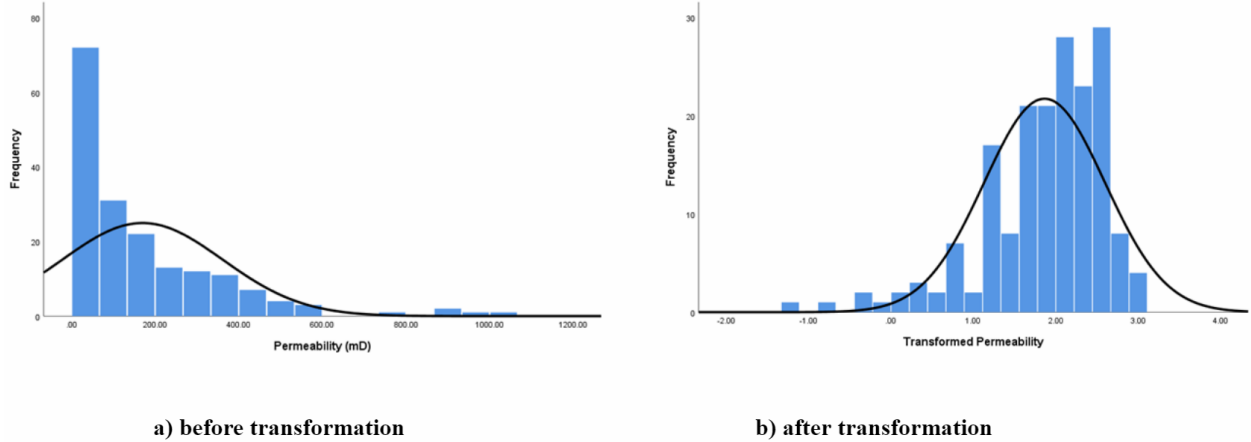


Figure 2-8. The frequency distributions of permeability a) before, and b) after the logarithmic transformation.

The next step is to check the goodness-of-fit for the MLR model. **Table 2-2** presents the information about the goodness-of-fit. In Model 1, the predictor porosity is included in the model. There was a 76.6% of total variance in the permeability. The mean radius was then added into the regression equation in Model 2. There was a total 82.4% of the variance in the permeability. Model 3 includes the predictors of porosity, mean radius, and sorting coefficient, leading to a total 84.8% of the variance in the permeability. The fourth and fifth predictors, the homogeneous coefficient and displacement pressure, were not included in the final MLR model because including these two predictors did not reduce the overall variance of the model to a noticeable extent.

Table 2-2. Goodness-of-fit Information. Model 1 includes the predictor of porosity, Model 2 includes the predictors of porosity and mean radius, and Model 3 includes the predictors of porosity, mean radius, and sorting coefficient.

Model	R Square	Std. Error of the Estimate	VIF
1	0.766	0.35630	1.000
2	0.824	0.30977	2.223, 2.223
3	0.848	0.28876	3.044, 2.242, 1.656

After the check of goodness-of-fit, the three predictors, the porosity, sorting coefficient, and mean radius, remained in the MLR model the coefficients of these predictors in the MLR model were then calculated. The final MLR model includes all the significant predictors for the

permeability. They were porosity, sorting coefficient, and mean radius. After the calculation, the standardized coefficients of the predictors are 0.468 for porosity, 0.199 for the sorting coefficient, and 0.381 for the mean radius. Therefore, the final mathematical regression equation for the core samples extracted from Stage 2 is written as follows:

$$\log_{10}(Y+17) = 0.468X_1 + 0.199X_2 + 0.381X_3 \quad (2-3)$$

Using the same modeling procedure, the MLR correlations for the core samples extracted from Stages 1, 3, and 4 are written as follows:

$$\text{Stage 1: } \log_{10}(Y+17) = 0.861X_1 + 0.173X_2 \quad (2-4)$$

$$\text{Stage 3: } \log_{10}(Y+17) = 0.557X_1 + 0.418X_3 \quad (2-5)$$

$$\text{Stage 4: } \log_{10}(Y+17) = 0.452X_1 + 0.565X_3 \quad (2-6)$$

where Y is the permeability, X_1 is the porosity, X_2 is the sorting coefficient, X_3 is the mean radius.

The variations of the coefficients in the MLR models through the four development stages during the waterflooding treatment agree with the petrophysical property variations measured in the laboratory experiments. In Stage 1, the reservoir had not been significantly influenced by the waterflooding treatment. In this situation, the original porosity and grain sorting coefficient can primarily decide the permeability of the reservoir rock. In Stage 2, the original pore structure had been influenced by the injection water. Fine-sized clay mineral particles that originally filled in the pore spaces were dislodged, leading to larger pore radius. Therefore, the porosity, grain sorting coefficient, and mean pore radius all had an impact on the permeability. In Stage 3, more and more large-radius pores became connected, so high-permeability flow channels started to develop, which greatly determine the permeability of the reservoir rock. The grain sorting coefficient played a negligible role and thus was removed from the MLR model. In Stage 4, the weight coefficient of the mean pore radius increased whereas the weight coefficient of the porosity decreased, which implies that the permeability was controlled by the high-permeability flow channels to a larger extent. The general trend of the change of reservoir petrophysical properties resulting from the

waterflooding treatment is the increase of reservoir heterogeneity. The cause for this was the development of high-permeability flow channels, which had a great impact on the permeability of reservoir. Mean pore radius is the petrophysical property that can represent the development of high-permeability channels and this value kept increasing from Stages 2 through 4.

2.5. *Conclusion*

The long-term waterflooding treatment had a noticeable influence on the petrophysical properties in a petroleum reservoir. The variations of permeability and porosity depended on the development stages through the waterflooding development history. The CT-scanned waterflooding experiments illustrated the distribution of water and oil saturations through the four different stages and showed that the polymer flooding led to a higher sweep efficiency because of the mitigation of viscous fingering. The velocity sensitivity decreased whereas the salinity sensitivity increased after the long-term waterflooding treatment. The mercury intrusion data not only provided more details of the pore structure but also contributed to the MLR model development. The MLR model output agreed well with the petrophysical property variations measured in the laboratory. The variations of the predictor coefficients in the MLR model illustrated the changes in the reservoir petrophysical characteristics through the four development stages.

The findings from this study advance the fundamental understanding of the role of long-term waterflooding treatment on oilfield developments. This work also provides valuable insight into the combination of reservoir petrophysical properties and MLR modeling. The outcome of this research will benefit geological reservoir simulations by providing insightful correlations between various reservoir petrophysical properties.

Chapter 3. Pore-scale Effects of Long-term Waterflooding Treatments on Reservoir Petrophysical Properties

3.1. Introduction

The petrophysical properties of a petroleum reservoir are constantly evolving, especially after decades of product development. The changes in the reservoir petrophysical properties should be identified and investigated, especially at the microscopic level, in order to benefit the enhanced oil recovery processes, because the petrophysical properties at the microscopic scale dictate the larger-scale multiphysics processes that can be observed and measured directly. A series of core samples, extracted from a developed oilfield located in Northeastern China, was extracted and classified according to the development stages. With these samples, a series of laboratory experiments was conducted, such as the casting thin sections (CTS) imaging and scanning electron microscope (SEM) imaging. Both of these two imaging tests showed the evolution of the pore-level characteristics during the waterflooding treatments. Because rock surface wettability has a significant impact on fluid flow, the relative permeability curves of certain core samples were plotted to identify the change of wettability. Based on the tests mentioned above, the changes of pore structure and wettability during the long-term waterflooding treatments can be determined. In addition, because high-permeability channels cause high water content in production fluids, a special 2D microfluidic equipment that simulates the pore structure of a sandstone formation was developed to investigate the influence of injection flow rate on the development of high-permeability channels. Based on these experiments, the improved understanding of the changes of reservoir petrophysical properties at the pore-scale level after long-term-waterflooding treatments will provide valuable insights into the subsequent production strategies.

Keywords: waterflooding, petrophysical properties, high-permeability channel, pore-scale, microfluidic

3.2. Methodology

3.2.1. Casting thin section imaging

The entire process of the CTS imaging method contains sampling, casting, making the section, and section analysis, etc. We selected representative samples and then the casting machine was used to make the casting sections. The casting sections were polished to a thickness of 0.03 mm and then observed under optical microscopy. In this study, the casting thin sections from the core samples extracted from the four development stages were fabricated and scanned in order to analyze the changes in petrophysical properties

3.2.2. Scanning electron microscopy

The advantages of SEM imaging include simple sample preparation procedures, high resolution, and deep depth of field. The sample in SEM imaging should be dry and have sufficient electrical conductivity (Chen et al., 2013). In this paper, we scanned several sandstone samples from the four development stages of the oilfield and then studied the variations in the microscopic structural properties.

3.2.3. Wettability and relative permeability curves

The wettability of the rock surfaces in a reservoir is a critical petrophysical property. The wettability determines the direction of the capillary force and influences the fluid flow and bound water content, which suggests that the wettability has a great influence on the oil recovery in the reservoir. A series of laboratory experiments was carried out to determine the relative permeability curves of the core samples extracted from the four development stages. The relative permeability curves were used to infer the wettability of the rocks. Specifically, the relative permeability curves measured from the four development stages were compared with each other to identify the role of long-term waterflooding treatments on rock wettability. In addition, the standardization method developed by Chen (1990) was used to merge the relative permeability curves and plot them together, because the core samples extracted from different development stages had various porosity and permeability.

3.2.4. 2D microfluidic model

2D microfluidic experiments, based on the CTS images and the photochemical etching technique, were designed and conducted in order to investigate the role of the injection flow rate and injection fluid volume on the development high-permeability flow channels. Specifically, the pore geometry

in the microfluidic models was designed based on the CTS images of the core samples extracted from Stage 4. The dimensions of the microfluidic model were 55 mm × 25 mm × 3 mm in the length, width, and thickness directions, respectively. The wettability of solid surfaces in the microfluidic model was water wet. The permeability of the model was around 600 millidarcy (mD). **Figure 3-1** illustrates the two microfluidic models used in this study. It should be noted that the dimensions of the pore geometries in the two microfluidic models were magnified around 10 times compared to the original pore geometry in the sandstone formation. Therefore, varying injection flow rates, ranging from 1 $\mu\text{l}/\text{min}$ to 10 $\mu\text{l}/\text{min}$, were used in the flooding experiments to achieve a wide range of Reynolds (Re) numbers in order to match the Re numbers in the real sandstone system.

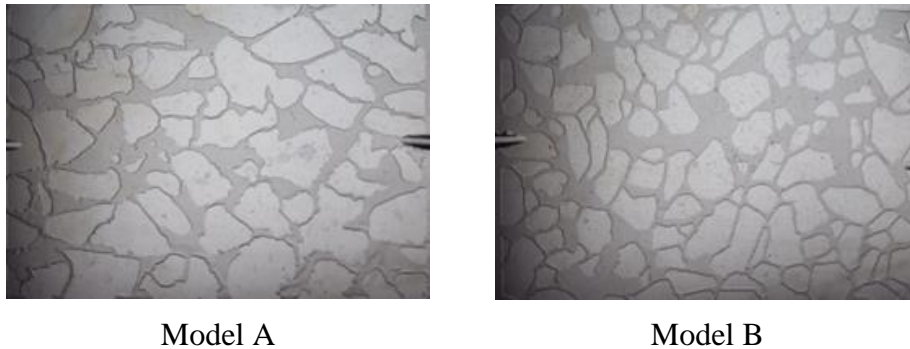


Figure 3-1. Two microfluidic flow models used in this study. Their pore geometries were both from the CTS images of the core samples extracted from Stage 4. The pixel dimensions of the images were 212×148 pixels in the x and y directions, respectively. The image resolution was $141 \mu\text{m}$ per pixel. The pore size in the models ranged from $200 \mu\text{m}$ to $400 \mu\text{m}$. In the microfluidic models, the flow inlet was at the right side, and the flow outlet was on the left side. The flow direction was thus horizontal and from right to left.

The microfluidic experiments were conducted under the temperature of 25°C . The first step was to vacuum the microfluidic model. The pore structure was then saturated with water followed by saturation of oil. The oil viscosity was $1.78 \text{ mPa}\cdot\text{s}$, and the water viscosity was $0.89 \text{ mPa}\cdot\text{s}$. After 24 hours, the model was placed under the optical microscope for flooding experiments. Water, with methylene blue as the dye tracer, was injected into the microfluidic model to displace the oil in pore space. Varying water injection flow rates were used to study the relationship between injection flow rate and sweep efficiency. The entire process was recorded by a high-speed

camera. We conducted in total ten groups of flooding experiments for each model. The injection flow rates ranged from 1 ul/min to 10 ul/min.

3.3. Results and Discussion

Figure 3-2 demonstrates the thin sections of core samples selected from Stage 1 to Stage 4. The CTS scanning image from Stage 1 shows the pore geometry of rock samples extracted from an inspection well in the early development stage of waterflooding. The grain particles were primarily fine sized in Stage 1. The main minerals include quartz and feldspar. With the development of waterflooding treatments, Figure 3-2 illustrates that the grain sizes became more and more coarse because relatively fine particles were dislodged by the injected water. In addition, through the development stages, it is observed that the roundness of grain particles was enhanced.

According to the results of CTS imaging, the samples from Stage 3 had an average porosity of 10.7%. In comparison, the samples from Stage 4 had porosity ranging from 18% to 35% with an average value of 27.2%. This confirms that the porosity of the reservoir rock increased with the development of waterflooding treatments because fine particles were dislodged from the pore spaces. In addition, intergranular cementing materials were also removed after long-term waterflooding, contributing to higher porosity in the later stage of waterflooding treatment. Furthermore, the long-term waterflooding treatments caused the dissolution of rock matrices and thus promoted the development of secondary porosity in the rock formation.

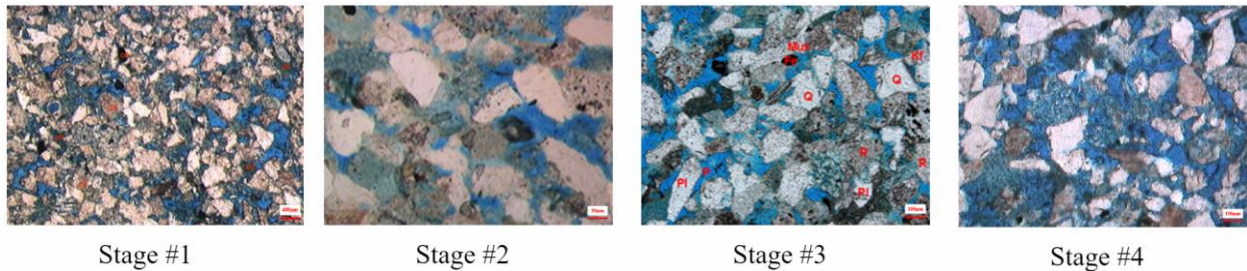


Figure 3-2. The thin section core samples selected from Stage 1 to Stage 4 in the waterflooding development history.

Figure 3-3 illustrates the SEM images of the core samples extracted from different development stages. The images were grouped by various minerals from left to right, including quartz, feldspar, kaolinite, and illite. It is found that the primary pore structural changes of these core samples resulted from dissolution by observing the SEM images from Stage 1 through Stage

4. Pore-scale erosion can be found in Stage 4. Anderson (1987) found that the wettability of rock surfaces could change and even reverse under the impact of long-term waterflooding treatments. This is because oil-wet materials on rock surfaces can be corroded and removed after long-term waterflooding, leading to more water-wet rock surfaces and consequently reduced contact angles.

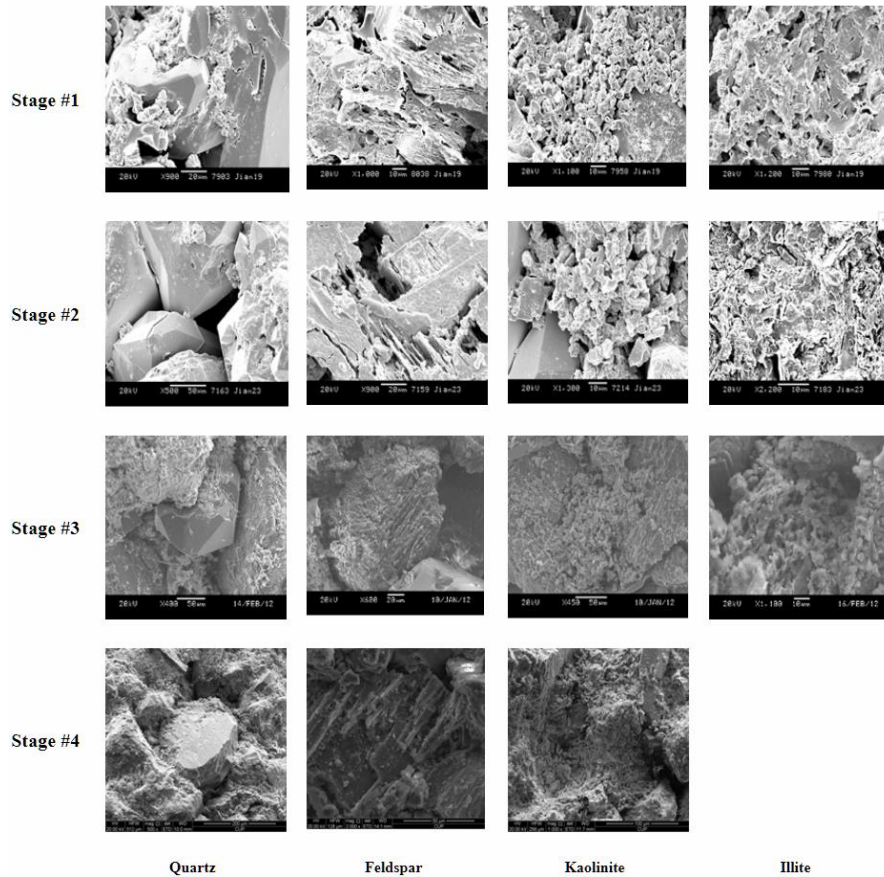


Figure 3-3. SEM images from Stage 1 through Stage 4. The four column (from left to right) account for various mineral components.

Figure 3-4 demonstrates the relative permeability curves measured on core samples extracted from Stages 2, 3, and 4. Specifically, the red, yellow, and blue markers are for Stages 2, 3, and 4, respectively. Comparison between these three development stages clearly illustrates the influence of long-term waterflooding treatments on the relative permeability of the reservoir rock. The oil relative permeability curve continuously increased from Stages 2 through 4, which implies that the oil relative permeability was enhanced through the waterflooding treatments. In addition, the water saturation, at which the water and oil relative permeabilities are equal to each other, continuously increased with the development of waterflooding. These phenomena suggest that the long-term

waterflooding treatments reduced the contact angle and thus made the reservoir rock more water-wet, which consequently enhanced the mobility of the non-wetting fluid (oil). This experimental finding is consistent with what we found in a recent numerical study in which lattice Boltzmann two-phase flow modeling was used to study the role of contact angle variation on the relative permeability curves (Fan et al., 2019).

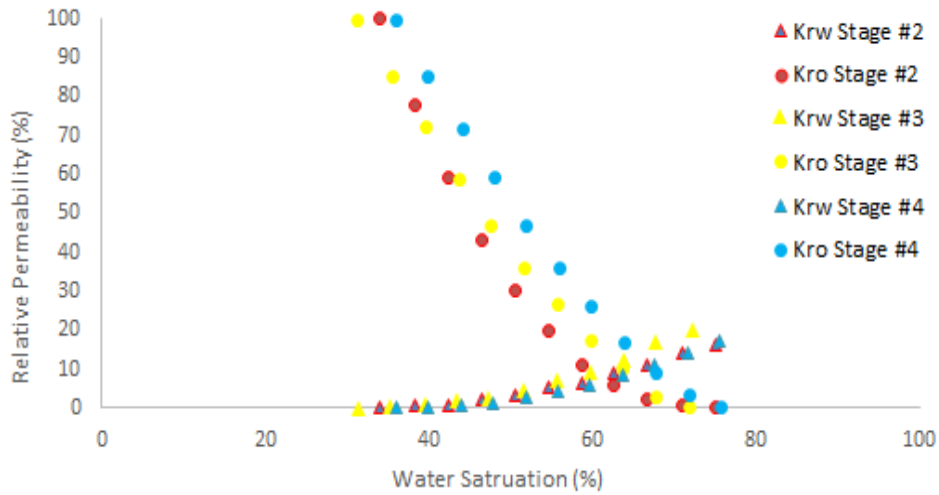


Figure 3-4. Relative permeability curves measured on core samples extracted from Stages 2, 3, and 4. Specifically, the red, yellow, and blue markers are for relative permeabilities of Stages 2, 3, and 4, respectively

Figure 3-5 illustrates the displacement process in Model A with a water injection flow rate of 5 ul/min. The pore geometry was from the CTS imaging results of Stage 4. Flow direction is from right to left. The blue fluid is water, and the yellow fluid is oil, which initially occupies the pore space. The interval between snapshot pictures is 5 seconds. It can be observed that with the increase of time injected water gradually started to sweep oil in the transverse direction.

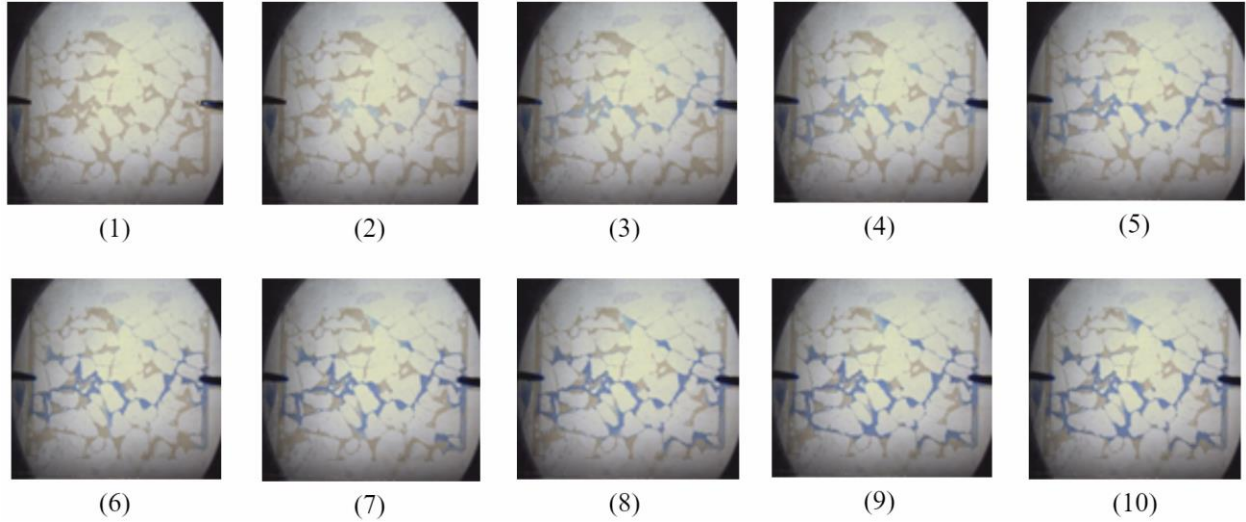


Figure 3-5. Displacement process in Model A with a water injection flow rate of 5 ul/min. The pore geometry was from the CTS imaging results of Stage 4. Flow direction is from right to left. The blue fluid is water, and the yellow fluid is oil, which initially occupies the pore space. The interval between snapshot pictures is 5 seconds.

Figures 3-6 and 3-7 demonstrate the moments when the injected water achieved the breakthrough through the microfluidic models A and B, respectively. Varying injection flow rates were tested, including 1 ul/min, 3 ul/min, 5 ul/min, 7 ul/min, and 10 ul/min. The breakthrough pore volumes (PVs) for these flow rates in Model A were, 0.58 PV, 0.66 PV, 0.31 PV, 0.10 PV, and 0.48 PV, respectively. The breakthrough PVs for these flow rates in Model B were, 0.49 PV, 0.61 PV, 0.32 PV, 0.12 PV, and 0.55 PV, respectively. In both models, the injection flow rate of 3 ul/min resulted in the highest sweep efficiency. When the injection flow rate was higher than 3 ul/min, viscous fingering occurred and thus led to lower sweep efficiency. Our microfluidic experimental results are different from the findings of Wei et al. (2014), where they found that the sweep efficiency increased with the increasing injection flow rate. This was because that in the laboratory experiments of Wei et al. (2014) the PV of injection fluid was 50, much higher than that in this study. In this study, the sweep efficiency was calculated when the injected water achieved breakthrough (i.e., the injected water arrives at the outlet and thus forms connected flow channels between the inlet and outlet), which corresponded to a PV less than one. We expect that a higher injection flow rate will be favorable for enhancing the final sweep efficiency if the PV of injection water is adequately high. This hypothesis will be tested in our future study.

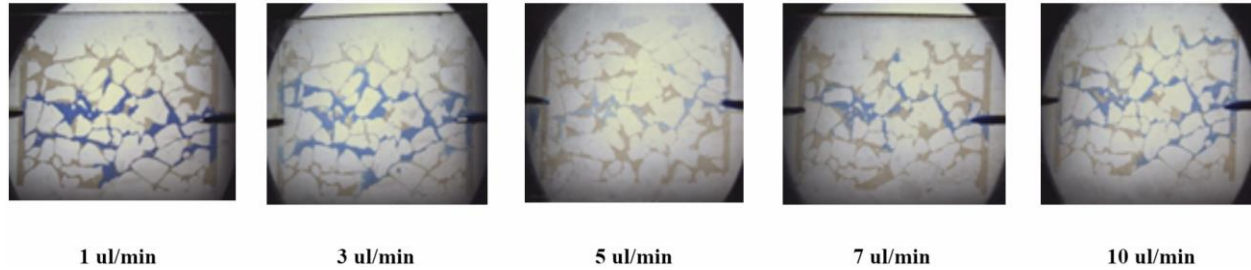


Figure 3-6. Breakthrough moments in Model A with different injection flow rates

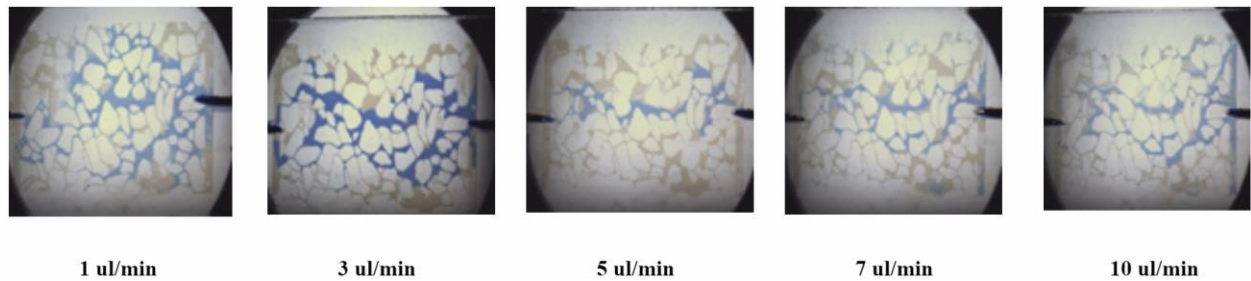


Figure 3-7. Breakthrough moments in Model B with different injection rates

Figure 3-8 illustrates that rectangular grids were utilized to divide the model images. The grid spacing was 10 mm. The model images were divided into five zones along the center streamline. Zone 1 is at the center of the microfluidic model in the streamline direction, and Zones 2, 3, 4, and 5 are sequentially located in the transverse direction. The microfluidic model images at the breakthrough moments were selected to analyze. The sweep efficiency (fraction of pore space area displaced by injection water) of each zone was calculated. The weighted average of the sweep efficiency of the entire microfluidic model was then calculated because the zones had different areas and thus had different weights in the contribution to the total sweep efficiency. **Figure 3-9** demonstrates the weighted average of sweep efficiency as a function of the injection flow rate. It is clear that, when the injected water broke through, the flow rate of 3 $\mu\text{l}/\text{min}$ led to the highest overall sweep efficiency, which is consistent with the visual observations in Figures 3-7 and 3-8.

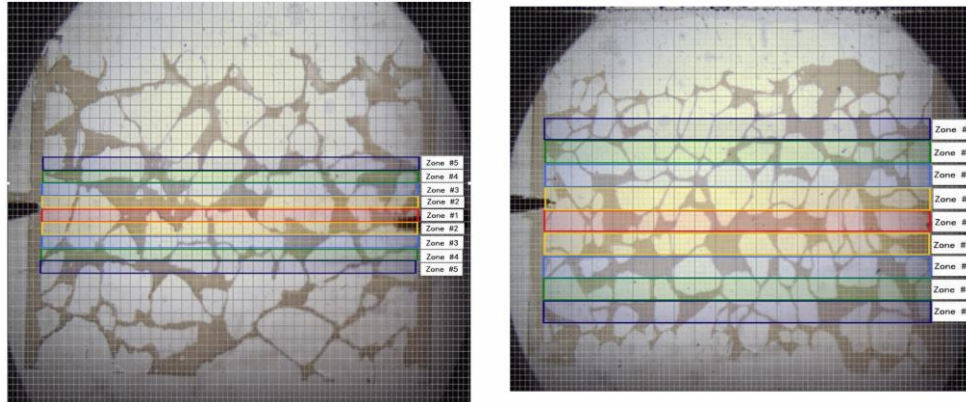


Figure 3-8. Zone divisions in Model A and Model B. Zone 1 is at the center of the microfluidic model in the streamline direction, and Zones 2, 3, 4, and 5 are sequentially located in the transverse direction.

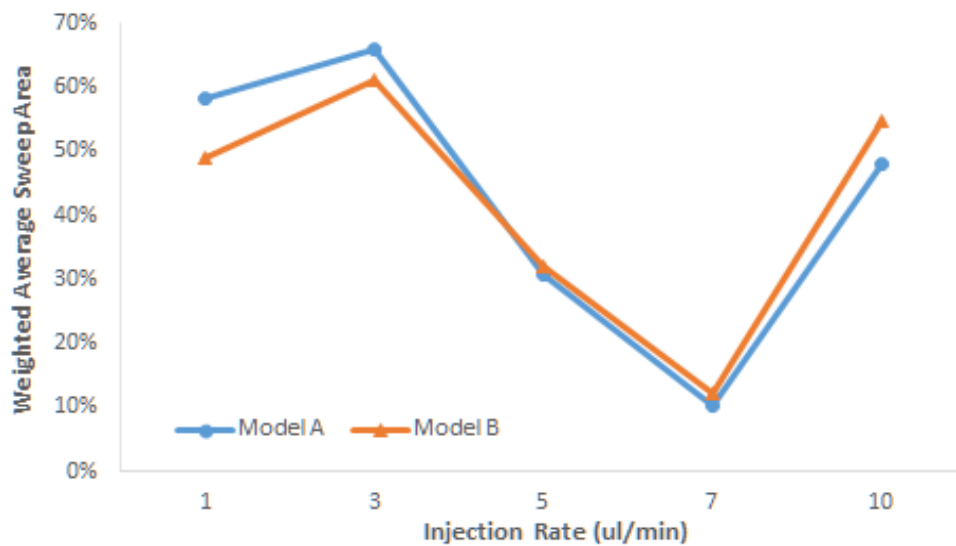


Figure 3-9. The weighted average of the sweep efficiency as a function of the injection water flow rate.

Figure 3-10 demonstrates the distribution of the sweep efficiency in each zone when the injected water reached breakthrough in Model A. It is clear that the sweep efficiency was relatively uniform across all zones when the injection water flow rate was not higher than 3 $\mu\text{l}/\text{min}$. When the flow rate exceeded 3 $\mu\text{l}/\text{min}$, noticeable viscous fingering developed and as a consequence the sweep efficiency in Zone 1 was significantly higher than those in the other zones, leading to reduced overall sweep efficiencies for the flow rates of 5 $\mu\text{l}/\text{min}$ and 7 $\mu\text{l}/\text{min}$. The same analysis

of sweep efficiency distribution was conducted for the five zones in Model B, and the result is presented in **Figure 3-11**. Similarly, it can be observed that when the flow rate exceeded 3 $\mu\text{l}/\text{min}$, viscous fingering developed and thus led to reduced overall sweep efficiencies for the flow rates of 5 $\mu\text{l}/\text{min}$ and 7 $\mu\text{l}/\text{min}$.

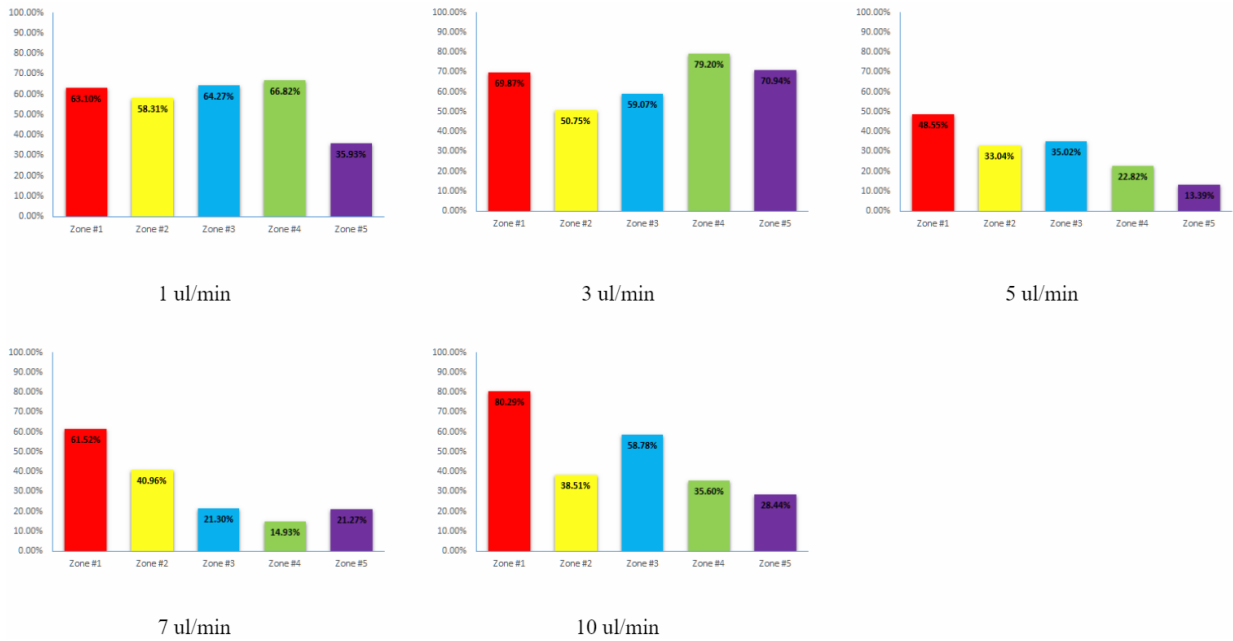


Figure 3-10. Distribution of the sweep efficiency in each zone when the injected water reached a breakthrough in Model A.

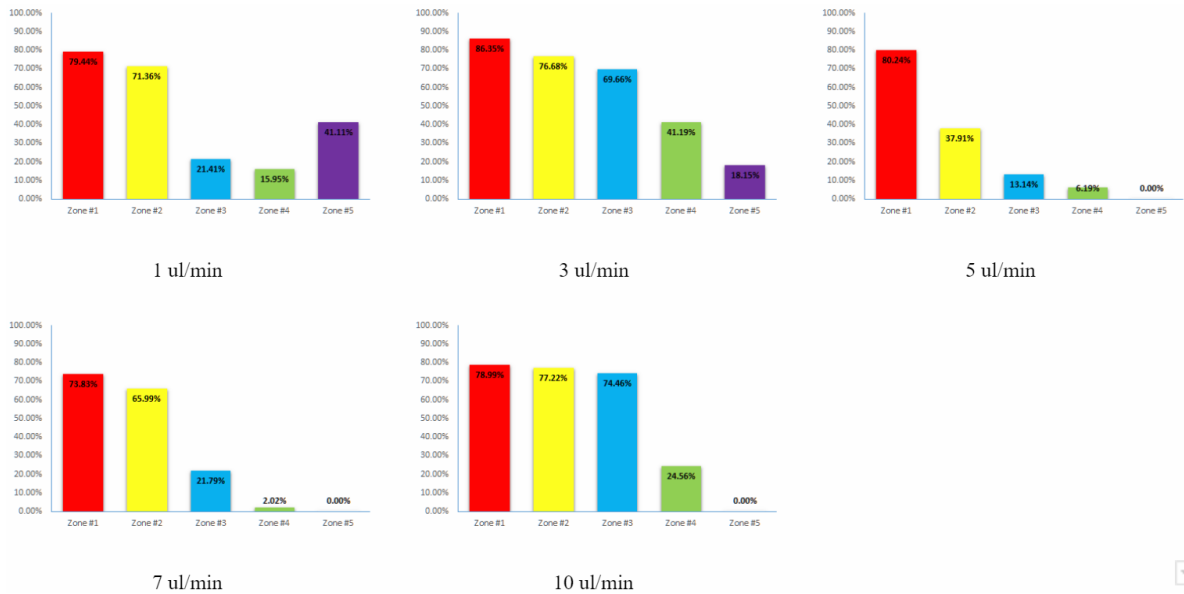


Figure 3-11. Distribution of the sweep efficiency in each zone when the injected water reached a breakthrough in Model B.

breakthrough in Model B.

3.4. Conclusion

In this study, various laboratory experimental techniques were utilized to study the pore-scale effects of long-term waterflooding treatments on the changes in reservoir petrophysical properties. 2D microfluidic flow models were developed, in which the pore geometries were based on CTS imaging data. With the development of long-term waterflooding treatments, fine particles in the reservoir rock were dislodged, leading to coarser grain sorting. In addition, the cementing materials in the pore spaces between particles were also removed due to waterflooding. These pore-scale processes resulted in the increase of pore space size and consequently increasing rock porosity and developments of preferential flow paths. Rock surface corrosion and dissolution due to the long-term waterflooding treatments were proved by using high-resolution SEM imaging. Laboratory relative permeability measurements, based on the unsteady-state method, demonstrated that the long-term waterflooding treatments caused the increase of oil relative permeability. This implies that the waterflooding processes reduced the contact angle at rock surfaces and thus led to a more water-wet formation. Microfluidic core flooding experiments illustrated the development of viscous fingering (i.e., preferential flow channels of the injected fluid) when the injection water flow rate was higher than a certain level, which resulted in reduced overall sweep efficiency.

The findings from this study advance the fundamental understanding of the role of long-term waterflooding treatment on the changes of reservoir petrophysical properties at the pore scale. Specifically, pore-scale variations of pore structure geometry, mineral composition, relative permeability and contact angle, and sweep efficiency, which was due to long-term waterflooding development, were identified and investigated. This work also provides valuable insights into the role of injection flow rate on the displacement efficiency in the later stage of waterflooding developments.

Chapter 4. Comprehensive laboratory investigation of Klinkenberg Effect and its role on apparent permeability in various U.S. shale formations

4.1. Introduction

Hydraulic fracturing in shales is challenging because of the complicated stress status. The confining pressure imposed on a shale formation has a tremendous impact on the permeability of the rock. The correlation between confining pressure and rock permeability is complicated and might be nonlinear. Gas flow in low-permeability shales differs significantly from liquid flow because of the Klinkenberg effect, especially when the pore pressure is relatively low. The Klinkenberg effect results from gas molecule slip at the solid walls inside the nanopores, where the collision between gas molecules and solid surfaces is more frequent than the collision between gas molecules. This effect causes the increase of apparent permeability (i.e., the measured permeability). In this study, the simple effective stress law and the effective stress coefficient law were used to study the relationship between permeability and effective stress. In the simple effective stress law, the effective stress is calculated as the difference between confining pressure and pore pressure. The Klinkenberg coefficient and the effective mean pore radius can then be calculated. In the effective stress coefficient law, there is an effective stress coefficient (i.e., the Biot coefficient) which controls the influence of pore pressure on the effective stress. In this study, the effective stress coefficient was obtained by analyzing a large number of laboratory data measured under varying pore pressures and confining pressures. Specifically, the permeabilities of core samples extracted from four U.S. shale formations were measured using a pulse decay permeameter under varying combinations of confining and pore pressures. The samples were cored in the directions parallel to and perpendicular to the shale bedding planes, in order to test the role of bedding plane direction on the measured permeability. Laboratory results demonstrate that the permeabilities of all core samples fell in the range between 10^{-2} millidarcy (mD) and 10^{-4} mD. In the same formation, the permeabilities of the core samples in which the bedding planes were in the longitudinal direction were about one order of magnitude higher than the permeabilities of the core samples in which the bedding planes were in the transverse direction. Using the simple effective stress law, the Klinkenberg effect was observed, because the measured apparent permeability decreased with increasing pore pressure. Using the effective stress coefficient law, the effective stress coefficient was found around 0.5, which suggests that the pore pressure had a

less influence on the effective stress compared to the confining pressure. These comprehensive laboratory experiments demonstrate the role of confining pressure, Klinkenberg effect, and bedding plane direction on the gas flow in the nanoscale pore space in shales. These experimental data will be valuable in validating and calibrating pore- to core-scale numerical models of the flow and transport properties in shale formations.

Keywords: Apparent permeability, Klinkenberg effect, Pulse decay, Effective stress coefficient, Shale.

4.2. Overview of the Experiment/Analysis Workflow

This section aims to provide an overview of the experiment workflow. Details of experimental setup will be given in a later section. In this work, an experiment/analysis approach was developed to study the correlation between apparent permeability, k_a , and the effective stress, P_e . First, a series of shale core samples, containing different bedding plane directions, were extracted from four U.S. shale formations. Second, a pressure pulse decay permeameter was used to measure core permeabilities with a wide range of various combinations of P_p and P_c . Third, the simple effective stress law was used to calculate the effective stress and to derive the Klinkenberg coefficient, b , and the mean pore radius, r , which are the petrophysical properties of core samples but vary when the effective stress varies. Fourth, the laboratory experimental data were fitted to the model based on the effective stress coefficient law, and the effective stress coefficient, χ , was obtained for each core sample

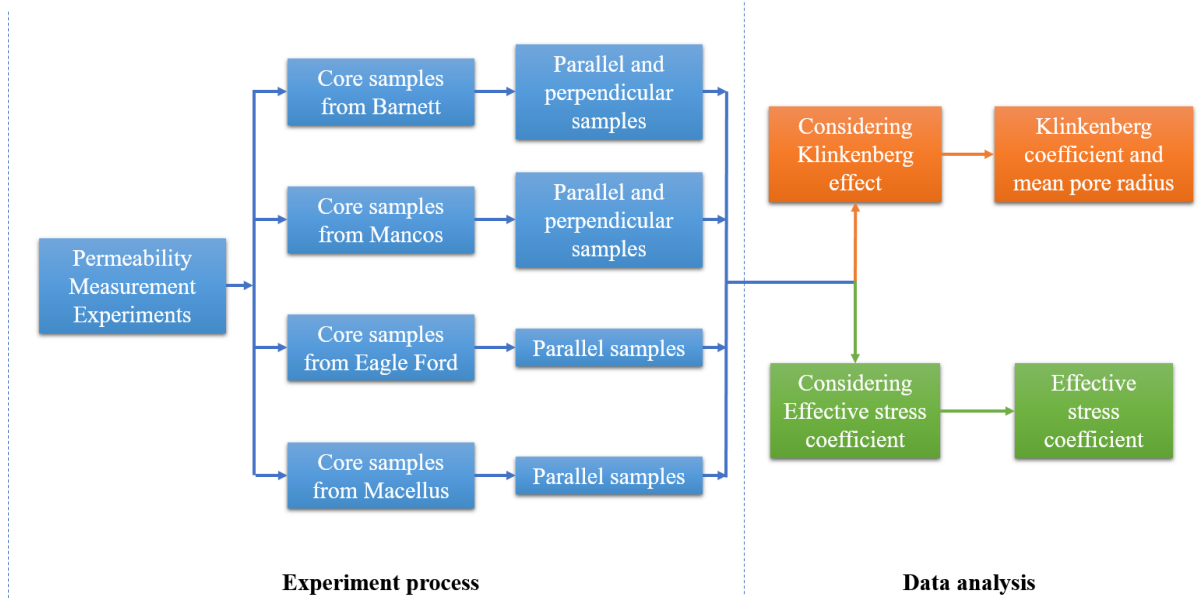


Figure 4-1. An experiment/analysis workflow for the assessment of the correlation between apparent permeability, confining pressure, and effective stress.

In this study, based on the simple effective stress law, we selected 500 psi, 1000 psi, and 1500 psi as the values of the effective stress, P_e , for each core sample. For each effective stress value, eight pore pressure values (100 psi, 300 psi, 500 psi, 700 psi, 900 psi, 1100 psi, 1300 psi, and 1500 psi) were tested using the pulse decay permeameter, and the confining pressures were calculated as the sum of the pore pressures and the particular effective stress based on the simple effective stress law. Therefore, we conducted in total 24 pulse decay experiments for a single shale core sample which was subjected to different combinations of P_e and P_p . The experimental results of the cores containing different bedding plane directions were compared with each other to unravel the role of bedding plane direction on the core permeability. The same experimental data were then used to fit the effective stress coefficient law and consequently to find the effective stress coefficient, χ .

4.3. Models and Experimental Equipment

4.3.1. Simple effective stress law and Klinkenberg equation

It is the Klinkenberg effect that leads to the difference between apparent permeability and absolute permeability, especially under low pore pressure. Using the simple effective stress law, the effective stress, P_e , is calculated as $P_e = P_c - P_p$. In order to quantify the Klinkenberg effect, the

Klinkenberg coefficient (Klinkenberg, 1941) was used to describe the role of pore pressure on the apparent permeability. The Klinkenberg coefficient depends on the petrophysical properties of the rock, and is included in the Klinkenberg equation written as follows:

$$\frac{k_a}{k} = 1 + \frac{b}{P_p} \quad (4-1)$$

where k_a is the apparent permeability (m^2), P_p is the pore pressure (Pa), k is the absolute permeability of the porous medium (m^2), and b is the Klinkenberg coefficient which is expressed as (Chen, 2016)

$$b = \frac{\mu}{r} \left(\frac{2}{\alpha} - 1 \right) \sqrt{\frac{8\pi RT}{M}} + \frac{16\mu}{3r} \sqrt{\frac{8RT}{\pi M}} \quad (4-2)$$

where μ is dynamic viscosity (Pa·s); α is the tangential momentum accommodation coefficient with a value from 0 to 1; R is the gas constant and equal to 8.314 J/mol/K; T is the absolute temperature (K); M is molar mass (kg/mol); and r is the effective pore radius (m). Using Equation 4-2, one can calculate r as:

$$r = \frac{\mu}{b} \left(\frac{2}{\alpha} - 1 \right) \sqrt{\frac{8\pi RT}{M}} + \frac{16\mu}{3b} \sqrt{\frac{8RT}{\pi M}} \quad (4-3)$$

4.3.2. Effective stress coefficient law

The effective stress coefficient law assumes that P_e is not simply the difference between confining pressure and pore pressure ($P_c - P_p$) but is written as (Bernabe, 1986):

$$P_e = P_c - \chi P_p \quad (4-4)$$

where P_e is effective stress (Pa), P_c is confining pressure (Pa), P_p is pore pressure (Pa), and χ is the effective stress coefficient, whose value depends on the specific rock mineral composition. Equation 4-4 suggests that the effective stress has different sensitivities to the confining pressure and pore pressure if the value of χ is not equal to one. The basic assumption of the effective stress

coefficient law is that the permeability depends on the effective stress, which controls the pore geometry and pore size in the rock. If the effective stress stays the same, then the permeability is a constant.

Because P_e is a function of P_p and P_c , k can be written as a function of these two variables:

$$k = k(P_c, P_p) \quad (4-5)$$

Because the permeability of natural geologic formations in general follows a lognormal distribution (Chen and Zeng, 2015), we use $\log(k)$ as an indicator of the formation permeability and then have:

$$\log(k) = \log(k)(P_c, P_p) \quad (4-6)$$

Based on Equation 4-6, one obtains the differential of $\log(k)$:

$$d\log(k) = \left(\frac{\partial \log(k)}{\partial P_c} \right) dP_c + \left(\frac{\partial \log(k)}{\partial P_p} \right) dP_p \quad (4-7)$$

One also has the following equation based on Equation 4-4:

$$dP_e = dP_c - \chi dP_p \quad (4-8)$$

When the effective stress stays constant, both $d\log(k)$ and dP_e are zero. Therefore, one obtains:

$$\left(\frac{\partial \log(k)}{\partial P_c} \right) dP_c + \left(\frac{\partial \log(k)}{\partial P_p} \right) dP_p = 0 \quad (4-9)$$

and

$$dP_c - \chi dP_p = 0 \quad (4-10)$$

Using Equations 4-9 and 4-10, one obtains:

$$\chi = -\left(\frac{\partial \log(k)}{\partial P_p}\right) / \left(\frac{\partial \log(k)}{\partial P_c}\right) \quad (4-11)$$

4.3.3. Pressure pulse decay experiment

The pressure pulse decay permeameter (PDP) equipment is convenient, dynamic approach to measuring the permeability of tight rocks. Jones (1997) developed the basic measurement principle of PDP. He found that the measurement range of PDP is from 0.1 mD to 0.01 microdarcy (μD). As opposed to traditional permeability measurement methods, which use flow parameters in the steady state and are based on Darcy's law, the PDP method uses transient flow parameters, which significantly accelerates the measurement process and consequently is ideal for low-permeability rocks. **Figure 4-2** is a schematic plot of the PDP setup. The flow rate measurement is not required but can be calculated from the known volumes of the reservoirs, fluid compressibility, and the rate of change of gas pressures (Hseih et al., 1981; Bourbie and Walls, 1982).

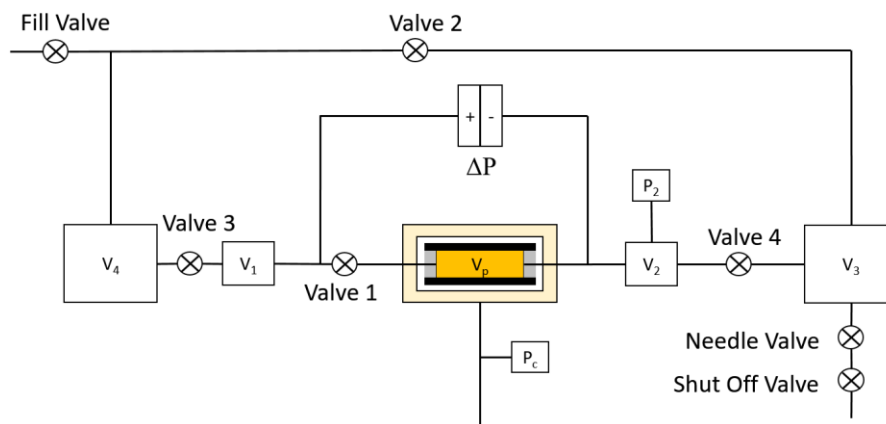


Figure 4-2. Schematic PDP equipment setup, which consists of an upstream test gas reservoir having a volume of V_1 , a high-pressure core holder with the pore volume of V_p , a downstream gas reservoir having a volume of V_2 , a differential pressure transducer to continuously measure the pressure difference (ΔP) between the upstream and downstream reservoirs, and a second pressure transducer to measure the downstream reservoir pressure, P_2 . This picture is from Core Lab PDP-200 operations manual.

Figure 4-3 demonstrates the shale core samples collected from four different U.S. shale formations, including the Eagle Ford, Marcellus, Mancos, and Barnett formations. The pore pressure, P_p , throughout the core sample is uniform in the initial stage. When $t = 0$, a gas pressure slightly higher than the initial pore pressure is imposed at the upstream end of the core sample. During the process of gas flow into the core sample from the upstream reservoir, the gas pressure in the upstream reservoir declines. When the pressure pulse propagates through the core sample and then reaches the downstream end, the gas pressure in the downstream reservoir increases. After a certain period of time, the differential pressure between the upstream and downstream reservoirs approaches zero. The decay rate of the differential pressure is proportional to the permeability of the core sample. Dicker and Smits (1988) developed the general analytical solution of the differential pressure as a function of time. Chen and Stagg (1984) and Haskett et al. (1988) also made contributions to analytical solutions.

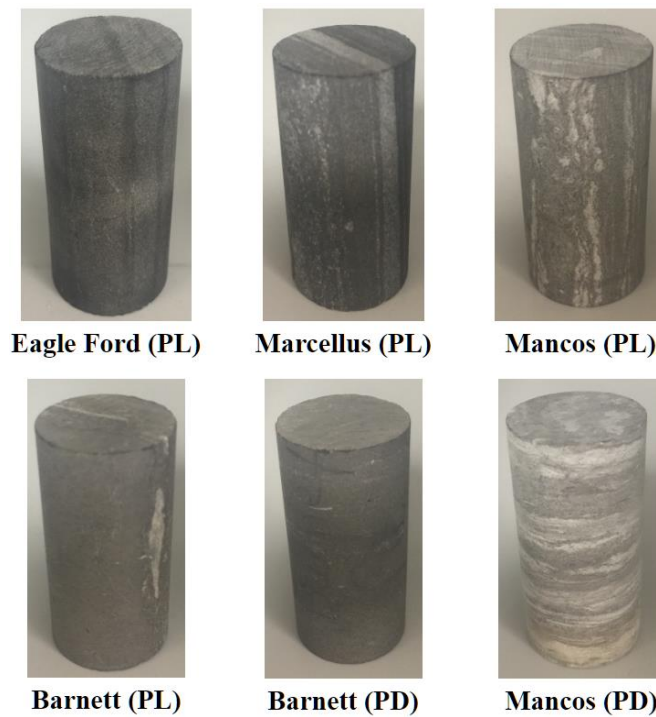


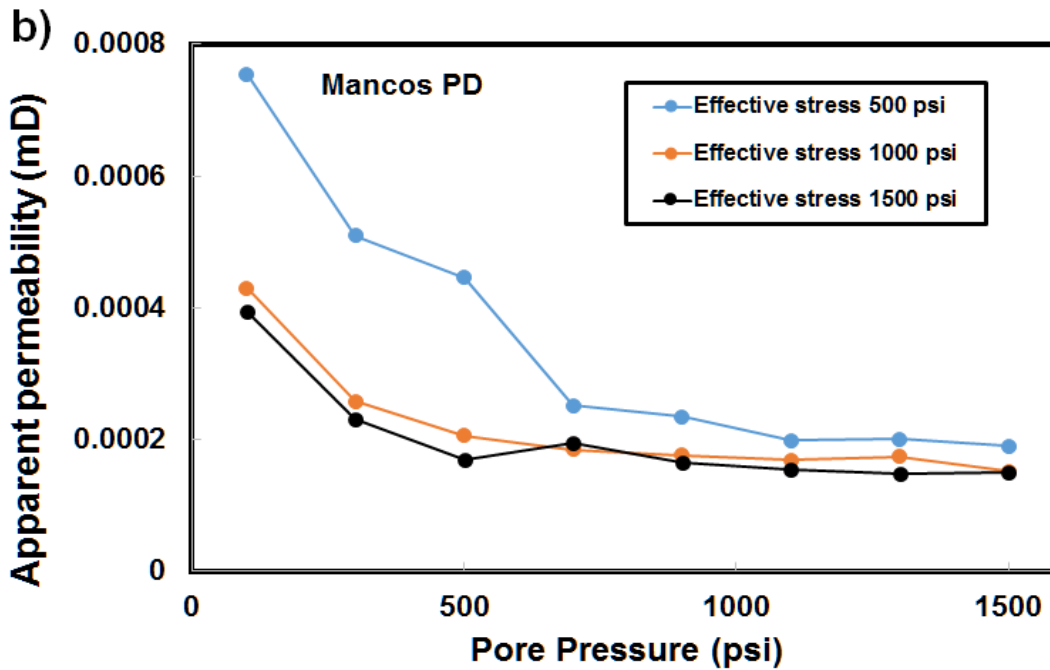
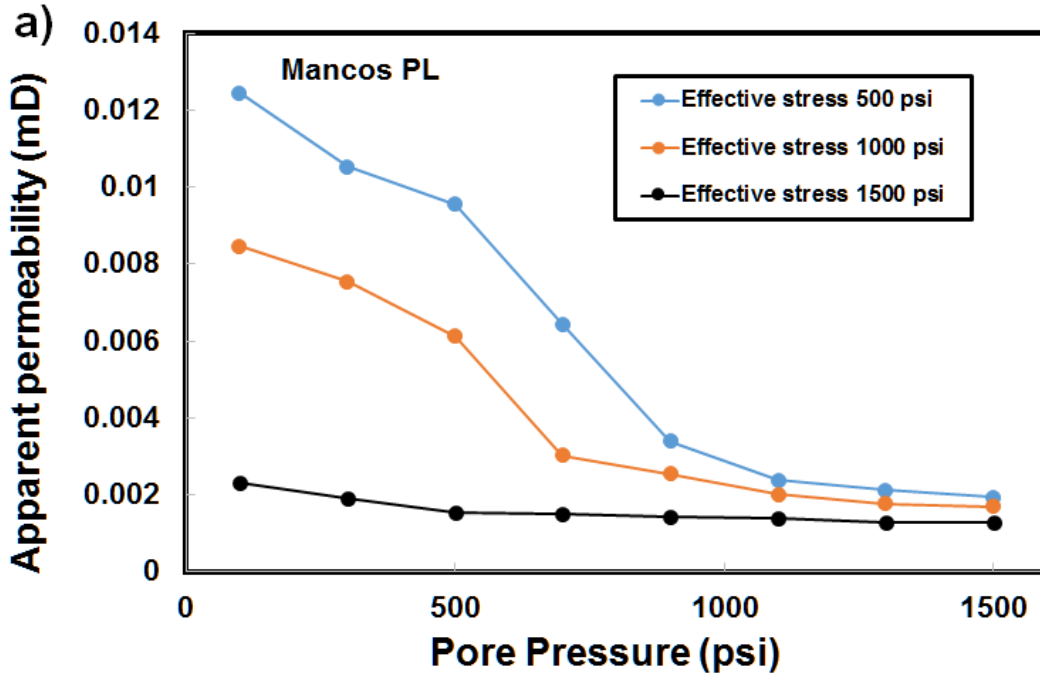
Figure 4-3. Core samples used in the PDP tests. The core samples were extracted from four U.S. shale formations, including the Eagle Ford, Marcellus, Mancos, and Barnett formations. “PL” denotes that the core axis direction is parallel to the bedding plane direction, whereas “PD” indicates that the core axis direction is perpendicular to the bedding plane direction.

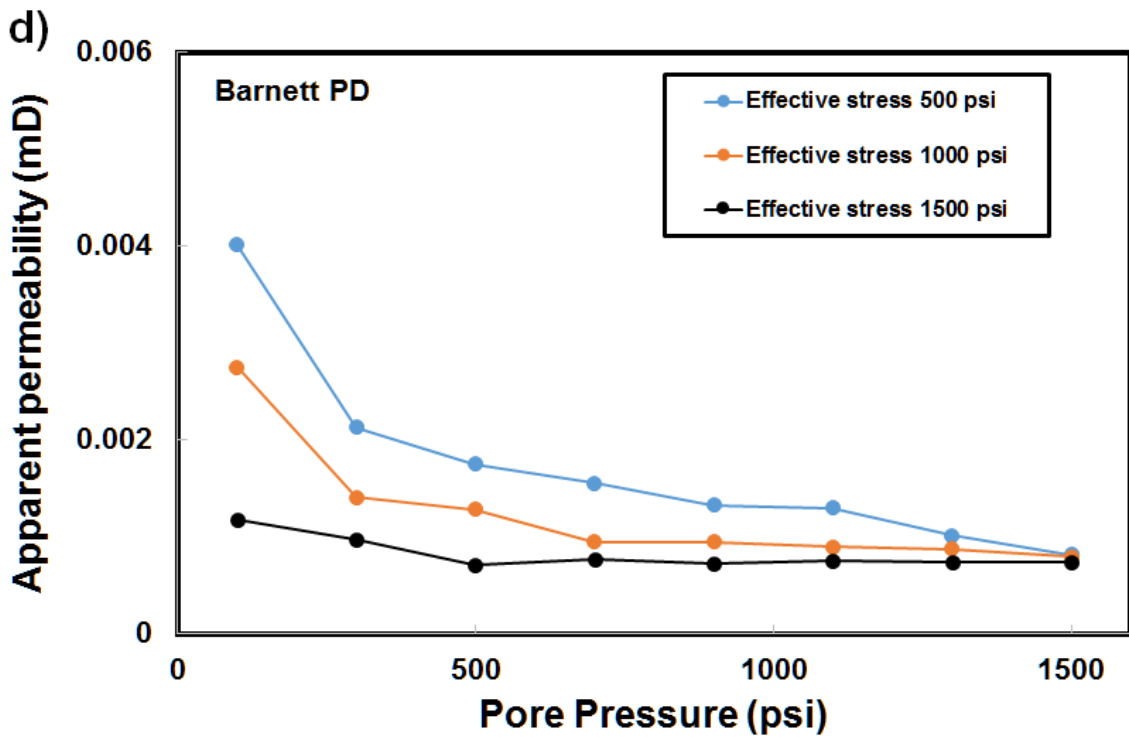
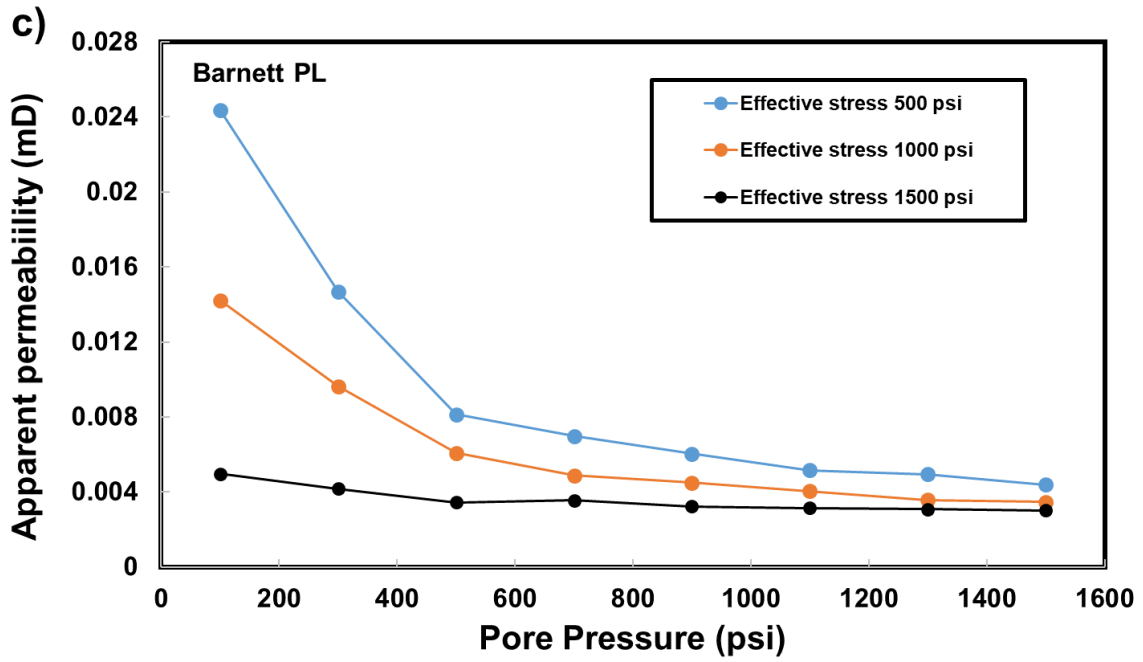
4.4. Results and Discussion

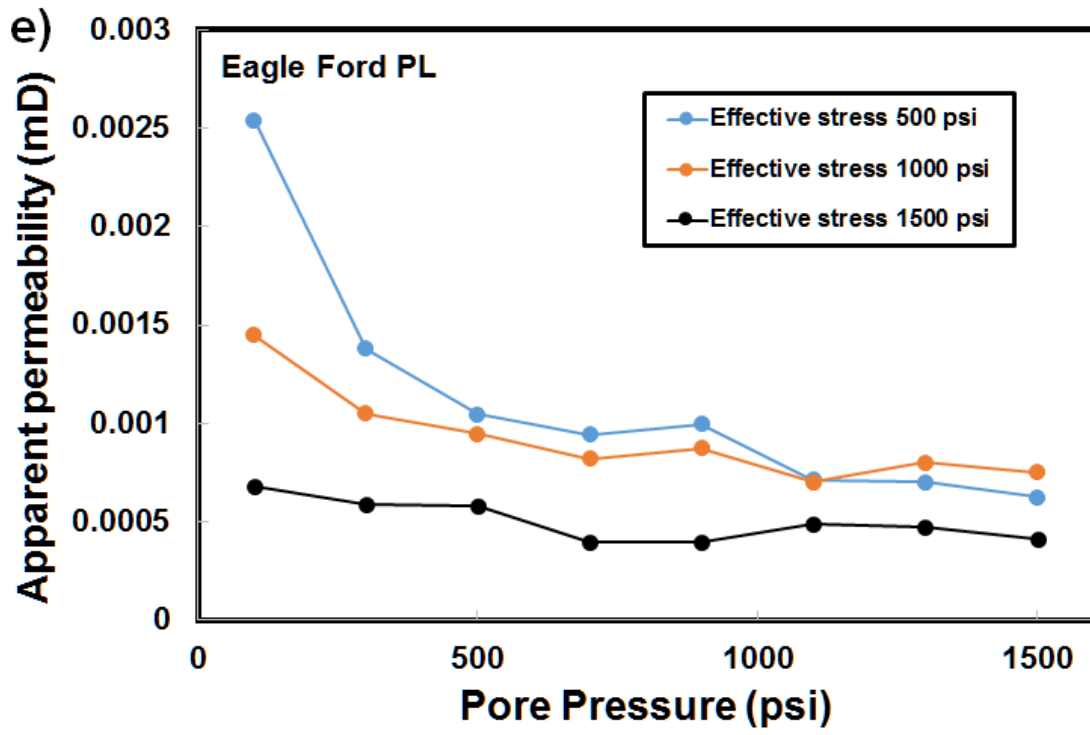
Figure 4-4 illustrates PDP-measured apparent permeability as a function of pore pressure under different effective stresses in the cores of Mancos PL, Mancos PD, Barnett PL, Barnett PD, Eagle Ford PL, and Marcellus PL. All the six groups of PDP tests demonstrated that the apparent permeability decreased with increasing pore pressure when the effective stress was constant based on the simple effective stress law. The sample of Mancos PL had the highest average permeability across all pore pressures, whereas the sample of Mancos PD had the lowest average permeability. Because high pore pressure can mitigate the Klinkenberg effect (Vermylen, 2011), in this study we considered the average value of the apparent permeabilities at the pore pressures of 1300 psi and 1500 psi as the absolute permeability of the core. Specifically, Soeder (1988) used laboratory tests to measure permeability under varying pore pressures for cores extracted from the Marcellus shale. He found that when the pore pressure was higher than 500 psi, permeability change was smaller than 15%. Therefore, the apparent permeabilities measured under 1300 and 1500 psi were very close to the absolute permeability. It was found that the absolute permeabilities of all core samples ranged from 10^{-4} mD to 10^{-2} mD. In addition, it was noticed that in the same shale formation the permeabilities in the cores where the bedding planes were parallel to the core axis were approximately one order of magnitude higher than those in the cores where the bedding planes were perpendicular to the core axis. This is because the pore spaces between bedding planes have higher connectivity and thus provide higher gas flow conductivity, leading to higher permeability if the sample is cored in this direction.

The effective stress is a critical parameter which has a great impact on the PDP-measured apparent permeability. Under high effective stress (1500 psi), the apparent permeability did not change noticeably when the pore pressure increased. This was because that for most core samples there existed connected pore networks having various spatial scales. The relatively small pore networks were more sensitive to effective stress, and they shut off when the effective stress increased, leaving relatively large pore networks open, which were relatively insensitive to the Klinkenberg effect and thus had relatively smaller Klinkenberg coefficients. The relatively high effective stress (1500 psi) effectively reduced the sizes of the connected gas flow channels contained in the organic-rich materials, leading to enhanced Klinkenberg coefficient, b , and consequently higher apparent permeabilities. When the effective stress was 500 psi, the apparent permeabilities decreased noticeably with increasing pore pressure, which suggests that the

Klinkenberg effect was significant under the relatively low effective stress because all relatively small pore networks stayed open.







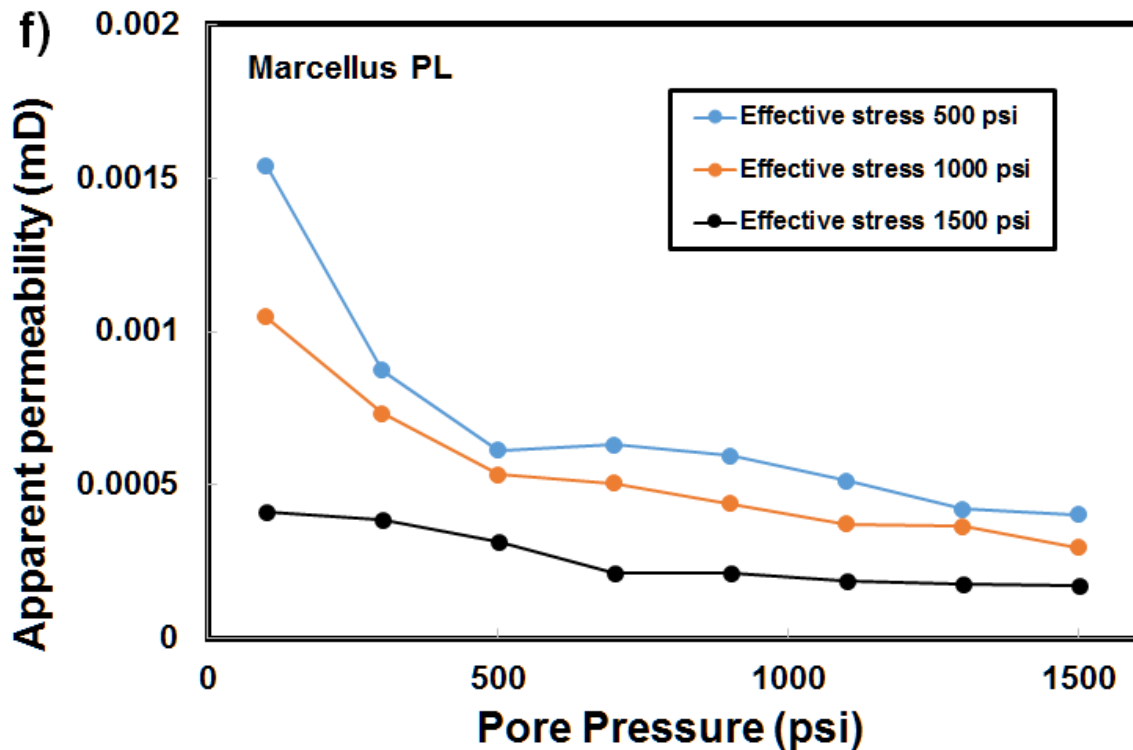
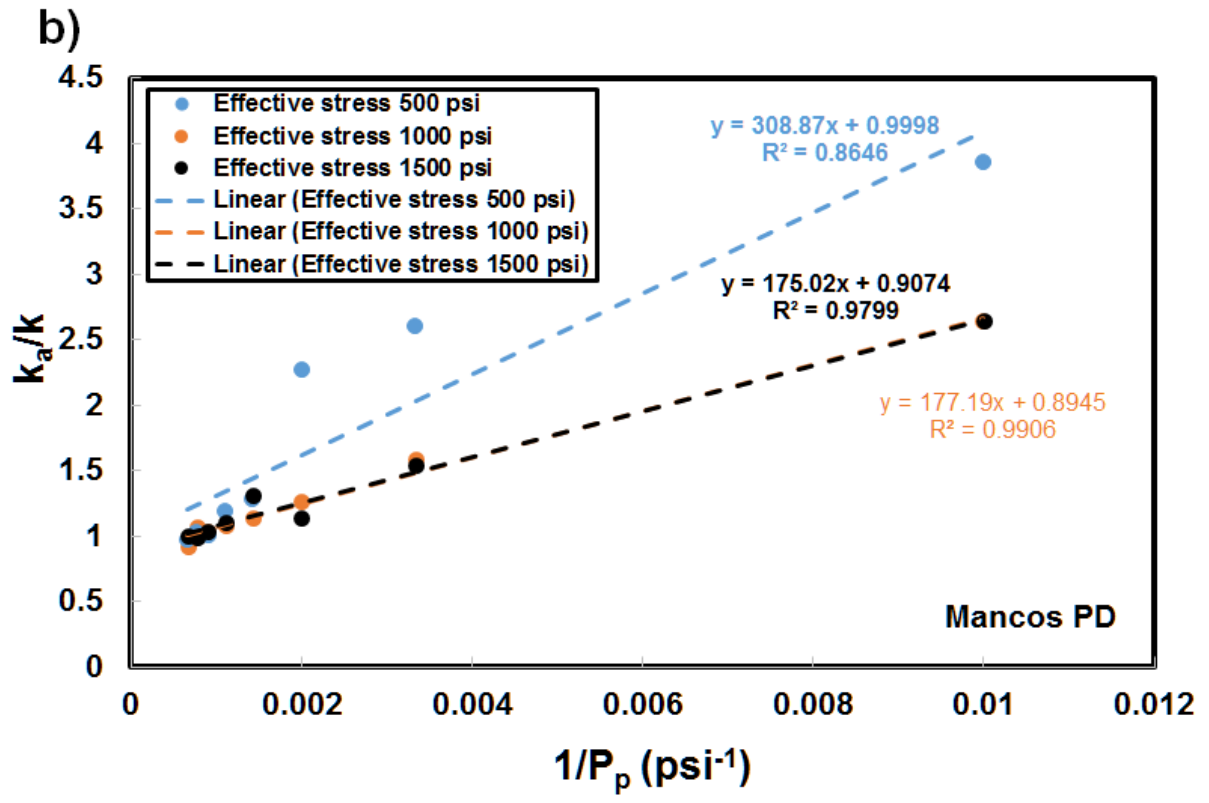
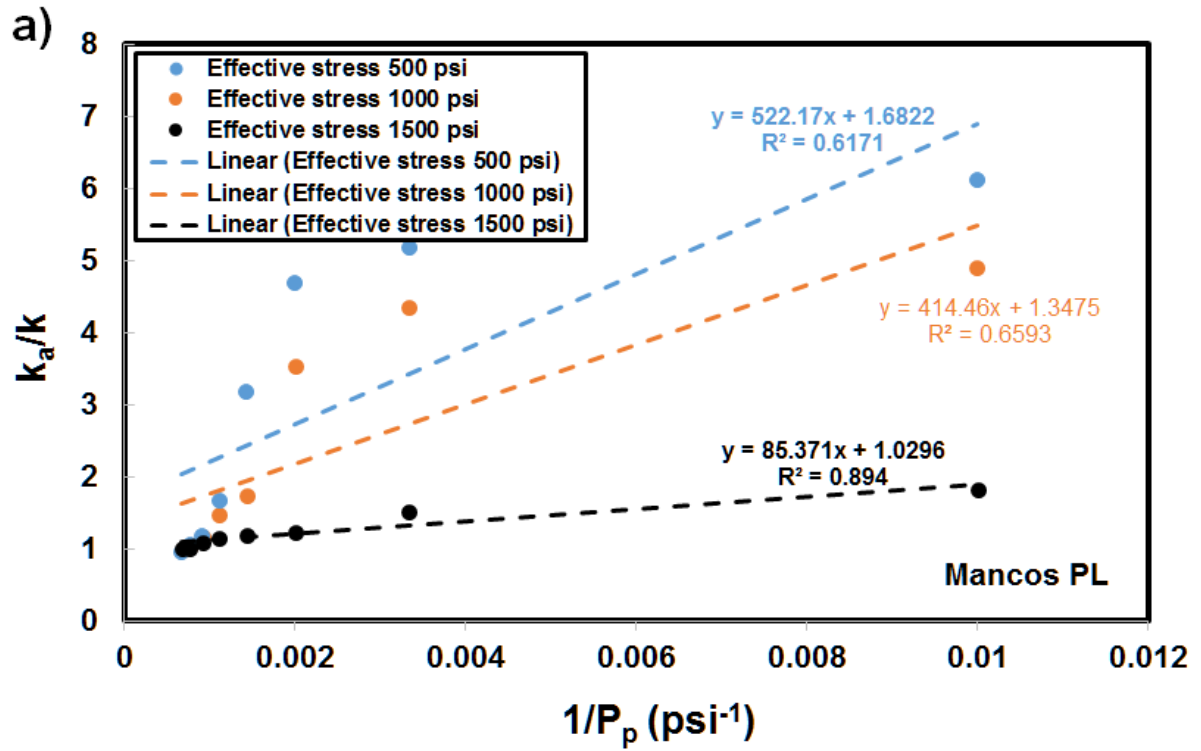
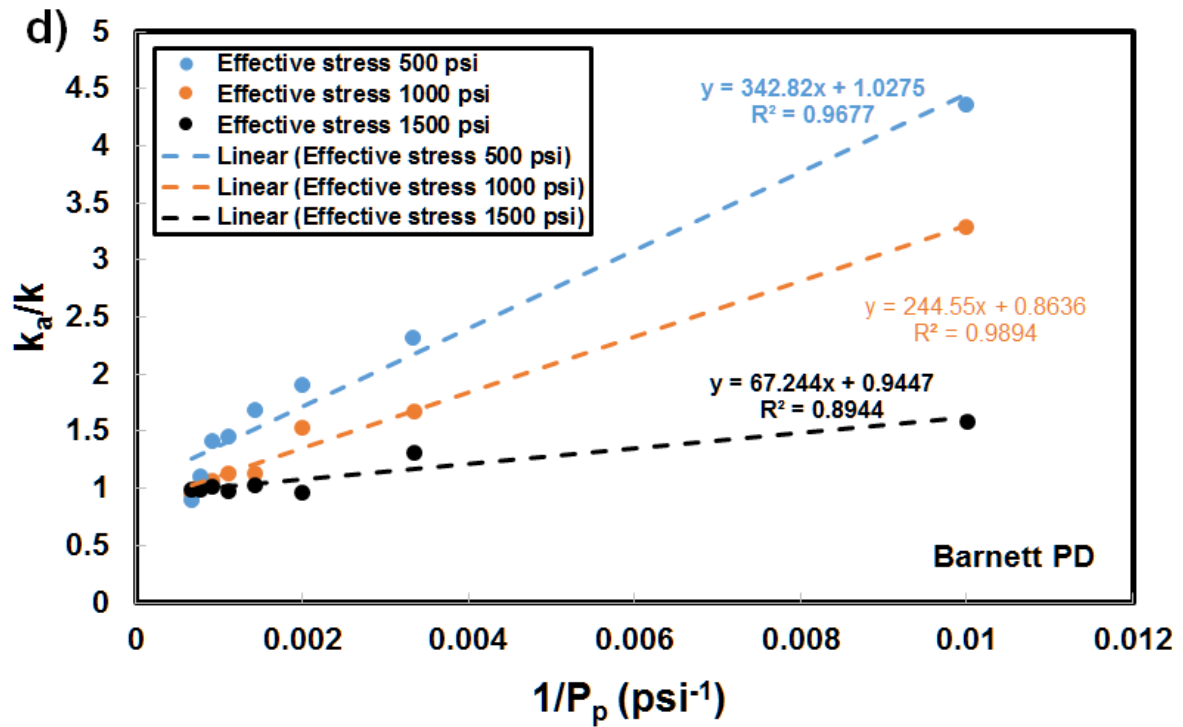
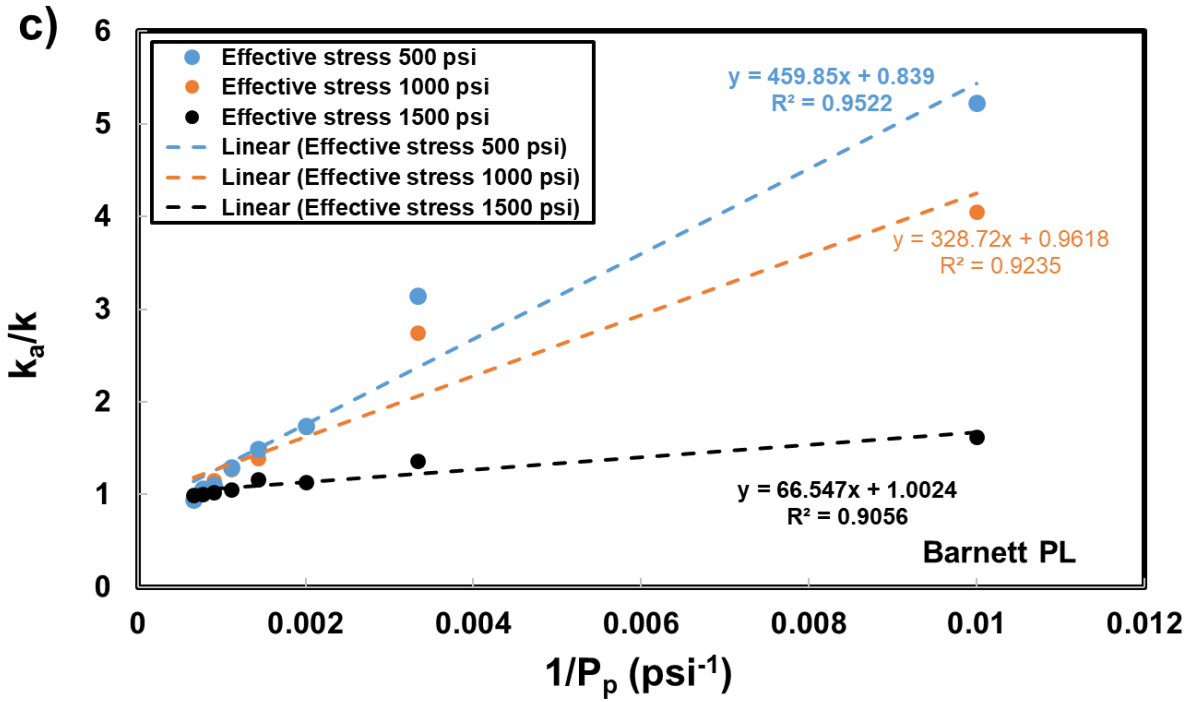


Figure 4-4. Apparent permeability as a function of pore pressure under different effective stresses in the core of a) Mancos PL, b) Mancos PD, c) Barnett PL, d) Barnett PD, e) Eagle Ford PL, and f) Marcellus PL.

Figure 4-5 illustrates k_a/k as a function of $1/P_p$, as well as the linear equation fitting, in the core samples of Mancos PL, Mancos PD, Barnett PL, Barnett PD, Eagle Ford PL, and Marcellus PL. Based on Equation 4-1, the y-intercept of the linear equation is 1, and the slope is equal to the Klinkenberg coefficient, b , in the unit of psi. The variation of the value of b , as a function of the effective stress across the six shale core samples, was consistent with the description and explanation in Figure 4-4. It was also noticed that the values of b , most of which fell into the range between 100 psi and 400 psi, were close to what were found in the literature based on laboratory (Soeder, 1988) and analytical (Chen, 2016) methods.





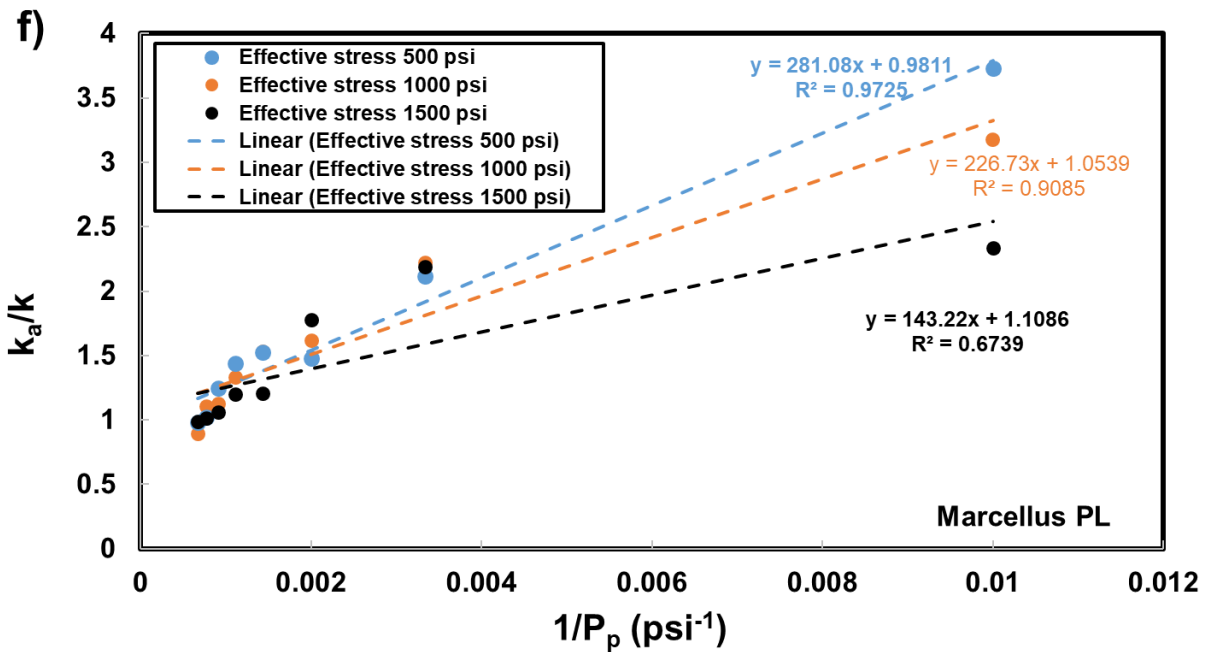
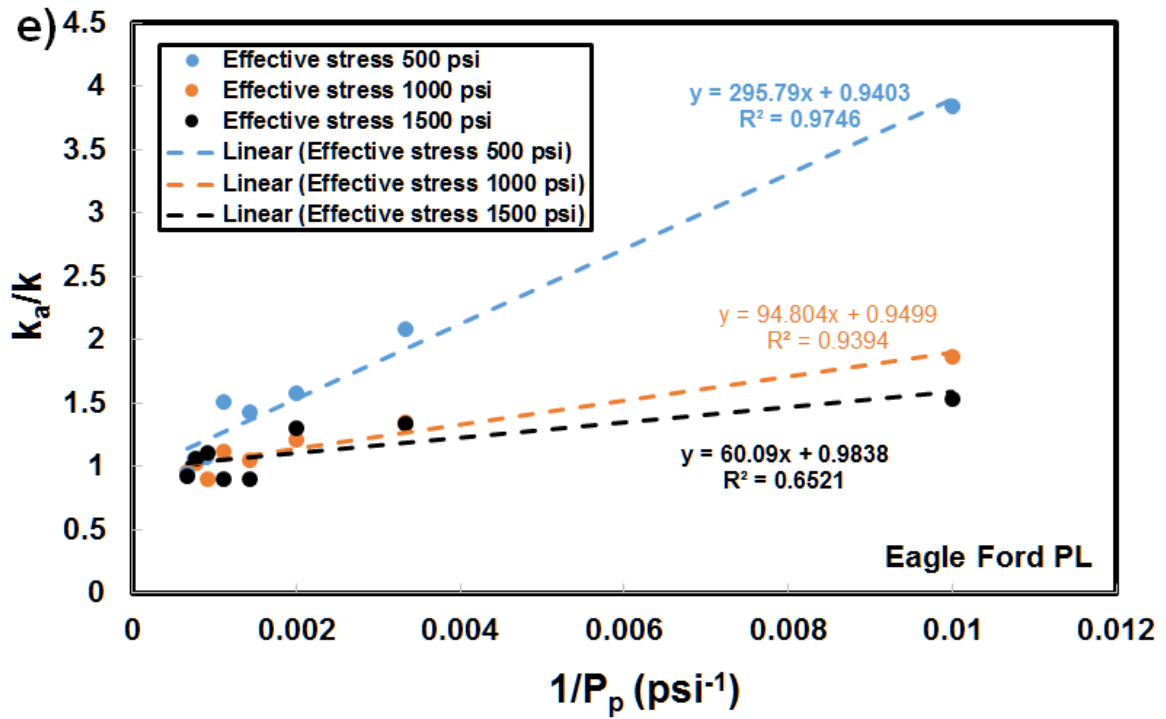
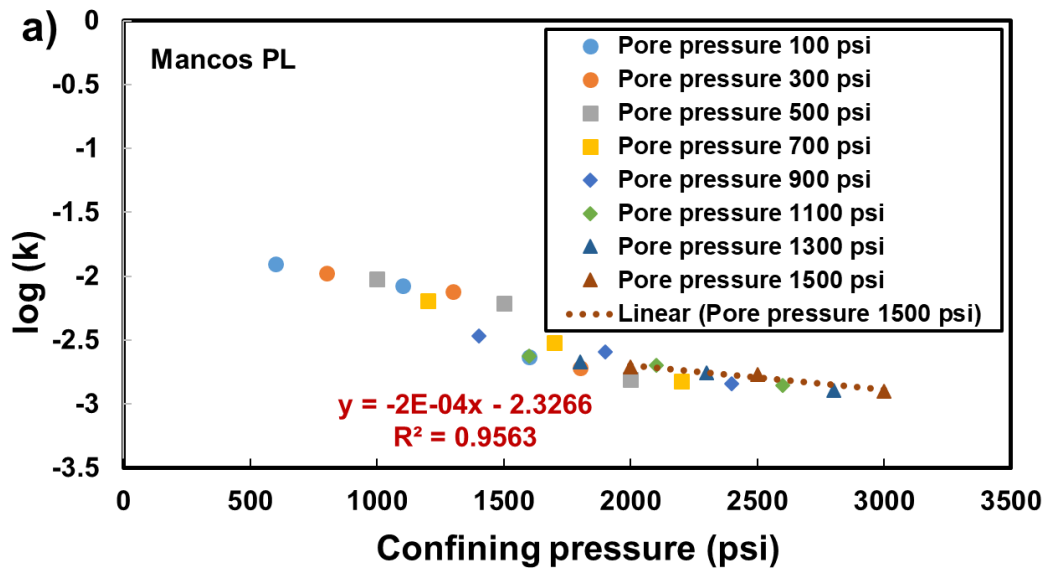
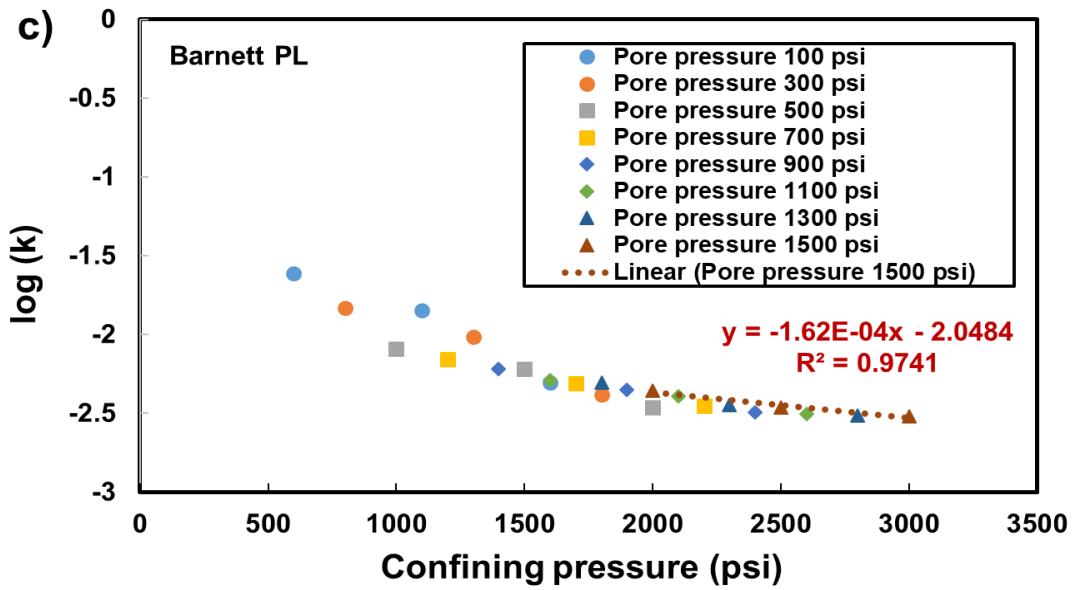
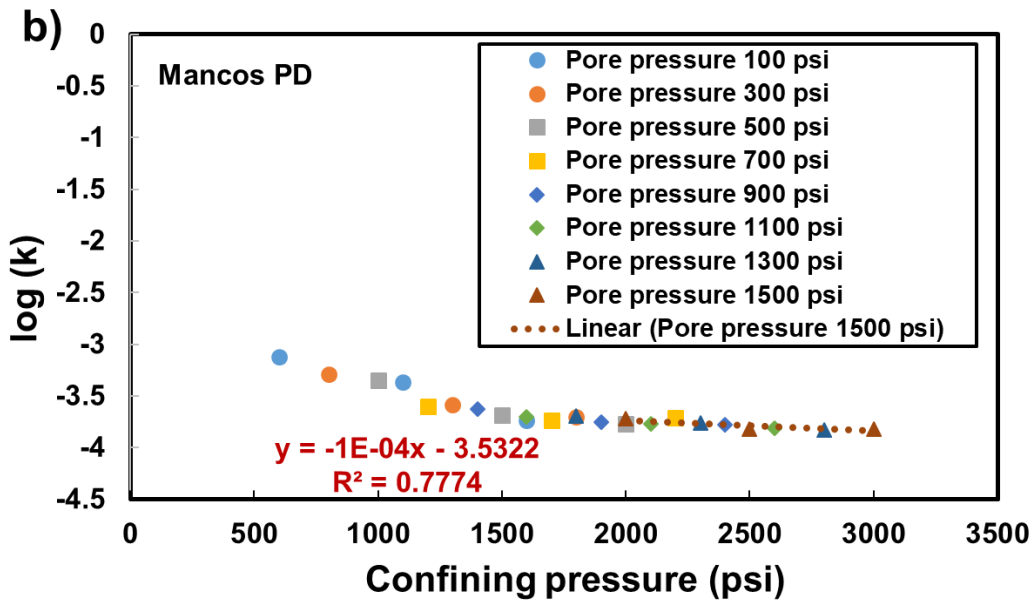


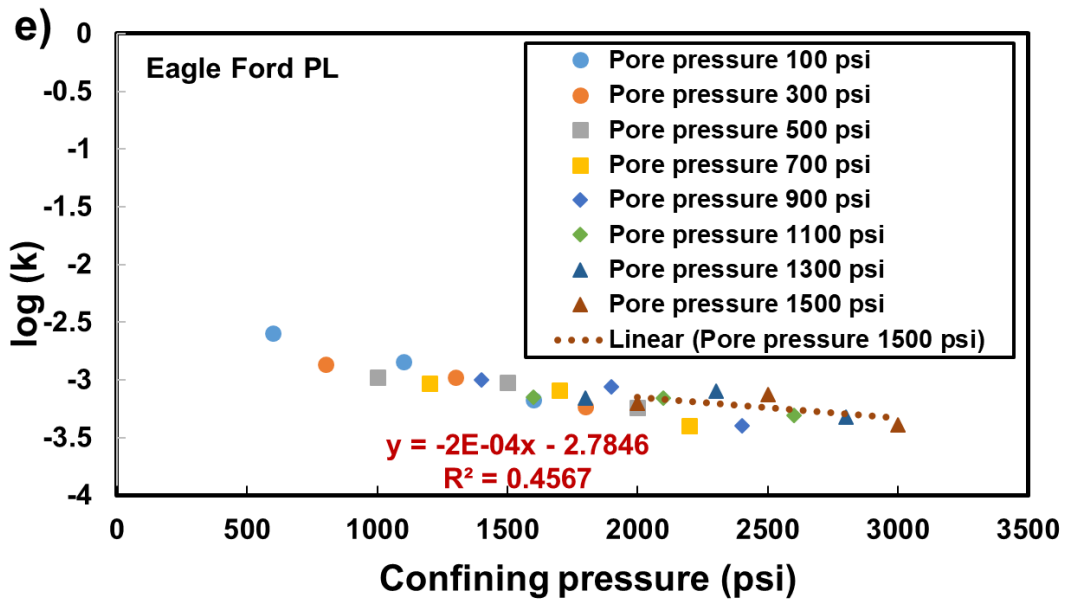
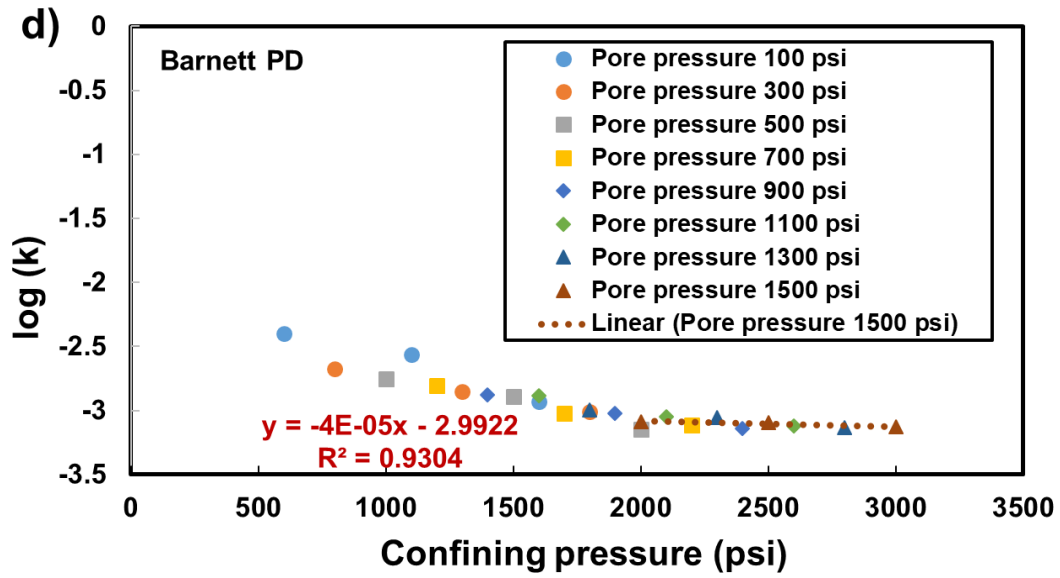
Figure 4-5. k_a/k as a function of $1/P_p$, as well as the linear equation fitting, in the core samples of a) Mancos PL, b) Mancos PD, c) Barnett PL, d) Barnett PD, e) Eagle Ford PL, and f) Marcellus

PL. Based on Equation 4-1, the y-intercept of the linear equation is 1 and the slope is equal to the Klinkenberg coefficient, b .

We then used the data fitting method, which was originally developed by Bernabe (1986) and then improved by Kwon et al. (2001), to find the effective stress coefficient (i.e., the Biot coefficient), χ , in the effective coefficient law (i.e., Equation 4-4). **Figure 4-6** illustrates $\log(k)$ as a function of the confining pressure, P_c , under varying pore pressures. The slope of the fitted straight lines was equal to $\partial \log(k) / \partial P_c$. Based on the method of Kwon et al. (2001), the value of $\partial \log(k) / \partial P_c$ in the same core sample should be constant and independent of the selected pore pressure, which is confirmed in Figure 4-6. Thus, in this study we used the data measured under the pore pressure of 1500 psi to fit $\partial \log(k) / \partial P_c$. It should be noted that in the same core sample the slopes of the straight lines fitted under the other pore pressures were close to that for the pore pressure of 1500 psi. Figure 4-6 demonstrates that the value of $\partial \log(k) / \partial P_c$ ranges from 4×10^{-5} to 4×10^{-4} .







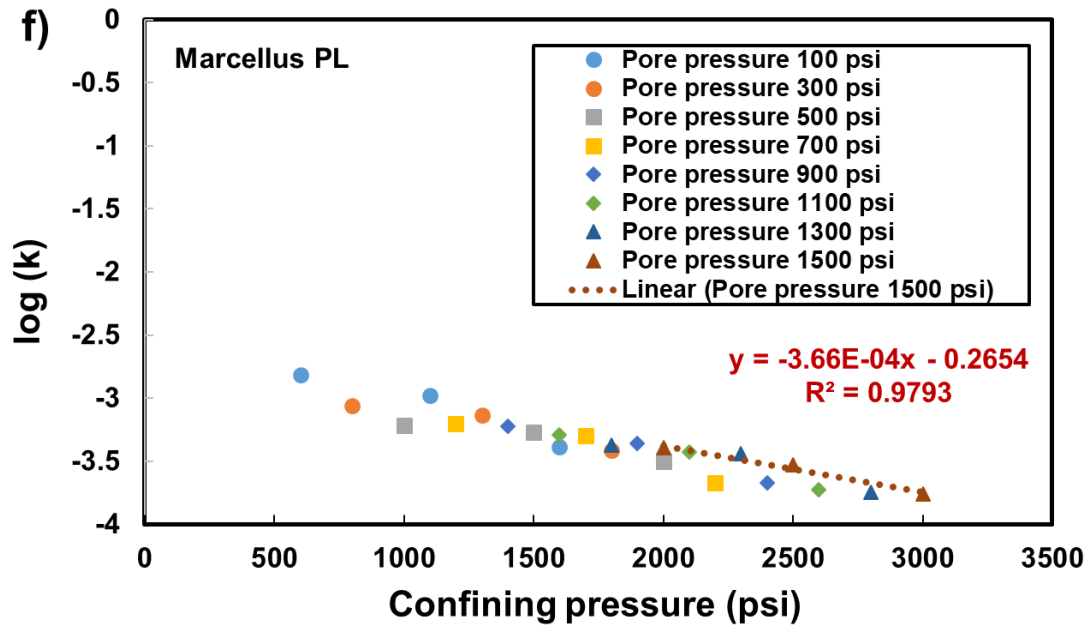
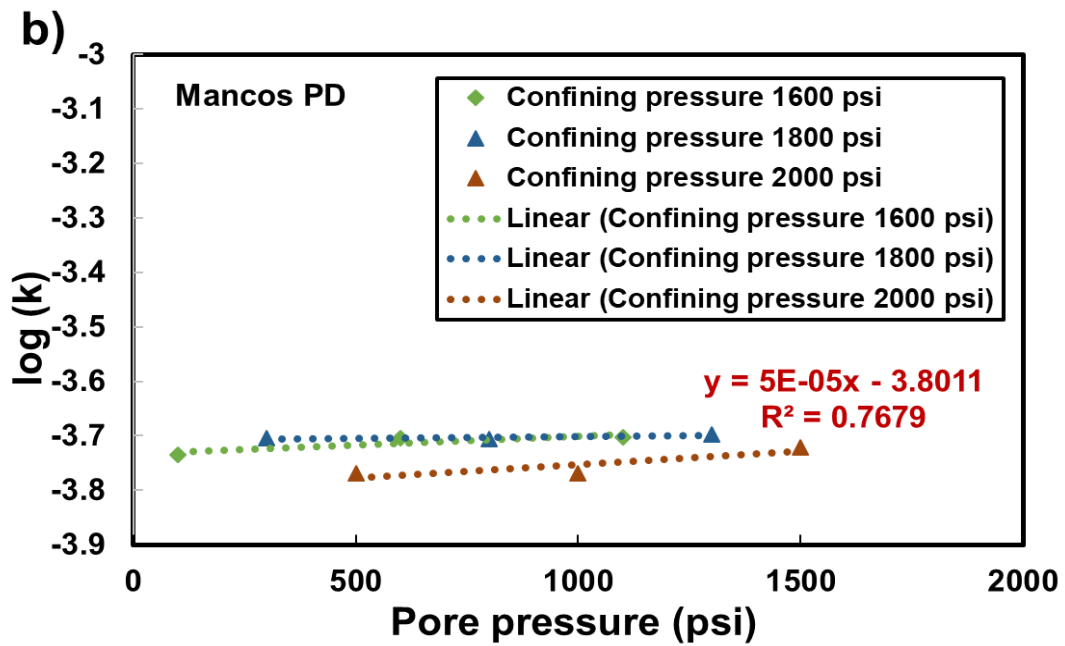
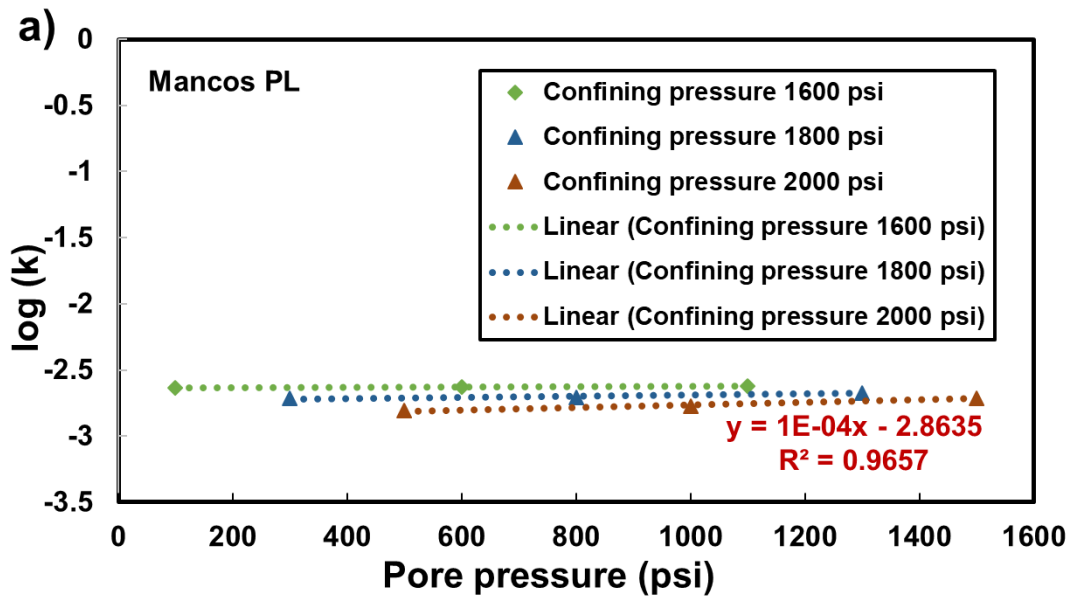
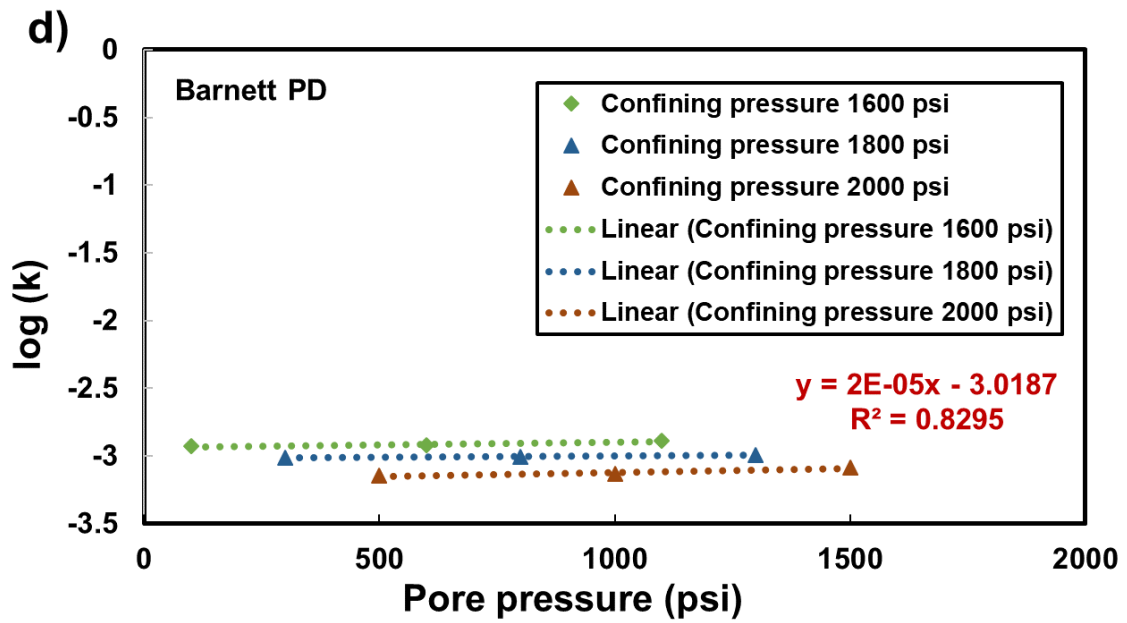
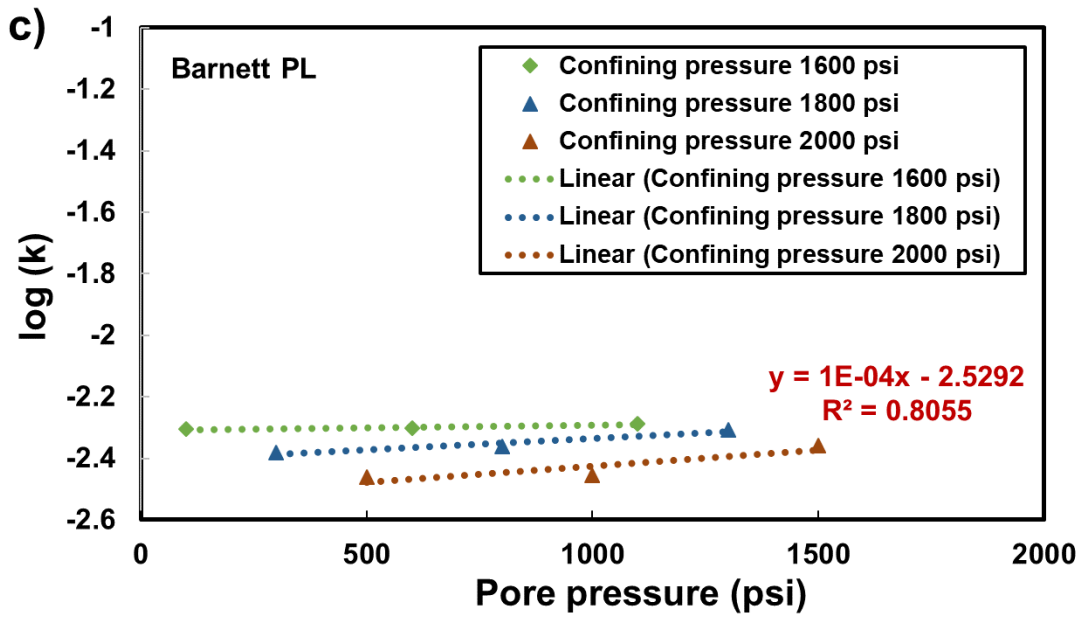


Figure 4-6. The value of $\log(k)$ as a function of the confining pressure, P_c , under varying pore pressures in the formations of a) Mancos PL, b) Mancos PD, c) Barnett PL, d) Barnett PD, e) Eagle Ford PL, and f) Marcellus PL.

Figure 4-7 illustrates $\log(k)$ as a function of the pore pressure, P_p , under varying confining pressures. The slope of the fitted straight lines was equal to $\partial \log(k) / \partial P_p$. Based on the method of Kwon et al. (2001), the value of $\partial \log(k) / \partial P_p$ in the same core sample should be constant and independent of the selected confining pressure, which is confirmed in Figure 4-7. Thus, in this study we used the data measured under the confining pressure of 2000 psi to fit $\partial \log(k) / \partial P_p$. It should be noted that in the same core sample the slopes of the straight lines fitted under the other confining pressures were close to that for the confining pressure of 2000 psi. Figure 4-7 demonstrates that the value of $\partial \log(k) / \partial P_p$ ranges from 2×10^{-5} to 1×10^{-4} .





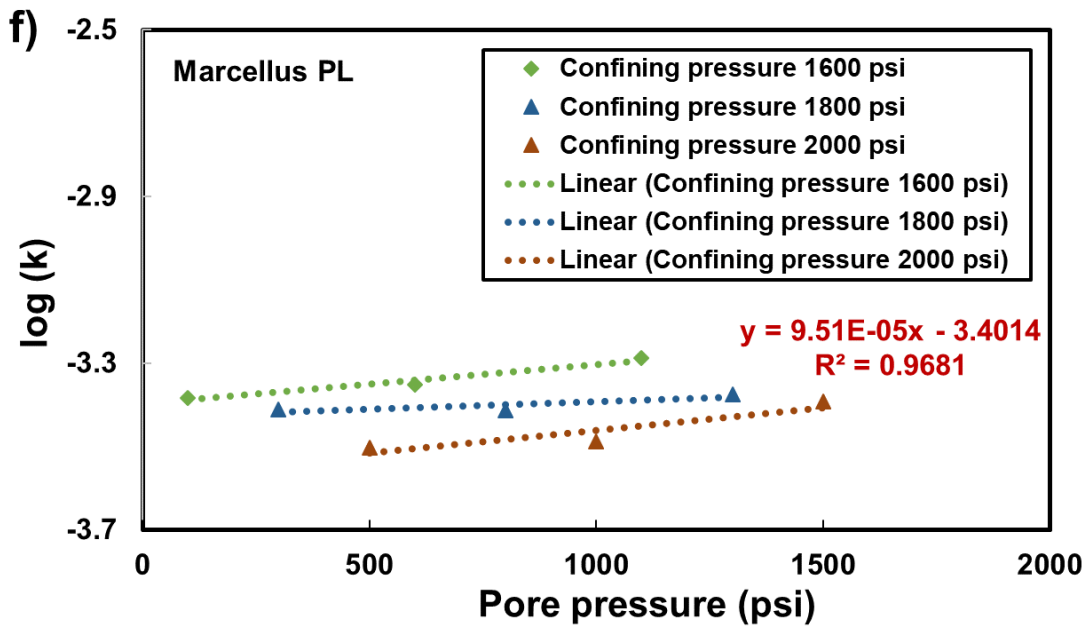
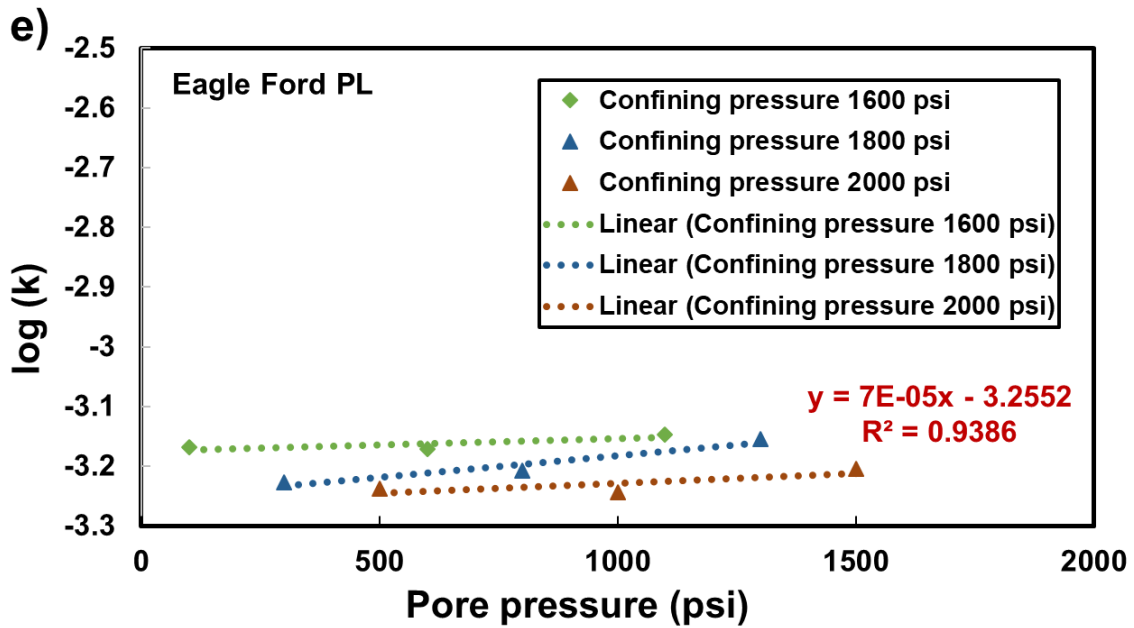
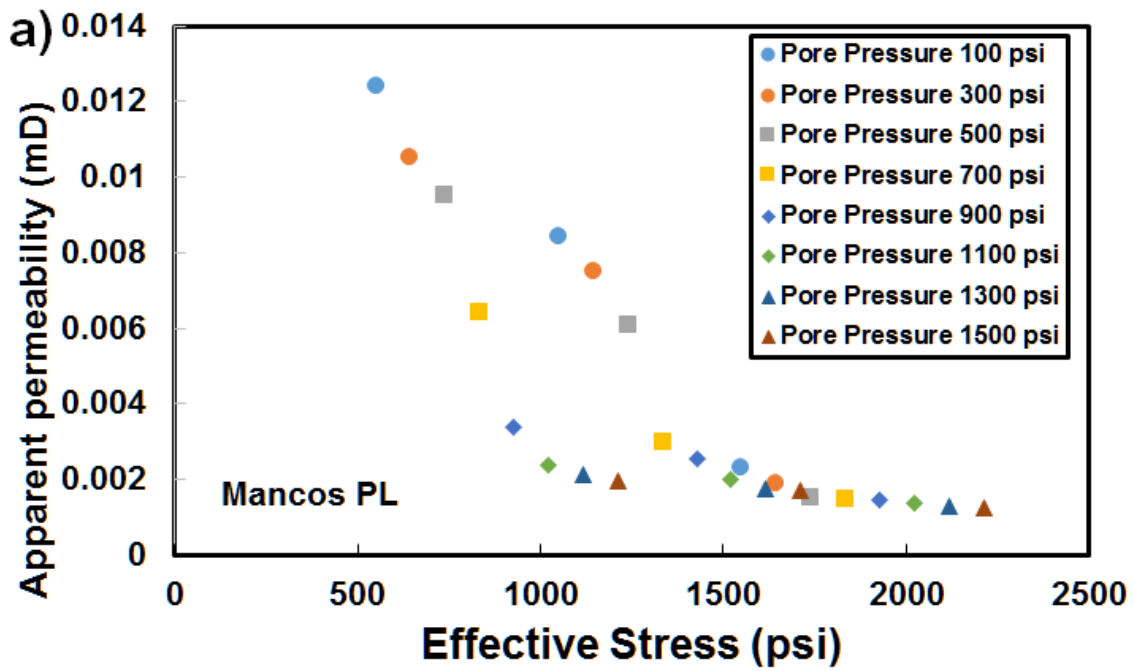
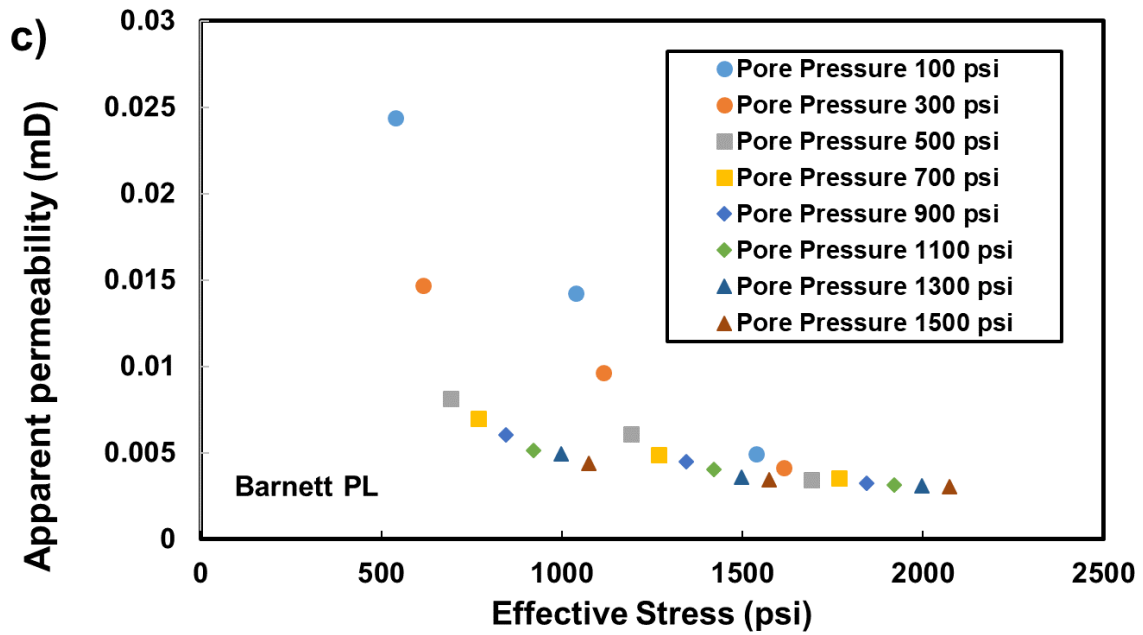
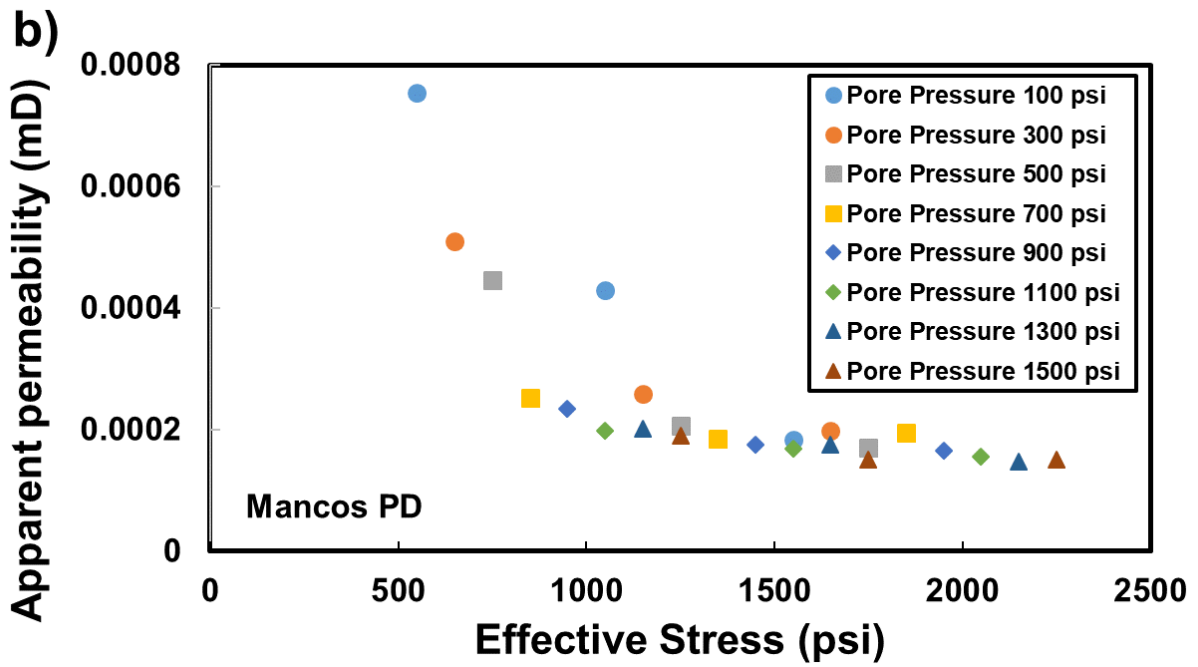


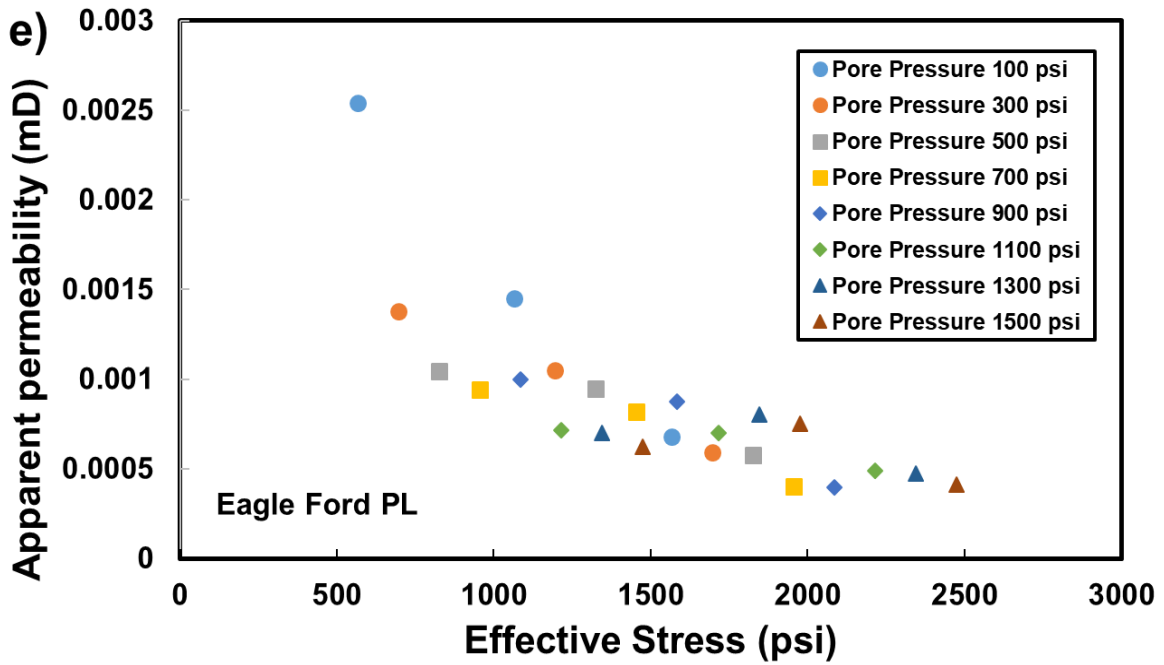
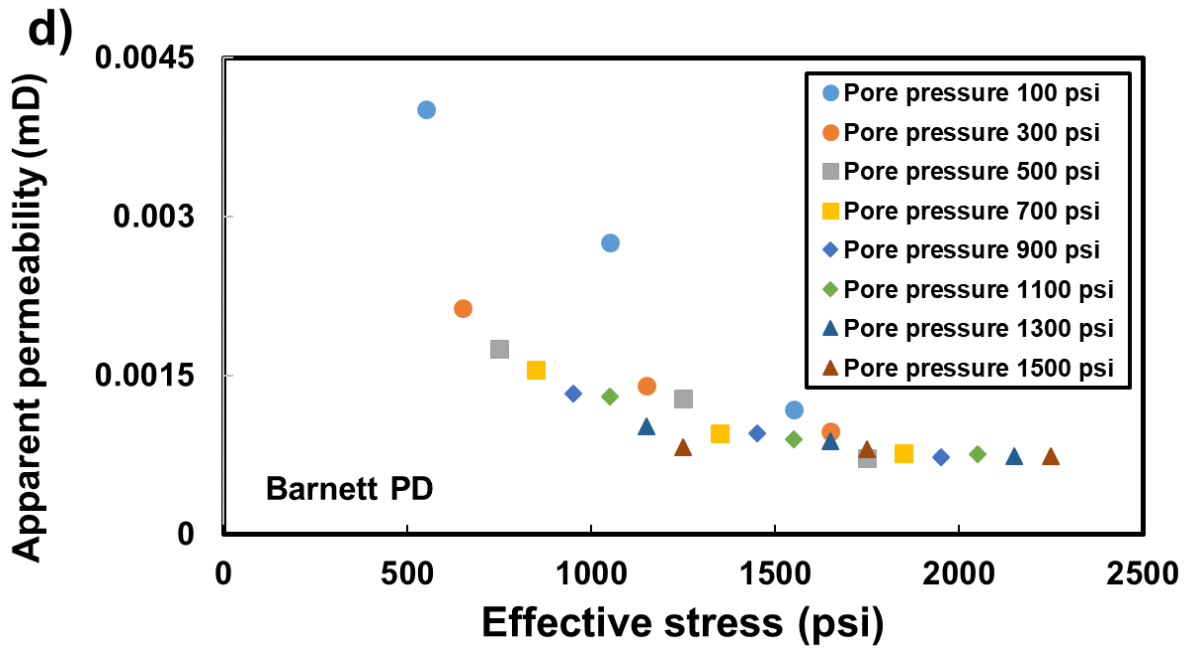
Figure 4-7. The value of $\log(k)$ as a function of pore pressure in the formations of a) Mancos PL, b) Mancos PD, c) Barnett PL, d) Barnett PD, e) Eagle Ford PL, and f) Marcellus PL.

Based on the results from Figures 4-6 and 4-7, we calculated the values of χ in the six shale formations using Equation 4-11. Specifically, the values of χ in the four core samples were 0.50,

0.50, 0.62, 0.50, 0.35 and 0.26, respectively. **Figure 4-8** illustrates PDP-measured apparent permeability as a function of the effective stress calculated based on χ in the six formations. The result demonstrates that in general the PDP-measured apparent permeability decreases with the increase of the effective stress calculated based on χ .







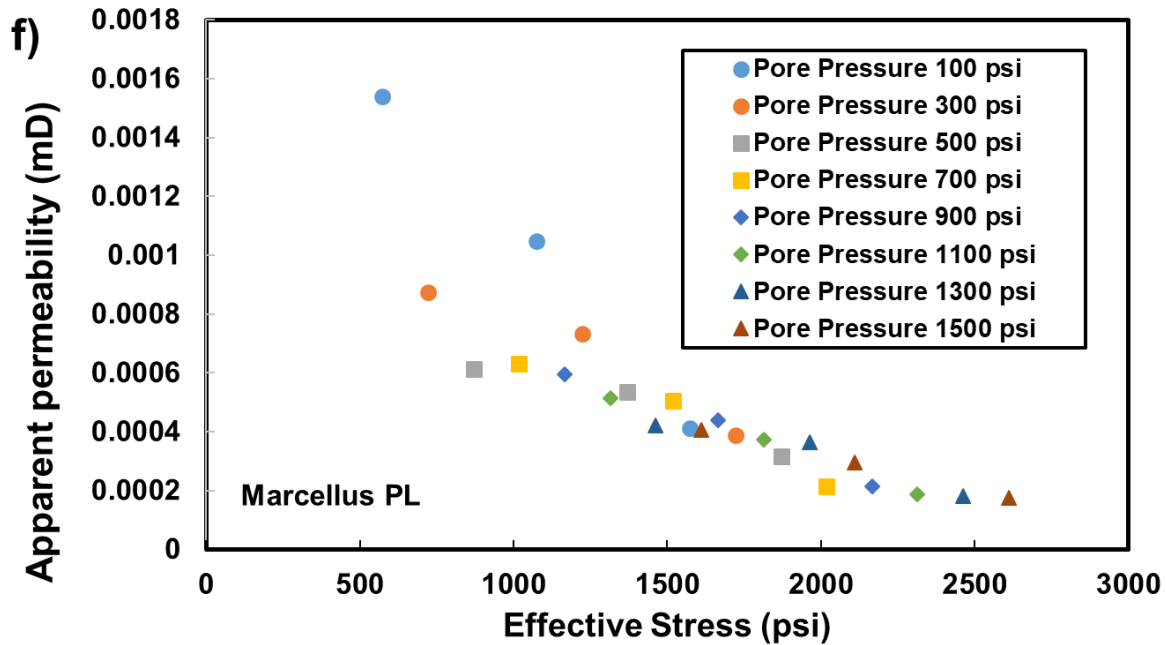


Figure 4-8. PDP-measured apparent permeability as a function of the effective stress calculated based on χ in a) Mancos PL, b) Mancos PD, c) Barnett PL, d) Barnett PD, e) Eagle Ford PL, and f) Marcellus PL.

4.5. Conclusions

In this study, comprehensive core analyses based on the PDP method were conducted to investigate the relationships between apparent permeability, pore pressure, and confining pressure. The influence of the Klinkenberg effect, as well as the direction of bedding planes, on the PDP-measured apparent permeability was also studied. Based on large volumes of data analytics, the effective stress coefficient (i.e., the Biot coefficient) was determined. The laboratory results indicate that in the same shale formation the permeabilities of the cores where the bedding planes were parallel to the core axis were approximately one order of magnitude higher than those in the cores where the bedding planes were perpendicular to the core axis.

Under high effective stress, the apparent permeability did not change noticeably when the pore pressure increased. This was because that for most core samples there existed connected pore networks having heterogeneous spatial scales. The relatively small pore networks were more sensitive to effective stress and they shut off when the effective stress increased, leaving relatively

large pore networks open, which were relatively insensitive to the Klinkenberg effect and thus had relatively small Klinkenberg coefficients. The relatively high effective stress effectively reduced the sizes of the connected gas flow channels contained in the organic-rich materials, leading to enhanced Klinkenberg coefficient and consequently higher apparent permeabilities.

This study advances the fundamental understanding of the role of confining pressure, pore pressure, and bedding plane direction on the apparent permeability of shales. The research outcome has the potential to benefit the optimization of engineering design in hydraulic fracturing. The laboratory experiments provide insight into the Klinkenberg effect and its role on the apparent permeability under varying confining pressures in different U.S. formations.

Chapter 5. Conclusions and Recommendations

The long-term waterflooding treatment had a noticeable influence on the petrophysical properties of a petroleum reservoir. The variations in permeability and porosity depended on the development stages through the waterflooding development history. The CT-scanned waterflooding experiments illustrated the distribution of water and oil saturations through the four different stages and showed that the polymer flooding led to a higher sweep efficiency because of the mitigation of viscous fingering. The velocity sensitivity decreased whereas the salinity sensitivity increased after the long-term waterflooding treatment. The mercury intrusion data not only provided more details of the pore structure but also contributed to the MLR model development. The MLR model output agreed well with the petrophysical property variations measured in the laboratory. The variations of the predictor coefficients in the MLR model indicated the changes in the reservoir petrophysical characteristics through the four development stages. The findings from this study advance the fundamental understanding of the role of long-term waterflooding treatment on oilfield developments. This work also provides valuable insight into the combination of reservoir petrophysical properties and MLR modeling. The outcome of this research will benefit geological reservoir simulations by providing insightful correlations between various reservoir petrophysical properties.

In this thesis, various laboratory experimental techniques were utilized to study the pore-scale effects of long-term waterflooding treatments on the changes of reservoir petrophysical properties. 2D microfluidic flow models were developed, in which the pore geometries were based on CTS imaging data. With the development of long-term waterflooding treatments, fine particles in the reservoir rock were dislodged, leading to coarser grain sorting. In addition, the cementing materials in the pore spaces between particles were also removed due to waterflooding. These pore-scale processes resulted in the increase of pore space size and consequently increasing rock porosity and developments of preferential flow paths. Rock surface corrosion and dissolution due to the long-term waterflooding treatments were proved by using high-resolution SEM imaging. Laboratory relative permeability measurements, based on the unsteady-state method, demonstrated that the long-term waterflooding treatments caused the increase of oil relative permeability. This implies that the waterflooding processes reduced the contact angle at rock surfaces and thus led to a more water-wet formation. Microfluidic core flooding experiments illustrated the development of

viscous fingering (i.e., preferential flow channels of the injected fluid) when the injection water flow rate was higher than a certain level, which resulted in reduced overall sweep efficiency. The findings from this study advance the fundamental understanding of the role of long-term waterflooding treatment on the changes of reservoir petrophysical properties at the pore scale. Specifically, pore-scale variations of pore structure geometry, mineral composition, relative permeability and contact angle, and sweep efficiency, which was due to long-term waterflooding development, were identified and investigated. This work also provides valuable insights into the role of injection flow rate on the displacement efficiency in the later stage of waterflooding developments.

Finally, comprehensive core analyses based on the PDP method were conducted to investigate the relationships between apparent permeability, pore pressure, and confining pressure. The influence of the Klinkenberg effect as well as the direction of bedding planes on the PDP-measured apparent permeability was also studied. Based on large volumes of data analytics, the effective stress coefficient (i.e., the Biot coefficient) was determined. The laboratory results indicated that in the same shale formation the permeabilities of the cores where the bedding planes were parallel to the core axis were approximately one order of magnitude higher than those in the cores where the bedding planes were perpendicular to the core axis. Under high effective stress, the apparent permeability did not change noticeably when the pore pressure increased. This was because that for most core samples there existed connected pore networks having heterogeneous spatial scales. The relatively small pore networks were more sensitive to effective stress, and they shut off when the effective stress increased, leaving relatively large pore networks open, which were relatively insensitive to the Klinkenberg effect and thus had relatively small Klinkenberg coefficients. The relatively high effective stress effectively reduced the sizes of the connected gas flow channels contained in the organic-rich materials, leading to enhanced Klinkenberg coefficient and consequently higher apparent permeabilities. This study advances the fundamental understanding of the role of confining pressure, pore pressure, and apparent permeability and will benefit the optimization of engineering design in hydraulic fracturing. The laboratory experiments provide insight into the Klinkenberg effect and its role on the apparent permeability under varying confining pressures in different U.S. formations.

Future work will be focused on the investigation of more types of petrophysical properties and the study of the relationship between them based on different geological backgrounds. The MLR-

based statistical model will be extended to the nonlinear mixing model and Bayesian model. More core analysis experiments will be conducted to increase the data volume. Furthermore, a theoretical model will be developed to fit and interpret the PDP laboratory data. This model will account for the coupled processes that involve fluid mechanics, geomechanics, and the Klinkenberg effect to advance the fundamental understanding with respect to shale gas recovery in deep reservoirs.

REFERENCE

Alpak, Faruk O., et al. "Simplified modeling of turbidite channel reservoirs." *SPE Journal* 15.02 (2010): 480-494.

Ameen, Siyamak, and Arash Dahi Taleghani. "Dynamic modeling of channel formation during fluid injection into unconsolidated formations." *SPE Journal* 20.04 (2015): 689-700.

Andersen, Charlotte Møller, and Rasmus Bro. "Variable selection in regression—a tutorial." *Journal of Chemometrics* 24.11-12 (2010): 728-737.

Anderson, William G. "Wettability literature survey-part 6: the effects of wettability on waterflooding." *Journal of petroleum technology* 39.12 (1987): 1-605.

Bager, Ali, et al. "Addressing multicollinearity in regression models: a ridge regression application." (2017).

Bernabe, Y. 1986. The effective pressure law for permeability in Chelmsford granite and Barre granite. In *International Journal of Rock Mechanics and Mining Sciences & Geomechanics Abstracts* (Vol. 23, No. 3, pp. 267-275). Pergamon.

Beskok, A., and Karniadakis, G. E. A model for flows in channels, pipes, and ducts at micro and nano scales. *Microscale Thermophysical Engineering* 3:43-77, 1999.

Blanchard, V., Lasseux, D., Bertin, H. J., Pichery, T. R., Chauveteau, G. A., Tabary, R., & Zaitoun, A. 2007. Gas/water flow in porous media in the presence of adsorbed polymer: Experimental study on non-darcy effects. *SPE Reservoir Evaluation & Engineering*, 10(04), 423-431.

Bourbie, T., & Walls, J. 1982. Pulse decay permeability: analytical solution and experimental test. *Society of Petroleum Engineers Journal*, 22(05), 719-721.

Chatterjee, Samprit, and Ali S. Hadi. *Regression analysis by example*. John Wiley & Sons, 2015.

Chen, C. 2016. Multiscale imaging, modeling, and principal component analysis of gas transport in shale reservoirs. *Fuel*, 182, 761-770.

Chen, C., D. Hu, D. Westacott, and D. Loveless (2013), Nanometer-scale characterization of microscopic pores in shale kerogen by image analysis and pore-scale modeling, *Geochemistry, Geophysics, Geosystems*, 14(10), 4066-4075, DOI: 10.1002/ggge.20254.

Chen, C., and L. Zeng (2015), Using the level set method to study the effects of heterogeneity and anisotropy on hyporheic exchange, *Water Resour. Res.*, 51, 3617–3634, doi:10.1002/2014WR016444.

Chen, C., Martysevich, V., O’Connell, P. et al. 2015. Temporal Evolution of the Geometrical and Transport Properties of a Fracture/Proppant System under Increasing Effective Stress. *SPE J.* 20 (3): 527–535. SPE-171572-PA. <https://doi.org/10.2118/171572-PA>.

Chen, C., and L. Zeng (2015), Using the level set method to study the effects of heterogeneity and anisotropy on hyporheic exchange, *Water Resour. Res.*, 51, 3617–3634, doi:10.1002/2014WR016444.

Chen, T., & Stagg, P. W. 1984. Semilog analysis of the pulse-decay technique of permeability measurement. *Society of Petroleum Engineers Journal*, 24(06), 639-642.

Chen Yuanqian. "Standardization on the Curves of Permeability and Capillary Pressure." *Experimental Petroleum Geology* 12.1 (1990): 64-70.

Chenevert, M. E., & Sharma, A. K. 1993. Permeability and effective pore pressure of shales. *SPE Drilling & completion*, 8(01), 28-34.

Chierici, G. L., et al. "Effect of the overburden pressure on some petrophysical parameters of reservoir rocks." 7th World Petroleum Congress. World Petroleum Congress, 1967.

Craig Jr., F.F. 1971. *The Reservoir Engineering Aspects of Waterflooding*, Vol. 3. Richardson, Texas: Monograph Series, SPE.

Dahraj, Naeem Ul Hassain, and Abid Ali Bhutto. "Linear mathematical model developed using statistical methods to predict permeability from porosity." PAPG/SPE Pakistan section Annual Technical Conference. Society of Petroleum Engineers, 2014.

Denney, Dennis. "Mapping Fractures and High-Permeability Channels in Waterfloods by Use of Injection and Production Rates." *Journal of Petroleum Technology* 62.01 (2010): 44-45.

Dicker, A. I., & Smits, R. M. 1988. A practical approach for determining permeability from laboratory pressure-pulse decay measurements. In *International meeting on petroleum engineering*. Society of Petroleum Engineers.

Dunn, Keh-Jim, Gerald A. LaTorraca, and David J. Bergman. "Permeability relation with other petrophysical parameters for periodic porous media." *Geophysics* 64.2 (1999): 470-478.

Economides M, Nolte K. *Reservoir Stimulation*. 2000.3rd edition: John Wiley and Sons.

F. Javadpour, Nanopores and apparent permeability of gas flow in mudrocks (shales and siltstone), *J Can Petrol Technol* 48 (2009) 16–21.

Fan, M., Han, Y., McClure, J., and Chen, C. 2017b. Hydraulic Fracture Conductivity as a Function of Proppant Concentration under Various Effective Stresses: From Partial Monolayer to Multilayer Proppants. *Unconventional Resources Technology Conference*. doi:10.15530/URTEC-2017-2693347.

Fan, M., L. Dalton, J. McClure, N. Ripepi, E. Westman, D. Crandall, and C. Chen (2019), On the Interactions between the Critical Dimensionless Numbers Associated with Multiphase Flow in 3D Porous Media, *SPE Journal*, in review.

Fan, M., McClure, J., Han, Y., Li, Z., and Chen, C. 2018. Interaction Between Proppant Compaction and Single-/Multiphase Flows in a Hydraulic Fracture. SPE-189985-PA. *SPE J*. doi:10.2118/189985-PA.

Firouzi, M., Alnoaimi, K., Kovscek, A., & Wilcox, J. 2014. Klinkenberg effect on predicting and measuring helium permeability in gas shales. *International Journal of Coal Geology*, 123, 62-68.

Garson, G. David. "Testing statistical assumptions." Asheboro, NC: Statistical Associates Publishing (2012).

Gomaa, Ahmed M., et al. "Computational Fluid Dynamics Applied To Investigate Development of Highly Conductive Channels Within the Fracture Geometry." *SPE Production & Operations* 32.04 (2017): 392-403.

Gu Lemin. "Historical review and future tendency of oil production in China." *Acta Petrolei Sinica* 37.2 (2016): 280-288.

Gu M, Mohanty KK. 2014. Effect of foam quality on effectiveness of hydraulic fracturing in shales. *Int J Rock Mech Min.* 70: 273-85.

Gupta, Robin, et al. "Enhanced waterflood for carbonate reservoirs-impact of injection water composition." *SPE Middle East Oil and Gas Show and Conference*. Society of Petroleum Engineers, 2011.

Haimson, B. C. "The hydrofracturing stress measuring method and recent field results." *International Journal of Rock Mechanics and Mining Sciences & Geomechanics Abstracts*. Vol. 15. No. 4. Pergamon, 1978.

Haskett, S. E., Narahara, G. M., & Holditch, S. A. 1988. A method for simultaneous determination of permeability and porosity in low-permeability cores. *SPE formation evaluation*, 3(03), 651-658.

Hayek, M. 2015. Exact solutions for one-dimensional transient gas flow in porous media with gravity and Klinkenberg effects. *Transport in Porous Media*, 107(2), 403-417.

Hess, Patrick H., et al. "Chemical method for formation plugging." *Journal of Petroleum Technology* 23.05 (1971): 559-564.

Howard, P. R., S. G. James, and David Milton-Taylor. "High Permeability Channels in Proppant Packs Containing Random Fibers." *SPE Formation Damage Control Conference*. Society of Petroleum Engineers, 1998.

Hu, G., Wang, H., Fan, X., Yuan, Z., & Hong, S. 2009. Mathematical model of coalbed gas flow with Klinkenberg effects in multi-physical fields and its analytic solution. *Transport in Porous Media*, 76(3), 407.

Hsieh, P. A., Tracy, J. V., Neuzil, C. E., Bredehoeft, J. D., & Silliman, S. E. 1981. A transient laboratory method for determining the hydraulic properties of 'tight' rocks—I. Theory. In *International Journal of Rock Mechanics and Mining Sciences & Geomechanics Abstracts* (Vol. 18, No. 3, pp. 245-252). Pergamon.

Innocentini, M. D., & Pandolfelli, V. C. 2001. Permeability of porous ceramics considering the Klinkenberg and inertial effects. *Journal of the American Ceramic Society*, 84(5), 941-944.

Jadhunandan, P. P., and Norman R. Morrow. "Effect of wettability on waterflood recovery for crude-oil/brine/rock systems." *SPE reservoir engineering* 10.01 (1995): 40-46.

Jones, S. C. 1997. A technique for faster pulse-decay permeability measurements in tight rocks. *SPE Formation Evaluation*, 12(01), 19-26.

Klinkenberg, L. J. 1941. The permeability of porous media to liquids and gases. In *Drilling and production practice*. American Petroleum Institute.

Kwon, O., Kronenberg, A. K., Gangi, A. F., & Johnson, B. 2001. Permeability of Wilcox shale and its effective pressure law. *Journal of Geophysical Research: Solid Earth*, 106(B9), 19339-19353.

Li, C., Xu, P., Qiu, S., & Zhou, Y. 2016. The gas effective permeability of porous media with Klinkenberg effect. *Journal of Natural Gas Science and Engineering*, 34, 534-540.

Li, Zihao, et al. "Formation damage during alkaline-surfactant-polymer flooding in the Sanan-5 block of the Daqing Oilfield, China." *Journal of Natural Gas Science and Engineering* 35 (2016): 826-835.

Liang, F., Sayed, M., Al-Muntasheri, G. A., Chang F. F., and Li, L. 2016. A comprehensive review on proppant technologies, *Petroleum*, 2(1): 26–39.

Lopes, Raul HC. "Kolmogorov-smirnov test." *International Encyclopedia of Statistical Science*. Springer Berlin Heidelberg, 2011. 718-720.

Lucia, F. J. "Petrophysical parameters estimated from visual descriptions of carbonate rocks: a field classification of carbonate pore space." *Journal of petroleum technology* 35.03 (1983): 629-637.

Mojarad, R. Salehi, and A. Settari. "Coupled numerical simulation of reservoir flow with formation plugging." *Canadian International Petroleum Conference*. Petroleum Society of Canada, 2005.

Montgomery, David R., and John M. Buffington. "Channel-reach morphology in mountain drainage basins." *Geological Society of America Bulletin* 109.5 (1997): 596-611.

- Ojala, I. O., & Fjær, E. 2007. The effective stress coefficient in porous sandstone. In 1st Canada-US Rock Mechanics Symposium. American Rock Mechanics Association.
- Pang, Y., Soliman, M. Y., Deng, H., & Emadi, H. 2017. Analysis of effective porosity and effective permeability in shale-gas reservoirs with consideration of gas adsorption and stress effects. SPE Journal.
- Park, Hun Myoung. "Univariate analysis and normality test using SAS, Stata, and SPSS." (2015).
- Pranter, Matthew J., Zulfiqar A. Reza, and David A. Budd. "Reservoir-scale characterization and multiphase fluid-flow modelling of lateral petrophysical heterogeneity within dolomite facies of the Madison Formation, Sheep Canyon and Lysite Mountain, Wyoming, USA." *Petroleum Geoscience* 12.1 (2006): 29-40.
- Seber, G. A., & Lee, A. J. (2012). *Linear regression analysis* (Vol. 329). John Wiley & Sons.
- Yamane, T. (1973). *Statistics: An introductory analysis*.
- Soeder DJ. Porosity and permeability of eastern Devonian gas shale. *SPE Form Eval* 1988;3(2):116–24.
- Stevens, James P. "Outliers and influential data points in regression analysis." *Psychological Bulletin* 95.2 (1984): 334.
- Tiab, d. and Donaldson, EC *Petrophysics*, Gulf Professional Publishing, Elsevier, MA, ISBN 0-7506-7711-2, 1999.
- Tabachnick, Barbara G., and Linda S. Fidell. *Using multivariate statistics*. Allyn & Bacon/Pearson Education, 2007.
- Vermilyen, J. P. 2011. *Geomechanical studies of the Barnett shale, Texas, USA*. Stanford University.
- Wang, G., Ren, T., Wang, K., & Zhou, A. 2014. Improved apparent permeability models of gas flow in coal with Klinkenberg effect. *Fuel*, 128, 53-61.
- Warpinski, N. R., & Teufel, L. W. 1992. Determination of the effective-stress law for permeability and deformation in low-permeability rocks. *SPE formation evaluation*, 7(02), 123-131.

- Wei, N., Gill, M., Crandall, D., McIntyre, D., Wang, Y., Bruner, K., Li, X., and Bromhal, G. (2014), CO₂ flooding properties of Liujiagou sandstone: influence of sub-core scale structure heterogeneity. *Greenhouse Gases-Science and Technology*, 2014. 4(3): p. 400-418.
- Willhite, G.P. 1986. *Waterflooding*, Vol. 3. Richardson, Texas: Textbook Series, SPE.
- Worthington, P. F. 2004. The stress response of permeability. In *SPE Annual Technical Conference and Exhibition*. Society of Petroleum Engineers.
- Wu, Y. S., & Pruess, K. 1998. Gas flow in porous media with Klinkenberg effects. *Transport in porous media*, 32(1), 117-137.
- Ye, Z. and Ghassemi, A. 2016. Deformation Properties of Saw-Cut Fractures in Barnett, Mancos and Pierre Shales. *Proceeding: 50th US Rock Mechanics/Geomechanics Symposium*, Houston, Texas.
- Zhang Hongxing., et al. "Variations of petrophysical parameters after sandstone reservoirs watered out in Daqing oil field." *SPE Advanced Technology Series* 5.01 (1997): 128-139.
- Zhang, J., Bai, M., Roegiers, J. C., Wang, J., & Liu, T. 2000. Experimental determination of stress-permeability relationship. In *4th North American Rock Mechanics Symposium*. American Rock Mechanics Association.
- Zhao, Fenglan, et al. "New type plugging particle system with high temperature & high salinity resistance." *Journal of Petroleum Science and Engineering* 152 (2017): 317-329.
- Zhou, Z., et al. "A new method for water shut-off in high permeability channels." *Annual Technical Meeting*. Petroleum Society of Canada, 1998.
- Zhu, W. C., Liu, J., Sheng, J. C., & Elsworth, D. (2007). Analysis of coupled gas flow and deformation process with desorption and Klinkenberg effects in coal seams. *International Journal of Rock Mechanics and Mining Sciences*, 44(7), 971-980.